X-ray Observations of Black Holes

Röntgenbeobachtungen Schwarzer Löcher

Der Naturwissenschaftlichen Fakultät
der Friedrich-Alexander-Universität
Erlangen-Nürnberg

zur
Erlangung des Doktorgrades Dr. rer. nat.

vorgelegt von

Maria Hirsch
aus Neumarkt

Als Dissertation genehmigt
von der Naturwissenschaftlichen Fakultät
der Friedrich-Alexander-Universität Erlangen-Nürnberg
Tag der mündlichen Prüfung: 23. Mai 2019

Vorsitzender des Promotionsorgans: Prof. Dr. Georg Kreimer

Gutachter: Prof. Dr. Jörn Wilms
Dr. Jérôme Rodriguez

Contents

Abstract

X-ray observations of black holes – the title of this work covers a broad field of science with so many different aspects that it is impossible to even mention them all here. The focus therefore is on binary systems, i.e., systems containing a compact object and a companion star of some kind. They orbit around a common center of mass, and in almost all cases matter is transferred from the companion star onto the compact object. With the evolution of observing techniques and the continuing growth of data archives, it is now possible to take a closer look at this mass transfer, its implications for the evolution of the systems, and at the information on the physical conditions that can be collected by such observations. To illustrate the bandwidth of possibilities, three examples of such binary systems are presented.

New observations of the intermediate mass X-ray binary GRS 1758−258, consisting of a black hole and an A-type companion star, are presented first. In this kind of system, mass transfer is accomplished via Roche lobe overflow: The companion star completely fills out the area in the common gravitational system that is dominated by its own gravitational attraction. The easiest way for the mass the star is losing in a stellar wind is via the inner Lagrange point, a saddle point in the binary potential, toward the compact object. Usually, such systems are transient X-ray sources; GRS 1758−258 is one of only few persistent ones. A characteristic feature for these objects are their different X-ray states. Whereas they are mostly found in the hard state with a powerlaw-dominated spectrum of a Photon index of $\Gamma < 2$, they sometimes change into a soft state by first increasing in brightness and, in a second step, a spectral steepening: A blackbody disk component becomes visible in the spectrum. Only once they have dimmed again, they change back to a hard spectral shape, thus following a hysteresis curve in their hardness intensity diagram. Several models have been proposed with various physical scenarios that can lead to such a state change. Current observations, however, do not allow yet to exclude some of these models or prefer one over the others.

GRS 1758−258 as a persistent source also shows this hysteresis curve, albeit without the brightening in the hard state. In some rare occasions, however, the dimming during a soft state is so strong that GRS 1758−258 is not detected any more in the hard X-rays. This behavior was first observed by Smith et al. (2001) and, in course of the ongoing monitoring of the source, again in 2016. The analysis of four Target of Opportunity observations with the Neil Gehrels-*Swift* observatory clearly show the spectral change during the dimming. The fitted blackbody disk temperatures are consistent with previous observations. Due to the lack of data in the hard X-rays, however, a correlation between the powerlaw Photon index and the disk temperature cannot be solved completely. In a dynamical power spectrum, GRS 1758−258 shows periodic modulations with a period around 18 days that is variable

with time. There are indications that kinks in the periodicity could be associated with the occurrences of the very dim soft states. Once these special characteristics are better understood, GRS 1758−258 might be an interesting test case for improved state transition models.

The second example is a class of sources that are candidates for the progenitors of supernova type Ia explosions and therefore possibly black holes to-be: Super soft X-ray sources are characterized by their extremely soft spectra and their complete lack of emission in the hard X-rays. They consist of an accreting white dwarf as a compact object, accompanied by a main sequence star. Depending on the accretion rate and the white dwarf mass, a hydrogen burning shell can develop around the compact object, emitting the super soft X-ray radiation. During the hydrogen burning time, transient periodic signals are observed in the light curves of such objects. This work shows how the significance of such transient signals can be confirmed. Once more systems showing the transient periodicities are observed and the mechanism that produces these modulations is investigated, conclusions could be drawn on the masses of white dwarfs in these objects, thus learning more about the possible progenitors of supernova type Ia explosions and the conditions before such explosions.

The third class of objects, high mass X-ray binaries, are exemplified in Cyg X-1, a system consisting of a black hole and the OB-giant star HDE 226868. This type of star emits a strong stellar wind that is focused towards the compact object. Three *Chandra* High Energy Transmission Gratings observations at different phases around $\phi_{\mathrm{orb}} = 0$ show that the stellar wind that is powering the accretion in this system is characterized by temperature and density inhomogeneities including structures, or "clumps" of colder, more dense material embedded in the photoionized gas. As these clumps pass the line of sight, absorption dips appear in the light curve. The physics of the clumps are characterized through spectral changes during various dip stages. Comparing the silicon and sulfur absorption line regions (1.6–2.7 keV ≡ 7.7–4.6 Å) in four stages of varying column depth reveals the presence of more lower ionization stages, i.e., colder or denser material, in the deeper dip stages. The Doppler velocities of the lines are roughly consistent within each observation, varying with the respective orbital phase. This is consistent with the picture of a structure that consists of differently ionized material, with shells facing the black hole shielding the inner and back shells from the ionizing radiation. The variation of the Doppler velocities compared to a toy model of the stellar wind, however, does not allow us to pin down an exact location of the clump region in the system. This result, as well as the asymmetric shape of the observed lines, point at a complex wind structure (Hirsch et al., 2019).

With the future *XRISM* and *Athena* missions, huge improvements in effective area and spectral resolution will allow for a closer study of single clumps, providing further insights into the composition of the plasma and its behavior under extreme physical conditions.

Zusammenfassung

Röntgenbeobachtungen Schwarzer Löcher – der Titel dieser Arbeit umfasst ein außerordentlich weites Themengebiet. Da es kaum möglich ist, auf alle Facetten dieses Gebiets auch nur kurz einzugehen, werde ich mich im folgenden auf Röntgendoppelsterne beschränken, die aus einem kompakten Objekt und einem stellaren Begleiter bestehen. Solche Systeme rotieren um einen gemeinsamen Masseschwerpunkt und in den meisten Fällen verlagert sich mit der Zeit Masse vom Begleitstern zum kompakten Objekt, welche dort akkretiert wird. Verbesserungen in der Beobachtungstechnik und stetig wachsende Datenarchive ermöglichen es heute, solche Systeme näher zu betrachten und ihre Entwicklung sowie die extremen physikalischen Bedingungen in ihrer Umgebung zu beobachten. Drei Beispiele sollen die vorhandene Bandbreite an Objekten verdeutlichen:

Das erste System trägt den Namen GRS 1758−258 und besteht aus einem Schwarzen Loch und einem Begleitstern der Spektralklasse A. Dieser Begleitstern füllt sein Roche-Volumen, also den Raum im gemeinsamen Gravitationspotential des Systems, den er mit seiner eigenen Schwerkraft dominiert, komplett aus. Masse, die er in Form eines Sternwindes verliert, kann über einen Sattelpunkt im Potential, den inneren Lagrangepunkt, in den Einflussbereich des Schwarzen Lochs hinüberströmen und dort akkretiert werden. Im Regelfall sind solche Systeme nur vorübergehend im Röntgenbereich zu beobachten; GRS 1758−258 bildet hier als ständig sichtbare Quelle eine Ausnahme. Eine charakteristische Eigenschaft solcher Systeme sind die verschiedenen spektralen Zustände, die sie durchlaufen. Zumeist befindet sich ihr Spektralindex im harten Bereich. Es ist jedoch möglich, dass sich ihr spektraler Zustand ändert, indem die Emission zunächst zunimmt, woraufhin das Spektrum weicher wird. Man kann nun Schwarzkörperstrahlung einer Akkretionsscheibe als zusätzliche Komponente im weichen Röntgenbereich messen. Einmal im weichen Bereich, nimmt die Intensität der Quelle wieder ab und schließlich ändert sich das Spektrum zurück zum ursprünglichen harten Spektralindex. Viele Modelle, die diesem Kreislauf zugrunde liegen könnten, wurden schon vorgeschlagen. Die derzeitige Datenlage erlaubt allerdings nicht, ein einziges allgemeingültiges Modell auszuwählen.

Auch GRS 1758−258 zeigt diesen Kreislauf – jedoch, als ständig sichtbare Quelle, ohne den Helligkeitsanstieg und -abfall mit hartem Spektrum. Es ist bisher zweimal vorgekommen, zuerst beobachtet von Smith et al. (2001) und dann wieder im Herbst 2016, dass GRS 1758−258, sobald es sich im Bereich der weichen Spektralform befindet, immer dunkler wird, soweit bis die Quelle im harten Röntgenbereich nicht mehr sichtbar ist. Dieses ungewöhnliche Verhalten wurde 2016 in vier Beobachtungen mit dem Neil Gehrels-*Swift*-Observatorium festgehalten. Die spektrale Veränderung im Verlauf ist deutlich sichtbar, die

gemessene Temperatur der Schwarzkörperstrahlung stimmt mit vorherigen Beobachtungen überein. Eine genaue Aussage über den Spektralindex zu treffen, ist jedoch nicht möglich, da die Quelle im harten Röntgenbereich nicht mehr zu beobachten war. Eine Zeitreihenanalyse der mehrjährigen Lichtkurven von GRS 1758−258 zeigt eine veränderliche Periodizität um die 18 Tage, die möglicherweise mit diesen besonderen Spektralzuständen zusammenhängen könnte. Ein besseres Verständnis dieser Quelle würde es möglich machen, sie als Testobjekt für Modelle zu verwenden, die den spektralen Kreislauf physikalisch beschreiben sollen.

Die zweite Art Quellen, die hier präsentiert werden soll, sind mögliche Vorgängersysteme von Typ Ia Supernovae, und damit eventuell zukünftige Schwarze Löcher. Ein extrem weiches Röntgenspektrum ohne harten Anteil zeichnet diese Systeme aus, die aus einem akkretierenden Weißen Zwerg und einem Hauptreihenstern als Begleiter bestehen. Je nach Akkretionsrate und Masse des Weißen Zwerges kann sich um diesen für kurze Zeit oder auch andauernd eine Hülle aus brennendem, also fusionierendem Wasserstoff bilden, die für die weiche Röntgenstrahlung verantwortlich ist. Während diese Hülle existiert, werden vorübergehend periodische Signale von diesen Systemen detektiert. Diese Arbeit zeigt, wie die Signifikanz solcher Signale bestimmt werden kann. Sie können Hinweise auf die Masse der Weissen Zwerge geben und es so ermöglichen, mehr über die Vorgänger von Supernova-Explosionen zu lernen.

Als drittes Beispiel dient Cyg X-1, ein Röntgendoppelstern bestehend aus einem Schwarzen Loch und dem Blauen Überriesen HDE 226868 als Begleiter. Dieser massive Begleitstern emittiert einen sehr starken Sternwind, der zum Schwarzen Loch hin gebündelt wird. Drei Beobachtungen mit dem Gitterspektrographen auf dem Satelliten *Chandra* um die Phase $\phi_{\mathrm{orb}} = 0$ zeigen, dass das photoionisierte Gas dieses Sternwinds bezüglich Temperatur und Dichte sehr inhomogen ist und Strukturen, „Klumpen“, aus kälterem oder dichterem Material enthält. Bewegen sich diese Klumpen durch die Sichtlinie des Beobachters, entstehen aufgrund von Absorption Einbrüche in der Lichtkurve. Diese Einbrüche werden in vier verschiedene Stufen eingeteilt. Ein Vergleich der Silizium- und Schwefelabsorptionslinien über diese vier Stufen zeigt, dass sich im tiefsten Teil der Einbrüche niedrigere Ionisationsstufen finden lassen, was für die Anwesenheit von kälterem oder dichterem Material spricht. Die Dopplergeschwindigkeiten, die für die Linien gemessen werden, sind innerhalb einzelner Beobachtungen konsistent, verändern sich jedoch mit der jeweiligen Orbitalphase. Dies entspricht der Vorstellung von Strukturen aus verschieden stark ionisiertem Material, wobei die dem Schwarzen Loch und seiner ionisierenden Strahlung zugewandten Schichten das dahinterliegende Material von der Strahlung abschirmen. Ein Vergleich der Dopplergeschwindigkeiten mit einem stark vereinfachten Modell für den Sternwind erlaubt jedoch nicht, den Aufenthaltsort der Klumpen im Doppelsternsystem genauer zu bestimmen. Zusammen mit den Asymmetrien, die im Linienprofil beobachtet werden, lässt dies auf eine komplexe Windstruktur schließen.

Die derzeit in Planung befindlichen Satelliten *XRISM* und *Athena* mit ihrer deutlich verbesserten effektiven Fläche und spektraler Auflösung werden es möglich machen, einzelne Klumpen zu untersuchen und so weitere Erkenntnisse über die Zusammensetzung des Sternwindes und über das Verhalten von solchem Material unter extremen physikalischen Bedingungen zu gewinnen.

1

A collapsar's a gravity whisk;
On approaching, you run a great risk
  That your atoms will flow
  In a gamma-ray glow
And accrete in a spiraling disk.

(Mike Scholtes)

Why X-rays

Throughout the ages, astronomy has been one of the sciences that never ceased to inspire people, to let them strive after discovering the unknown. Starting out in Egypt with the connection between the seasons and the patterns of stars on the night sky, in Greece with the discovery of the wandering stars and the Arabic astronomical tables, continuing throughout the medieval ages with various explanations of the solar system (Aveni, 1993), up to the recent detection of gravitational waves (Abbott et al., 2016), space and its wonders have always fascinated both professional and amateur astronomers. For centuries, we have considered the Universe as a vast laboratory, allowing us to observe the most extreme physical phenomena, always pushing technology beyond its limits.

Thus, it is not surprising that astronomy is present in many aspects of our daily life. Not only is there a close link between the scientific development of a region and its human development index (Truman, 1949), but one can find developments that have their roots in astronomy almost everywhere if one only looks. Personal computers, mobile phones and their cameras, solar panels, communication and navigation satellites, even various imaging techniques used in modern medicine trace back to technologies developed for and used in astronomy (Rosenberg et al., 2013). Especially satellites and imaging techniques were extremely pushed by the desire to observe the sky not only in the optical waveband that can pass through the atmosphere, but also in the X-ray band, for which the atmosphere is opaque, as shown in Fig. 1.1.

What is so important for us to be able to catch a glimpse on, though, that we spend heaps of money to build detectors, put them on a rocket and shoot them into space? The answer to this question is easily given: Astronomers regard space as a vast laboratory where they can explore science in an extent and in extremes that are simply not possible on earth. Chapter 1 of this thesis gives a quick tour through this laboratory and introduces its "facilities", i.e., stars in their various life stages, and the basic physical processes that are important for X-ray astronomy. Chapter 2 introduces the current X-ray observatories I used to take a closer look at different kinds of objects, namely super soft sources (Chapter 4), low and intermediate mass X-ray binaries (Chapter 3), and high mass X-ray binaries (Chapter 5).

1.1 Stages in a stellar lifetime

The universe offers astronomers a huge variety of very diverse objects. From very tiny to extremely large, from almost no weight to more weight than one can imagine, from vacuum

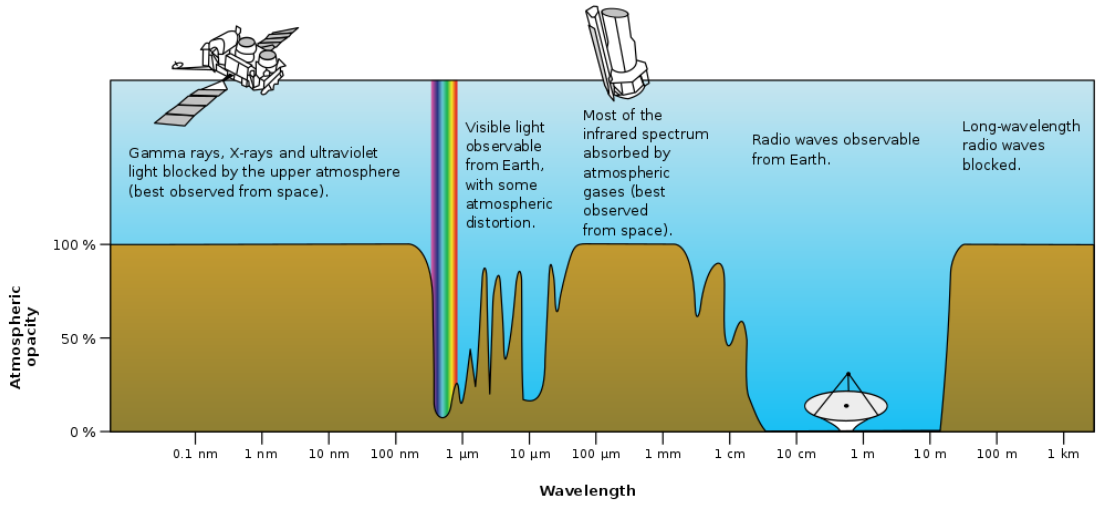

Figure 1.1: The atmospheric window
(http://gsp.humboldt.edu/olm_2015/Courses/GSP_216_Online/lesson2-1/atmosphere.html)

to the most dense material, it all is out there, waiting for us to take a look. It should be noted that it is only about four percent of the stuff that makes up our Universe that we actually know and, more or less, understand: visible matter. The rest, what we cannot see but know that it has to be there, dark matter and dark energy, are still beyond our reach. Here, I want to give an overview of the perhaps most obvious part of visible matter, namely stars, and their evolution as well as how they interact with their surroundings. This section can only give a short overview. For more detailed descriptions, see, e.g., Carroll & Ostlie (1996); Karttunen et al. (2007).

Mostly, the first thought that comes up at the word “star” is a bright dot on the night sky. If we look closer, we can see, that none of these dots are exactly the same. They have different colors, pointing to different temperatures (Planck, 1900). Some are flickering, some are not. Some are bright, some are dim, even if they are at the same distance to earth. We observe a cross-section of stellar population and evolution.

The Hertzsprung-Russell-Diagram (HRD, named after the astronomers Ejnar Hertzsprung, 1873–1967, and Henry Norris Russell, 1877–1957, see Fig. 1.2) helps us to categorize these observations. This diagram orders stars according to their temperature on the x-axis (somewhat counter-intuitive, hot, blue stars are located at the left and temperature is decreasing to the right of the x-axis where we find cool, red stars), and their brightness on the y-axis. During the time the stars are burning hydrogen to helium in their cores, they are located on the main sequence: The more massive stars are brighter and hotter, whereas the less massive stars are cooler and less luminous. It is depending on their mass, too, how they evolve once the hydrogen burning subsides. Solar mass stars leave the main sequence once the hydrogen in their cores is exhausted. They enter the red giant branch, their outer shells expand whereas the core, now missing the radiation pressure from hydrogen burning, is compressed. The temperature rises due to the degeneracy until helium burning starts in a flash with the triple α process. The star is now burning helium to heavier elements in the core and hydrogen to helium in the outer shells. It enters the asymptotic giant branch. Due to the helium core burning being unstable, thermal pulses lead to the ejection of the outer

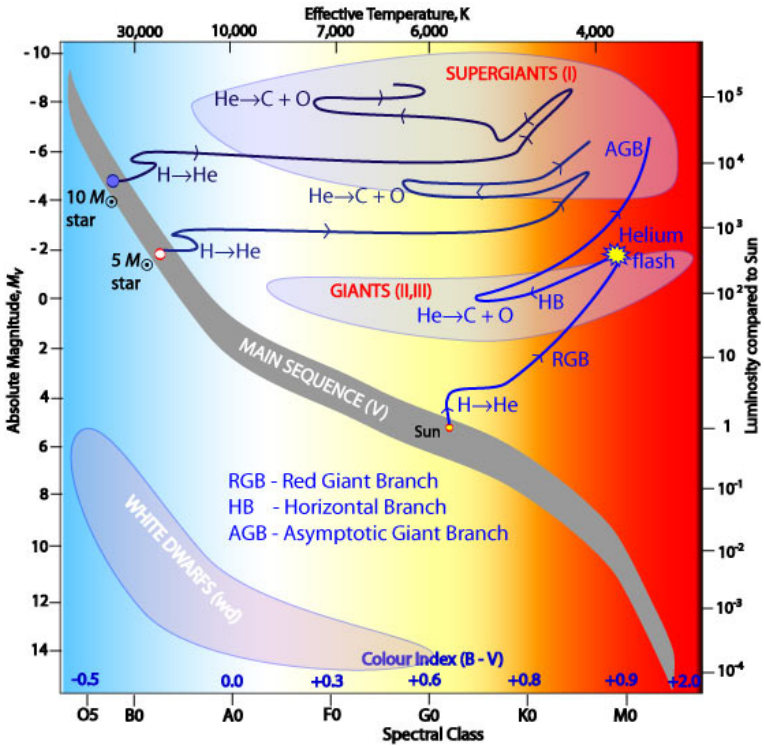

Figure 1.2: Hertzsprung-Russell-diagram (http://www.atnf.csiro.au/outreach//education/senior/astrophysics/stellarevolution_postmain.html)

layers. The hot core, a white dwarf, remains, ionizing the ejecta to a planetary nebula, and slowly cooling down.

Stars of higher masses evolve similarly, but much faster. Due to their higher temperature on the left side of the HRD, the triple α process sets in before the core is degenerated, and helium burning just starts. Fusion continues until the core reaches iron. ^{56}Fe is the most tightly bound nucleus produced in stellar nucleosynthesis[1], and from this point on, the fusion process becomes endothermic. Similar to the low mass stars, the radiation pressure cannot be sustained in the core, and it collapses to a maximum density of almost $10^{18}\,\mathrm{kg\,m^{-3}}$. The Pauli principle applies and all further infalling material bounces off the dense core, building out a shock wave, driving the outer layers away from the core. There are two possibilities for the appearance of the stellar remnant: If the initial mass of the star was below about 25 solar masses, the core will stabilize due to the degenerate neutron pressure, forming a neutron star. For larger initial masses, the neutron degeneracy pressure is not large enough to counterbalance the gravitational pressure and the core collapses completely, forming a black hole (e.g., Fryer & Kalogera, 2001; Woosley et al., 2002).

1.2 X-ray binaries

Most stars in the Universe are not single stars: They appear in binary systems. If one of the two stars in such a system reaches its end of life, the newly formed compact object might be able to accrete matter from its companion star. The resulting system is called an X-ray binary. X-ray binaries are not only characterized by the compact object of the system: It is

[1] Fewell (1995) point out that ^{62}Ni has an even higher binding energy, but is not reached in stellar fusion.

also common to classify them by the mass of the companion main sequence star into low mass X-ray binaries (LMXB) for companion masses $m \lesssim 10 M_\odot$ and high mass X-ray binaries (HMXB) for companion masses $m \gtrsim 10 M_\odot$, i.e., an O-star or B-star. Both classes of systems generally show different attributes, however, in some cases the line between them is blurred and there are systems with intermediate mass companions that show characteristics of both categories.

In this thesis, I will present three different examples of such binary systems: Super soft sources consisting of a white dwarf and an optical companion, an intermediate mass X-ray binary consisting of a black hole or and an A-type optical companion, and a HMXB consisting of a black hole and a high mass optical companion.

1.2.1 Low mass X-ray Binaries

A common picture of the formation of an LMXB, first proposed by Whelan & Iben (1973) in a different context, are systems containing a relatively massive white dwarf that is accreting mass from its main sequence companion. Once the mass of the white dwarf reaches the Chandrasekhar limit (Chandrasekhar, 1931a,b, 1935), it can no longer compensate its own gravitational attraction with electron degeneracy pressure, i.e., the impossibility of two electrons occupying the same quantum state in the same system at the same time: There is only a finite number of states available for extremely dense environments, limiting the number of electrons and thus creating a pressure. The exact mass for which this electron degeneracy pressure is overcome by gravitational self-attraction depends on the chemical composition of the compressed gas, the thermal structure, Coulomb interaction between the particles and relativistic effects (Timmes et al., 1996). If this mass limit is surpassed, the extreme gravitational pressure forces the electrons into the nuclei through electron capture,

$$\mathrm{p} + \mathrm{e}^- \rightarrow \mathrm{n} + \nu_\mathrm{e},$$

in an implosion with little mass loss, leaving a neutron star.

Other mechanisms to form an LMXB include, e.g., an inspiral phase of an initially high mass system that loses most of its mass and angular momentum, ending up in an LMXB. Dynamic processes like the capture of a compact object that originated outside of its current binary system (Lewin et al., 1997; Michaely & Perets, 2016) or several subsequent fly-by interactions shrinking the orbit of a formerly wide system (Klencki et al., 2017) are both scenarios that can happen primarily in globular clusters. A classical supernova explosion (Kalogera, 1998) can also end up in an LMXB.

Both, the imploding white dwarf and the mass loss settings, require the binary systems to lose a large part of their angular momentum in order to reflect the range of observed binary separations for LMXBs of ~ 0.1–$10\ R_\odot$, which is much smaller than the size of the progenitor of the compact object itself. This loss of angular momentum can happen in common envelope phases (Kalogera & Webbink, 1998), where one of the companions loses more mass than the other can accrete, thus engulfing both binary companions in a common envelope of ejected mass. Inside this envelope, energy is deposited via friction and an inspiral takes place until the envelope material gained enough energy to leave the system.

In our region of the Universe, LMXBs are comparatively rare sources, with less than 200 confirmed LMXBs known in our Galaxy and the Magellanic Clouds (e.g., Ritter & Kolb, 2003,

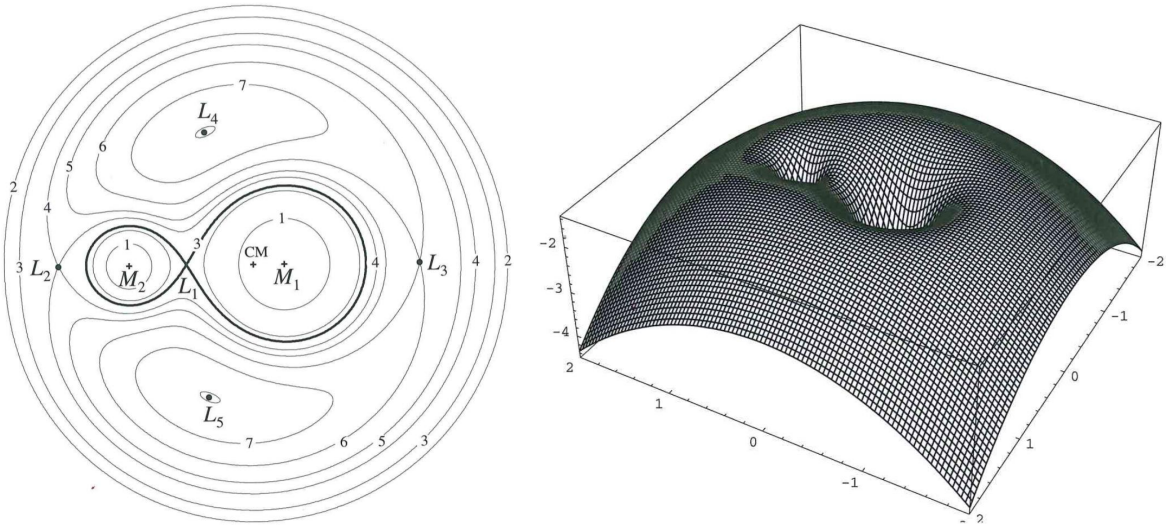

Figure 1.3: Left: Equipotential lines of the Roche potential (Frank et al., 2002, Fig. 4.3). *CM* demarks the center of mass of the two companions of masses M_1 and M_2. $L_{1...5}$ are the Lagrange points of the system. **Right:** 3D representation of the Roche potential (Frank et al., 2002, Fig. 4.2).

last updated 2015). There is simply not enough statistics to make exact statements about the formation and the progenitor systems. What we can do, however, is to collect and map LMXB characteristics and search for patterns to piece together a depiction of this kind of sources.

The probably most obvious feature is the mass of the companion star, giving the class of sources its name. The optical spectra of the companion stars show characteristics of spectral types A or later. X-ray radiation is powered by accretion onto the compact object. To take a closer look at the accretion process in an LMXB, one needs to consider the gravitational potential of a binary system in the corotating frame, called the Roche potential after the French astronomer Edouard Albert Roche (1820–1883),

$$\Phi_{\mathrm{R}}(r) = -\frac{GM_1}{|r-r_1|} - \frac{GM_2}{|r-r_2|} - \frac{1}{2}(\omega \times r)^2 . \tag{1.1}$$

It contains the gravitational potentials of the two companions at r_1 and r_2, as well as a centrifugal term for a test mass at the position r, as the system is rotating with the angular velocity

$$\omega = \left(\frac{GM}{a^3}\right)^{1/2} . \tag{1.2}$$

The equipotential lines of the Roche potential (Fig. 1.3, left) depend on the mass ratio in the binary system and are roughly peanut-shaped in the immediate neighborhood of the binary. For each of the companions, there is a region where its own gravitational potential is dominating. This region is called a Roche lobe. The two Roche lobes of the system are touching each other in the inner Lagrange point L_1 where the gravitational forces of both objects equal each other. There are four more local maxima or Lagrange points in the potential: L_2 and L_3 are the easiest escape routes for material leaving the binary system. Those three are saddle points. L_4 and L_5, known for their collection of asteroids, are the plateau points of the Roche potential (see Fig. 1.3, right). Despite its complex shape in close-up, however, the system appears to be a point mass from the distance.

To track the motion of gas in this system, this potential is put into the Euler equation (Euler, 1757)

$$\frac{\mathrm{d}^2 r}{\mathrm{d}t^2} + 2\omega \times \frac{\mathrm{d}r}{\mathrm{d}t} = -\frac{1}{\rho}\nabla P - \nabla\Phi \tag{1.3}$$

which contains both the gravitational force due to the two companions using the Roche potential Φ_R as well as the Coriolis force $f_c = 2\omega \times v$ acting on the gas.

In the close binary system, the Roche lobe of the companion is comparatively small and quickly filled completely by the companion star. The system is then called a contact binary. Mass then may be pushed beyond the inner Lagrange point L_1 towards the compact object by perturbations of the material, e.g., by pressure forces. This transfer of mass is called Roche lobe overflow (see, e.g., Frank et al., 2002, for a more detailed description). The compact object is now accreting matter that carries a considerable amount of angular momentum. In a ballistic free fall towards the compact object, following the Roche potential, the matter first forms elliptical orbits. As the binary is rotating, i.e., in the rest frame of the compact object, the source of mass is rotating, the elliptical orbits of the mass stream will intersect and cause shocks, thus lead to a randomization. Circular orbits are formed. Dissipative processes then lead to the gas heating up, radiating away energy and thus moving deeper into the potential well of the compact object. An accretion disk has formed.

As it is mostly the case in nature, things do not work as smooth as predicted from theory. In fact, most LMXBs containing a black hole as compact object are not persistent systems but show a transient behavior with long phases of quiescence, interrupted by bright outbursts. These outbursts happen whenever there is a sudden onset or increase in the accretion flow. While in the quiescent state, these systems are not detected in the X-rays. The outbursts of black hole X-ray binaries (BH-XRBs), however, follow a characteristic pattern. When they become first visible, as well as during the brightening phase, they show very hard spectra (hard state). Once they reach their maximum luminosity, the spectrum begins to soften. The radio emission usually seen during the hard state quenches. High frequency quasi-periodic oscillations (QPOs) appear, and the source enters the soft state. This state is characterized by variations of spectral hardness (but still much softer than the hard state) and a decrease in luminosity. Finally, the spectrum hardens again before the source dims back into quiescence. In Chapter 3, GRS 1758−258 is presented as an example for this class of sources.

1.2.2 High mass X-ray binaries

Equivalent to the LMXBs discussed before, high mass X-ray binaries (HMXBs) contain a compact object, which is either a neutron star or a black hole, and a massive O-star or B-star companion. Due to the higher mass of this companion, the binary orbit, too, can be larger, allowing for periods of up to a few hundred of days. The major difference between the two kinds of systems, however, is the behavior of the companion star: Massive stars produce strong stellar winds (e.g., Abbott, 1978; Blondin et al., 1991; Puls et al., 2006; Oskinova et al., 2006; Puls et al., 2008; Oskinova et al., 2012). Thus, there is enough material for the compact object to accrete regardless whether the star fills its Roche lobe or not: A radially emitted wind will be focused towards the compact object.

To understand the phenomena that occur in such a wind-accreting binary, a closer look at stellar wind and its properties is essential. In the case of O- or B-stars, the stellar wind

cannot be due to pressure gradients like in the later type stars: The velocities observed in winds of massive stars, a few hundreds of kilometers per second, are much faster than the speed of sound in, e.g., G type stars,

$$v_s = \left(\frac{\gamma P}{\rho}\right)^{1/2}, \tag{1.4}$$

where for an ideal, monoatomic gas with $f = 3$ degrees of freedom, i.e., $\gamma = 1 + 2/f = 5/3$, the pressure is $P = nkT$ and the density is $\rho = nm$ with the number of particles per cm^3 n and the proton mass m, leading to

$$v_s = \left(\frac{5}{3}\frac{nkT}{nm}\right)^{1/2} = \left(\frac{5}{3}\frac{kT}{m}\right)^{1/2}. \tag{1.5}$$

For a typical G type star like the Sun, a temperature of 5000–6000 K leads to a speed of sound of $\sim 10\,\mathrm{km\,s^{-1}}$. But even the higher temperatures of $10^{5\ldots6}$ K of OB stars only yields a speed of sound of a few tens to a hundred km s^{-1}, making the wind of these stars supersonic. The additional force needed to drive this wind is radiation pressure: The hot OB star strongly radiates in the ultraviolet region. The material in the stellar atmosphere absorbs these UV photons and gets accelerated outwards by the momentum transfer of the photons onto the material. As the photoabsorption is not equal over the continuum but happens at discrete energies (see Sect. 1.6), the thus accelerated wind is called line-driven.

Castor et al. (1975) developed a model for such a line-driven wind, known as CAK-model. The force exerted on the gas of an expanding atmosphere through radiation pressure depends on the local velocity gradient. Through analytic approximations, Castor et al. (1975) modeled this force solely dependent on the mass of the OB star, its luminosity, photospheric radius and mass loss rate. They find a velocity law of

$$v^2 = \frac{\alpha}{1-\alpha}\,2GM(1-\Gamma)\left(\frac{1}{r_0} - \frac{1}{r}\right) \tag{1.6}$$

(Castor et al., 1975, Eq. 47), where the ratio of stellar to Eddington luminosity is

$$\Gamma = \frac{\sigma_e L}{4\pi GMc}.$$

In this equation, σ_e is the mass scattering coefficient of free electrons, which is $\sigma_e = 0.33\,\mathrm{cm^2\,g^{-1}}$ for all except Wolf-Rayet stars (Abbott, 1978). The velocity law contains the escape velocity

$$v_{\mathrm{esc}} = \left(\frac{2GM(1-\Gamma)}{r_0}\right)^{1/2} \tag{1.7}$$

(Abbott, 1978, Eq. 4), which can be scaled to the terminal velocity of the stellar wind, v_∞, using a constant α, which depends on the stellar temperature (see Castor et al., 1975, Table 1), to

$$v_\infty = \left(\frac{\alpha}{1-\alpha}\right)^{1/2} v_{\mathrm{esc}} = \left(\frac{\alpha}{1-\alpha}\,\frac{2GM(1-\Gamma)}{r_0}\right)^{1/2}. \tag{1.8}$$

Friend & Castor (1982) take into account effects of the compact object in the system, both through gravitational and continuum radiation pressure forces, as well as centrifugal forces due to the binary orbital motion. Friend & Castor (1983) as well as Pauldrach et al. (1986)

expand the model to correctly include the angle integration instead of using a radial approximation, and to take into account multiple scattering processes in overlapping line series, leading to further enhanced velocities. Friend & Abbott (1986) also include the finite size of the star, leading to a more gradual velocity, as well as a centrifugal force due to the rotation of the star, reducing the terminal velocity. Both effects, however, are comparatively small.

It is obvious that in a HMXB system containing an OB star and a black hole where, due to gravitational forces, the stellar wind is focused towards the black hole, the wind will not be of smooth consistency but initially small perturbations will quickly grow and result in shocks (Owocki & Rybicki, 1984) and shells of denser material (Feldmeier et al., 1997; Dessart & Owocki, 2003) which then break apart and form clumps. Using the high energetic radiation provided by the black hole to "X-ray" these clumps, important observational facts concerning the chemical composition, the ionization stage and the velocity can be obtained.

1.3 Accretion

Once the mass flow from the companion star, whether via Roche-lobe overflow or via a focused wind, has formed an accretion disk, we are looking at the most powerful source of energy in space: Accretion onto a compact object. This section contains an overview of the most important aspects for this work. A comprehensive review of accretion processes can be found, e.g., in Frank et al. (2002).

The amount of potential energy that is released with accretion of a mass m is dependent on the mass and radius of the accreting object, M_* and R_*:

$$E_{\mathrm{acc}} = \frac{GM_*m}{R_*} = \frac{mc^2}{R_*/R_{\mathrm{g}}} \tag{1.9}$$

where $R_{\mathrm{g}} = GM/c^2$ is the gravitational radius of the mass M. A typical radius for a neutron star is $R_* = 10\,\mathrm{km}$, and with one solar mass, $M_* = M_\odot$ the released energy adds up to $1.3 \cdot 10^{13}\,\mathrm{J} \equiv 1.3 \cdot 10^{20}\,\mathrm{erg}$ per accreted gram, released mostly in the form of electromagnetic radiation. This is about twenty times the energy freed by nuclear fusion a gram of hydrogen. The ratio of course changes for less dense objects such as white dwarfs, which are comparable in mass but have much larger radii. The timescales, however, on which the two processes are happening, still make accretion an important process for white dwarfs: While nuclear fusion is a very fast reaction and, using up all available material during a very short time, produces short events of extreme brightness (so-called "nova outbursts"), during the major part of its lifetime no nuclear fusion happens and the luminosity of the white dwarf is entirely powered by accretion.

Eddington Luminosity

Accretion, powerful as it is, also has its natural limit: Once the force caused by radiation pressure of the energy released in the accretion process equals the gravitational force moving the matter towards the accreting object, the accretion process cannot be sustained any more. The luminosity corresponding to this hydrostatic equilibrium is called Eddington luminosity (after Sir Arthur Stanley Eddington, 1882–1944, a British Astrophysicist) and can be calculated to

$$L_{\mathrm{Edd}} = \frac{4\pi G M m_{\mathrm{p}} c}{\sigma_{\mathrm{T}}} \tag{1.10}$$

for a proton of the mass $m_{\mathrm{p}} = 1.67 \cdot 10^{-27}\,\mathrm{kg}$, where σ_{T} is the Thomson cross section for non-relativistic electron-photon scattering. Note, however, that this approach is based on the assumption of a spherically symmetric accretion of a fully ionized hydrogen plasma[2]. There are only few sources reaching the Eddington limit. Once they exceed this luminosity, they start to emit strong winds, blowing away a substantial part of their mass (e.g., Owocki & van Marle, 2008).

Accretion Disks and Emitted Spectra

Matter within the reach of a compact object, whether it comes from a binary companion or not, usually comes with a non-zero angular momentum with respect to the accreting object, which prohibits a direct infall of the material: it starts circulating the compact object in an elliptical orbit. Dissipative processes cause the material to heat up and radiate, draining the gas of its energy and thus causing it to move inward, deeper into the potential well. An accretion disk is formed.

The standard accretion disk model, a geometrically thin disk, was proposed by Shakura & Sunyaev (1973), who assume a disk in a local thermal equilibrium. The viscous dissipation per unit disk face area can be expressed as

$$D(R) = \frac{3GM\dot{M}}{8\pi R^3}\left\{1 - \left(\frac{R_*}{R}\right)^{1/2}\right\} \tag{1.11}$$

(see Frank et al., 2002, Eq. 5.20). For a locally thick (in z-direction) disk, the emitted spectrum roughly resembles a blackbody, and a characteristic measure for the emitted photons is the radiation temperature $T(R)$:

$$\sigma_{\mathrm{SB}} T(R)^4 = D(R) \tag{1.12}$$

with the Stefan-Boltzmann constant σ_{SB}. Using Eq. 1.11, we get

$$T(R) = \left\{\frac{3GM\dot{M}}{8\pi R^3 \sigma_{\mathrm{SB}}}\left[1 - \left(\frac{R_*}{R}\right)^{1/2}\right]\right\}^{1/4}. \tag{1.13}$$

In astrophysical models, it is common to focus on larger radii $R \gg R_*$ (Pringle, 1981), which reduces eq. 1.13 to

$$T(R) = T_*\left(\frac{R_*}{R}\right)^{3/4} \tag{1.14}$$

with a characteristic temperature of $T_* = (3GM\dot{M}/8\pi R_*^3 \sigma_{\mathrm{SB}})^{1/4}$.

We can insert this temperature into Planck's law (Planck, 1900),

$$I_\nu = \frac{2h\nu^3}{c^2(e^{h\nu/kT(R)} - 1)} (\mathrm{erg\,s^{-1}\,cm^{-2}\,Hz^{-1}\,sr^{-1}}), \tag{1.15}$$

[2] This assumption does not hold for magnetized neutron stars, where the critical accretion rate is much higher (Mushtukov et al., 2015)

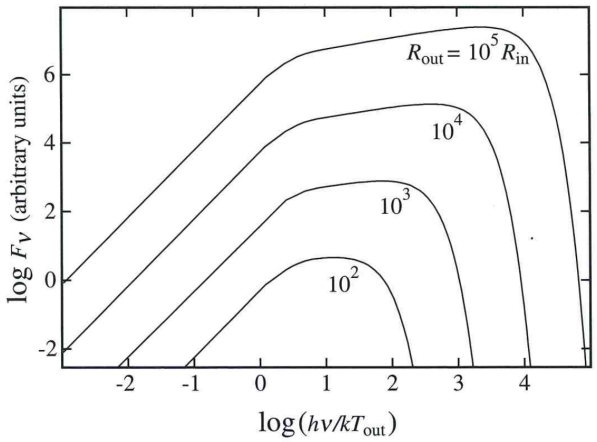

Figure 1.4: Complete spectral shape of a steady, optically thick accretion disk for different extensions of the disk (Frank et al., 2002, Fig. 5.2). One can clearly see the Rayleigh-Jeans limit for lower frequencies, where $F_\nu \propto \nu^2$, as well as the Wien tail at high frequencies, where $F_\nu \propto \nu^3 \cdot e^{-h\nu/kT}$. The flat part in the middle can be approximated with $F_\nu \propto \nu^{1/3}$, making up the characteristic part of a disk.

to get an approximate spectrum emitted at a certain radius of the disk. For an observer at a distance d, observing the system at an inclination i, the flux at the frequency ν from the disk is then

$$F_\nu = \frac{2\pi \cos i}{d^2} \int_{R_*}^{R_{out}} I_\nu R \, dR = \frac{4\pi h \cos i \, \nu^3}{c^2 d^2} \int_{R_*}^{R_{out}} \frac{R \, dR}{e^{h\nu/kT(R)} - 1}. \tag{1.16}$$

Figure 1.4 shows the form of such an accretion disk for several ratios of inner and outer radii. Integrating over a range of temperatures throughout the disk leads to the common denotation "multicolored disk". It serves as a basic model to explain the soft spectral part observed from compact objects (e.g., in the xspec models `diskbb`[3] or `diskpn`[4]), even though many other aspects, such as the elemental composition, ionization stage and viscosity of the disk as well as other properties of the compact object are not considered. Up to now, there are no models available that describe an accretion disk in a more sophisticated way.

1.4 Comptonization

As seen above, already the description of the soft X-ray spectra of accreting compact objects has its difficulties. To depict the hard X-rays in a physical model, however, is even more challenging. The canonical interpretation of the radiation above 10 keV, shaped as a exponentially cutoff powerlaw, is Compton upscattering (inverse Compton scattering, see Compton, 1923, for the original effect) of soft disk photons on relativistic electrons near the compact object. For a scattering angle θ, the photon energy E' after the scattering process is

$$E' = \frac{E}{1 + \frac{E}{m_e c^2}(1 - \cos\theta)} \sim E\left(1 - \frac{E}{m_e c^2}(1 - \cos\theta)\right). \tag{1.17}$$

Depending on the number of scattering processes the photons undergo before they leave the scattering environment, the emerging photon energy distribution looks different. For relatively low optical depths, the sum of the distributions for different numbers of scatterings resembles a power law. Higher optical depths lead to more scattering processes, eventually resulting in a thermodynamic equilibrium between photons and electrons and a Wien spectrum. The exact origin of this Comptonized spectrum is still debated. Proposed geometries

[3] https://heasarc.gsfc.nasa.gov/xanadu/xspec/manual/node162.html
[4] https://heasarc.gsfc.nasa.gov/xanadu/xspec/manual/node168.html

for the Comptonization region include a hot corona around the disk (Haardt & Maraschi, 1991; Dove et al., 1997), a lamppost model with the photon source above the disk (Matt et al., 1992; Martocchia & Matt, 1996), or a jet base model (Markoff & Nowak, 2004).

Comptonization, however, is not the only interaction of the photons with the matter around the compact object: Powerlaw photons are Thomson scattered in the accretion disk, leading to the Compton Reflection hump (e.g., Davis et al., 2005). Photons are absorbed, exciting atoms which then decay via fluorescent line emission. The most prominent example for such an emission line is the Fe Kα line at ~ 6.4 keV (Reynolds, 1999), which can be seen in most sources, but also absorption lines can be observed.

The amount, positions and strengths of such lines strongly depend on the elemental abundance, ionization stage and luminosity in these regions. This becomes most important, if the absorbing matter is located close to the compact object, as is the case for wind-accreting sources. Depending on the line of sight, the X-ray photons emitted during the accretion process pass though the clumpy wind structures and ionize the matter. This can be seen as absorption lines in the spectra, and, with the knowledge of the atomic physics behind the process, allows a deeper insight into the composition and structure of the stellar wind.

1.5 Atomic Structure

Line spectroscopy has always been an important part of astrophysics. Perhaps the most prominent example in modern atomic astrophysics is the detection of the Fraunhofer lines in the solar spectrum (Fraunhofer, 1814): The absorption of photons from the continuous solar radiation by atoms or ions in the solar atmosphere causes dark lines in the spectrum at discrete wavelengths. As it often is the case in the development of science: Fraunhofer himself was not yet able to assign the lines to specific elements as important relations were not yet discovered at his time. Instead, he numbered the lines alphabetically, without any physical meaning. Yet, his nomenclature is still in use today.

The most abundant element in our Universe, hydrogen, provides a great opportunity to highlight the processes that lead to absorption but also emission line features in astrophysical spectra, and can be found in almost all atomic physics textbooks: With only one electron, it is the easiest atom to consider, and also the only one whose equations of state can be solved analytically. This and the following section describe only the basic principles that are necessary for this work. It is based on Pradhan & Nahar (2015), who specifically highlight the astrophysical aspects of atomic physics.

The easiest way to understand the basic principles of atomic structure is to take a look at history, beginning in the 19th century, where atomic processes became more palpable for scientists: The Swiss school teacher Johann Jakob Balmer (1825–1898) analyzed the light caused by electric discharge in hydrogen and found a series of emission lines, the wavelengths of which he was able to describe with the relation

$$\frac{1}{\lambda} = R_{\mathrm{H}} \left(\frac{1}{4} - \frac{1}{n^2} \right) \tag{1.18}$$

with the Rydberg constant for hydrogen $R_{\mathrm{H}} = 1.09677583 \cdot 10^7 \pm 1.3\,\mathrm{m}^{-1}$ and $n = 3, 4, 5, \ldots$

(Balmer, 1885). He then generalized it to

$$\frac{1}{\lambda} = R_{\mathrm{H}}\left(\frac{1}{m^2} - \frac{1}{n^2}\right) \tag{1.19}$$

with $m = 2$ and $n > m$ for the series he had analyzed. Today, this series is known as the Balmer series. Later, also the Lyman series ($m = 1$, Lyman, 1906), the Paschen series ($m = 3$), the Bracket series ($m = 4$) and the Pfund series ($m = 5$) were detected. The physical background for the formalism, however, was still unclear. The planetary model of electrons moving around a central core of protons, although able to explain the outcome of the scattering experiment (Rutherford, 1911) of Ernest Rutherford (1871–1937), does not support stable atoms as the electrons as accelerated charged particles would emit electromagnetic radiation on their orbit around the nucleus, thus lose energy and spiral inward.

Bohr's Atom

The Danish physicist Niels Bohr (1885–1962) then proposed the quantization of angular momentum of the orbiting electrons (Bohr, 1913a,b,c), contradicting the old theorem *Natura non facit saltum*, nature does not jump. He proposed stable angular momenta for the electrons $L = n \cdot \hbar$ as multiples of the Planck constant h divided by 2π. The energy levels resulting from this quantization can be written as

$$E_n = -\frac{\mu e^4}{32\pi^2 \epsilon_0^2 \hbar^2} \frac{1}{n^2} = -13.6\,\mathrm{eV}\,\frac{1}{n^2} \tag{1.20}$$

with reduced mass of electron and proton μ, the fundamental charge $e = 1.6022 \cdot 10^{-19}\,\mathrm{C}$, and the permittivity of free space ϵ_0. In this model, electrons can move between these levels by emitting or absorbing photons of the energy difference of the respective levels, which leads to the line series. Although the model has since been replaced by modern quantum mechanics, it still played an important role in the evolution of atomic physics.

Quantum numbers

At least since Werner Heisenberg (1901–1976) found the uncertainty principle in 1925 (Heisenberg, 1927), the classical picture of an atom did not hold any more: It is not possible to precisely determine both location and momentum of a particle at the same time. Instead, the orbitals of electrons around the cores can be pictured as probability density. They can be described using different quantum numbers:

n The **principal quantum number**, designating the shell of the electron. Shells are counted $n = 1, 2, 3, 4, 5, \ldots$ with the respective shells labeled K, L, M, N, O, P, ..., continued alphabetically. A shell can contain up to $2n^2$ electrons.

In the Siegbahn notation (Siegbahn, 1924), transitions of electrons to the $n = 1$ shell are named K-shell transitions, those into the $n = 2$ shell L-shell transitions, and so on. The difference between origin and destination shell of the transiting electron is denoted by adding a Greek letter: α for $(n + 1)$, β for $(n + 2)$, and so on. Thus, a Kα transition is a transition from $n = 2$ to $n = 1$, Kβ from $n = 3$ to $n = 1$, and Lα from $n = 3$ to $n = 2$.

l The **orbital quantum number**, or orbital angular momentum quantum number, dividing each shell into $l = 0, 1, 2, 3, 4, 5, 6, 7, \ldots, (n-1)$ subshells or orbitals. These orbitals

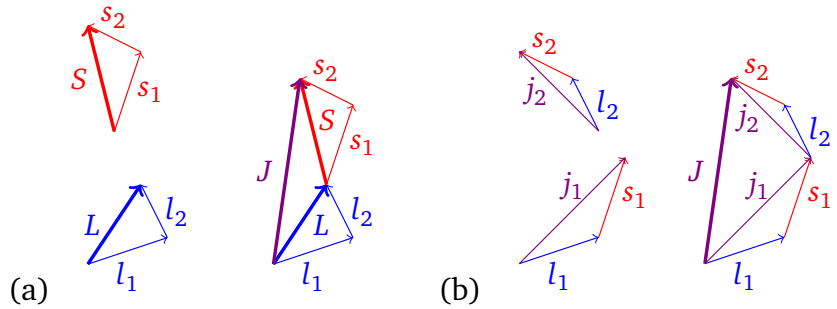

Figure 1.5: Vector representation of the orbital, spin and total angular momenta for *LS*-coupling (a) and *jj*-coupling (b).

are named s, p, d, f, g, h, i, k, ..., for "sharp", "principal", "diffuse", "fundamental", and continued alphabetically. Note that, to avoid confusion, the letter j is skipped.

s The **spin projection quantum number** takes values of $s = \pm 1/2$ for electrons. Each suborbital can contain up to two electrons with opposite spin.

From these three quantum numbers, another three quantum numbers can be derived:

m_l The **orbital magnetic quantum number**, $m_l = -l, -l+1, \ldots, l-1, l$, specifying the spatial orientation of the suborbital. The different m_l become energetically visible once the atom is placed in an external magnetic field. This removal of degeneracy due to a magnetic field is called Zeeman effect (Zeeman, 1896a,b, 1897).

m_s The **spin quantum number**, $m_s = -s, -s+1, \ldots, s-1, s$, defining the spatial orientation of the spin.

Both the orbital angular momentum and the spin angular momentum have to be considered as three-dimensional quantities. The total angular momentum J then is the vector combination of the orbital angular momentum L and the spin S (see Fig. 1.5), which leads to another quantum number:

m_j The **secondary total angular momentum quantum number**, describing the projection of the total angular momentum onto a predefined axis. There are $g = 2j+1$ suborbitals taking values $m_j = -j, -j+1, \ldots, j-1, j$, where $j = |l-s|, \ldots, |l+s|$ in steps of 1[5]. The quantity g is also called statistical weight of the state.

The electron configuration

With these quantum numbers, the state of each electron in an atom or ion can be described. The electron configuration of ions with multiple electrons often follows the pattern

$$n\,l_j^x$$

with $n\,l$ denoting the orbital, j leading to the suborbitals as described above and x being the number of electrons in the respective suborbital[6]. The ground state electron configuration of a helium-like ion would thus be $1s^2_{1/2}$ ($m_j = \pm 1/2$) with two electrons in the K-shell. For a completely filled orbital, the subscript j is often omitted and one simply writes $1s^2$. If another three electrons are added, they will first fill the s orbital of the $n = 2$ shell, the L shell, and then start to populate the p orbital, $1s^2\,2s^2\,2p^1_{1/2}$.

[5] j is also called the main total angular momentum quantum number.
[6] for $x = 1$, x is often omitted

An important rule that has to be obeyed when filling the orbitals is the Pauli exclusion principle (Pauli, 1925): No two identical fermions can occupy the exactly same state at the same time in one system. In the case of multiple electrons in an atom, this means that each electron must have its unique set of four quantum numbers. Note that this principle is not valid for bosons, which have an integral spin.

To describe the energy level of an ion, not only the electron configuration is needed but also information on how these electrons couple with each other. There are two different schemes of coupling commonly used: LS-coupling for low-Z atoms, i.e., atoms with a low number of protons in their nucleus, and jj-coupling for heavier atoms with a higher atomic number Z. Note that the systems rely on different sets of quantum numbers.

LS-coupling

The basic coupling scheme is the LS-, or Russell-Saunders coupling (Russell & Saunders, 1925), which can be used for low-Z elements. Here, as the electrostatic interactions between the electrons outweigh the interactions of orbit and spin in the same electron, the orbital motion and the spin momenta are treated as independent constants of motion. Thus, the relevant quantum numbers in this coupling scheme are (n, l, m_l, m_s). The orbital momenta l_i of the electrons couple and can be added up to a total momentum $L = \sum_i l_i$, as well as the spin momenta s_i to a total $S = \sum_i s_i$ for the whole atom or ion. A total angular momentum can now be obtained: $J = |L-S|, \ldots, |L+S|$. The total symmetry of the state includes L, S, and the parity π and is denoted as

$$^{2S+1}L^{\pi}$$

$(2S+1)$ hereby denotes the spin multiplicity. The parity is negative or odd ($\pi = -1$) if the wave function of the state changes its sign upon reflection. If the sign does not change, the parity is even, $\pi = +1$. For systems that have only one electron per subshell, i.e., systems of non-equivalent electrons, all combinations of l and s are allowed. The Pauli principle has to be applied, however, for equivalent electron configurations.

The multiplicity, or degeneracy, of the atom again is $g = (2J+1)$, g being the statistical weight. For two electrons, J can take the values $J = |j_1 - j_2|, \ldots, |j_1 + j_2|$, leading to the electron states $(j_1, j_2)_J$. The total state includes parity as before,

$$^{2S+1}L_J^{\pi}.$$

The additional J compared to the LS-coupling term denotes the fine structure splitting of the classical LS levels (see Fig. 1.6).

It is not so easy to draw a line between light and heavy elements, depending on their Z. A common, but still arbitrary definition is $Z \leq 18$ (Ar) for light elements, as with the 18th electron, the $3p^6$ subshell is closed, making the nobel gas argon the last element in which the subshells are filled in the obvious order ($1s^2$, $2s^2$, $2p^6$, $3s^2$, $3p^6$). The next electron would then go in the 4s subshell rather than in the 3d subshell for the ground state.

jj-coupling

With growing Z, relativistic effects become more and more important for the electrons as the electron-nuclear force increases[7], the orbital and spin angular momenta of an electron

[7] Note that for intermediate atomic numbers, neither of the coupling schemes gives an exact description. There is no region of overlap.

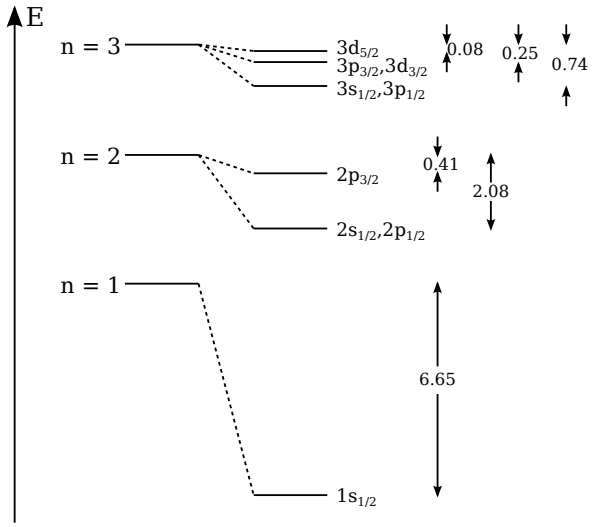

Figure 1.6: Fine structure splitting of the hydrogen energy levels of the K, L and M shells (Hell, 2017, Fig. 3.1, sketch after Friedrich 1990). Denoted in numbers are the energy differences in units of 10^{-6} atomic units.

couple to $j_i = l_i + s_i$ with each other first. Only in the second step, those j_i couple between the electrons to a total angular momentum $J = \sum_i j_i$. The relevant quantum numbers then are (n, l, j, m_j).

Level sorting

To determine the transition energy of electrons moving between these levels, the energy and level order has to be considered. For the most easy cases of LS-coupling, Hund (1925) developed three empirical rules:

S-rule The LS term with the highest spin multiplicity $(2S + 1)$ has the lowest energy: The spins of the electrons tend to be parallel where possible. This leads to a large distance between the electrons and thus to a minimum in Coulomb interaction, which is the dominating factor in LS-coupling.

L-rule For terms with equal spin multiplicity, the term with larger total L has the lower energy: The farther the shells are away from the nucleus, the larger tends to be the distance between the electrons in these shells.

J-rule For subshells that are less than half filled, the level with the lowest J has the lowest energy. For more than half filled subshells on the other hand, the level with the highest J has the lowest energy.

Hund's rules are to be applied in this order, the first rule depicts the strongest effect, etc.. Note, however, that these rules are purely empirical, and valid only for the ground state. Exited atoms already need exceptions from these rules and for more complex configurations, there are increasing deviations. To determine an exact scheme, the Schrödinger equation (Schrödinger, 1926b,a)

$$\underbrace{\left[-\frac{\hbar^2}{2m}(\nabla^2) + V(r)\right]}_{H}\psi = E\psi \tag{1.21}$$

where H denotes the Hamiltonian with the Coulomb potential (Coulomb, 1785a,b)

$$V(r) = -\frac{Ze^2}{r} \tag{1.22}$$

and the wave function for the state (n, l, m_j)

$$\psi_{n,l,m_j} = \frac{1}{\sqrt{2\pi}} R_{n,l}(r)\, \theta_m^l(\vartheta)\, e^{im\varphi} \tag{1.23}$$

for the non-relativistic case would have to be solved. This is possible analytically for the simple case of a hydrogen atom, but not for systems containing more electrons, where not only the interaction between a single electron and the nucleus have to be taken into account, but also the interactions between the different electrons themselves. For example, the potential V for a two-electron system already complicates to

$$V(r_1, r_2) = -\frac{Ze^2}{r_1} - \frac{Ze^2}{r_1} + \frac{e^2}{|r_1 - r_2|} \tag{1.24}$$

where the negative terms account for the central Coulomb potential for each electron and the positive term for the electron-electron interaction. More terms are added as the number of electrons increases. To find a solution for these cases numerically, a trial function containing adjustable parameters has to be used. A common method is the Hartree-Fock-method (Fock, 1935), using a self-consistent iterative approach. The most challenging aspect here is the treatment of the repulsive electron-electron interaction terms. To simplify the calculations, the radially symmetric part of these interaction potential, and the Coulomb potential of the nucleus are merged into one central field potential, whereas the non-radial part is neglected. Further approximations are made when including relativistic effects such as the spin-orbit interaction leading to the fine structure splitting (Sommerfeld, 1940). By now, there are extensive databases which try to compile the best of available data for general users. They contain level energies for various electron configurations (NIST[8]) and, to some extent, also transition energies (AtomDB[9]).

1.6 Atomic Processes

In our Universe, which is much less empty than one might expect, atoms and ions will interact with their surroundings, i.e., other electrons, atoms, ions, or photons. This section will highlight the processes most relevant for astrophysics.

An atom normally prefers to be in its ground state, i.e., the electron configuration is such that the potential energy of all electrons is minimum. If then an electron gains energy from the outside, there are two possibilities: Either the amount of gained energy is large enough to free the electron from the potential well and moving it into the continuum above the discrete energy levels, leaving back an ion, or the amount of energy is smaller and only enough to lift up the electron to a higher energy level, now forming an excited atom. Of course it is possible in the same way to further ionize or excite an ion, or even to have more than one excited electron in a system. Equivalent to the atom, an ion in the ground state has the energetically lowest electron configuration. Note that ground state ions of different species but with the same number of electrons (iso-electronic sequence) tend to have the same electron configurations and, although the order of the levels changes as a function of

[8] https://www.nist.gov/pml/ground-levels-and-ionization-energies-neutral-atoms
[9] http://www.atomdb.org/index.php

Z, they show similar behavior with similar transitions and spectra. This is the reason that often ions are referred to by their iso-electronic sequence: H-like ions have one remaining electron, He-like ions have two remaining electrons, etc.. It is possible for ions to capture passing electrons to one of their energy levels, releasing the difference in energy, $E_{\text{kin}} + E_{\text{pot}}$ where E_{kin} is the former kinetic energy of the captured electron and E_{pot} is the ionization energy of the recombined ion. The cross-section for this process, however, decreases with increasing E_{kin}, making it less likely for fast electrons. In general, there are two kinds of processes:

Excitation and ionization processes An electron can be excited either by absorbing a photon (photo-excitation) or by the transmission of kinetic energy of a passing particle or photon (collisional excitation). The electron then moves to an energetically higher level (bound-bound transition). For both processes, if the energy transmitted to the bound electron is large enough, the electron is raised to the continuum (bound-free transition) and one talks of photo-ionization and collisional ionization. Note that photo-excitation is a resonant process, i.e., the photon energy has to match the transition energy.

Recombination processes An ion with its positive charge can capture a passing electron. The electron then falls into the potential well, releasing the excess energy, which – if it is the right amount of energy – is absorbed internally by exciting another electron in the system (dielectronic recombination), leading to a doubly excited state. Dielectronic recombination therefore is a resonant process. For other amounts of excess energy, this energy is transported away by the emission of a photon (radiative recombination), leading either to the ground state or to an excited state, depending on the energy level the electron is captured into.

De-excitation processes Finally, to de-excite an electron, a photon is emitted with an energy according to the energy difference of the start and end levels of the transition. This process can happen spontaneously or it can be induced to make the transition by an external electromagnetic field (stimulated emission). An electron does not always directly de-excite to the ground state, but can also de-excite in several steps, leading to a cascade of several photons.

In some cases, it is possible that the energy released by de-exciting an electron is directly absorbed again and used to raise another electron to the continuum. This process, basically the inverse of dielectronic recombination, is called auto-ionization.

Selection rules

As the electrons gain or lose energy, it is not possible for them to arbitrarily move between different energy levels. Some transitions appear to be preferred over others, and some transitions only occur under very special conditions. The expectation value M_{if} of the transition dipole momentum integral

$$\mathbf{M}_{if} = \int \psi_i \mathbf{r} \psi_f^* \mathrm{d}^3\mathbf{r} \tag{1.25}$$

depends on both the initial (i) and final (f) state. At least one of the three spacial components of the integral have to be non-zero for a transition to be possible. This leads to certain restrictions on the $(n, l, m_j)_i$ and $(n', l', m_j')_f$ of the initial and final state:

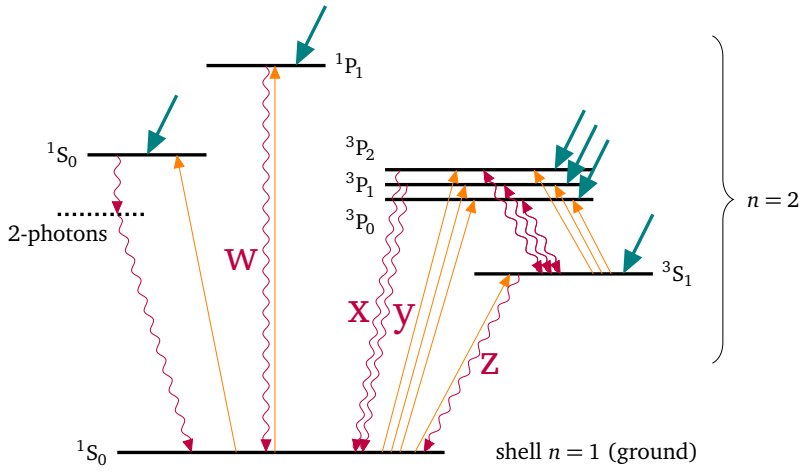

Figure 1.7: Simplified Grotrian diagram for the $n = 1$ and $n = 2$ shells of helium with all possible transitions (after Porquet et al., 2001, Fig. 1). Orange arrows demark collisional excitation, thick blue arrows demark radiative and dielectric recombination, curved purple arrows are radiative transitions.

- $\Delta J = J' - J = 0, \pm 1$ (but not $J' = J = 0$)
- $\Delta M = M' - M = 0, \pm 1$ (but not $\Delta m = 0$ if $\Delta J = 0$)
- Parity change
- $\Delta l = l' - l = \pm 1$
- $\Delta S = 0$ (for LS-coupling)
- $\Delta L = 0 \pm 1$ (for LS-coupling)

Transitions that satisfy these conditions are called (electric) dipole-allowed, or E1 transitions. They account for the majority of observed transitions in the laboratory. There are, although with a much smaller probability and transition rate, also transitions that violate these rules: magnetic dipole (M1), electric quadrupole (E2) and magnetic quadrupole (M2) transitions do occur. They follow modified selection rules, for a comprehensive table see, e.g., Garstang (1962, , Table 1).

A common way to sketch energy levels and transitions between them is the Grotrian diagram (Grotrian, 1928) as shown in Fig. 1.7 for a He-like system. The prominent transitions are labeled

- w ($1s2p\,^1P_1 \rightarrow 1s^2\,^1S_0$),
- x ($1s2p\,^3P_2 \rightarrow 1s^2\,^1S_0$),
- y ($1s2p\,^3P_1 \rightarrow 1s^2\,^1S_0$)
- z ($1s2s\,^3S_1 \rightarrow 1s^2\,^1S_0$)

after Gabriel (1972), but one can also find the labels r (resonance line, for w), i (intercombination line, for x and y, which cannot be resolved for low Z ions as the levels are very close to each other), and f (forbidden line, for z). The latter is a M1 transition, which nonetheless can be observed as the $^3P_0$ level has no way to directly decay to the ground state, and instead populates the $^3S_1$ level. This enhanced population makes the transition visible despite of it being a very slow transition. Similarly, the $n = 2$ $^1S_0$ level cannot directly decay to the ground state by emitting a single photon, leading to a two-photon decay via an additional virtual level. This term scheme, although with deviations in the energies of the levels, can be applied to all He-like ions, i.e., ions with two remaining electrons. The ratios of the w, x, y, and z lines are sensitive to the electron density and electron temperature in collisionally ionized and photoionized plasmas (Porquet & Dubau, 2000, and references therein).

2

Said Wilbur Wright, 'Oh, this is grand,
but, Orville, you must understand:
We've discovered all right
The secret of flight –
The question is, how do we land?'

(Frank Richards)

And how to observe them?

As mentioned before, the Earth's atmosphere is opaque to X-rays. To observe them, one cannot simply set up a telescope somewhere and point it to the sky, but one has to put a detector up above the atmosphere. With their high energies, X-rays also require different setups and technologies to be focused and detected than what has been known from optical astronomy. This chapter summarizes the history of X-ray astronomy and highlights current observing methods as they are in use on different X-ray observatories.

2.1 First efforts

X-ray astronomy was born in the late 1940s when, for the first time, a detector placed inside a captured V2 missile was launched. The rockets reached an altitude just above the atmosphere, carrying photographic plates with optical filters of Beryllium and Aluminum of varying thickness or basic Geiger counters. First spectra of solar X-rays were obtained with a Bragg crystal spectrometer in the early sixties (see Keller, 1995, for a summary of early X-ray astronomy).

The main problem – apart from a small field of view – with experiments onboard such missiles was time: Only a few minutes per flight were spent high enough for X-rays to reach the detector. Balloon flights were the only alternative available then. Although limited in flight height and thus still affected by absorption due to the atmosphere, balloon-borne experiments were able to observe much longer. Clark (1965) reports on the first hard X-ray spectrum of the Crab nebula taken during a balloon flight. The detector used in this experiment was a scintillation counter: Large crystals coupled to photomultiplier tubes. The crystals are of material that absorbs the ionizing X-ray radiation and emits the excess energy by emitting photons at a specific wavelength. These photons are recorded by the photomultiplier tubes. Electronic thresholds allow for a rough resolution in energy. With the invention of phoswich detectors that allowed to couple several scintillation counters by a distinction in pulse shape, and with improved shielding to reduce instrumental background as well as background from cosmic rays, these early detectors quickly grew better.

With the rapid technical progress, it was possible in the 1960s and 1970s to start building space qualified experiments. The first satellite dedicated to the observation of X-rays was *Uhuru* (Giacconi et al., 1971), which was launched into low earth orbit in 1970 and carried two sets of proportional counters. During its tree years of mission time, *Uhuru* performed the first X-ray all-sky survey. The 339 sources detected with the *Uhuru* satellite can be found

in the fourth *Uhuru* catalogue (Forman et al., 1978) and can be recognized by the "4U" in their source identifications. But not only satellites were used to carry X-ray detectors: The first scintillation detector to go into space was the *High Energy X-ray Experiment* or *HEXE* onboard the Russian space station *Mir* (Reppin et al., 1985).

X-ray astronomy has developed rapidly since these beginnings. The number of known sources grew steadily with better and better detectors and increasing observing time. *Uhuru* was followed, amongst others, by

- the *High Energy Astronomy Observatory (HEAO)* program (Tucker, 1984) with its three missions
  - *HEAO1* (1977–1979; Gursky et al., 1978; Matteson, 1978; Rothschild et al., 1979),
  - *HEAO2* (also known as the *Einstein observatory*, 1978–1981; Giacconi et al., 1979), and
  - *HEAO3* (1979–1981; Schwartz et al., 1987; Wheaton et al., 1989; Mahoney et al., 1980),
- the *European X-ray Observatory Satellite* (*EXOSAT*, 1983–1986; Taylor et al., 1981),
- the *Ginga* satellite (Japanese for "galaxy", 1987–1991; Turner et al., 1989; Tsunemi et al., 1989; Murakami et al., 1989),
- the *GRANAT*[1] satellite (1989–1994 (1998)[2]; Brandt et al., 1990; Roques et al., 1990; Siuniaev et al., 1990),
- *ROSAT* (short for "Röntgen-Satellit", 1990–1999; Trümper, 1982),
- the *Compton Gamma Ray Observatory* (*CGRO*, 1991–2000; Kniffen, 1989)
- the *Advanced Satellite for Cosmology and Astrophysics* (*ASCA*, 1993–2001; Tanaka et al., 1994)
- the *Rossi X-ray Timing Explorer* (*RXTE*, 1995–2012; Jahoda et al., 1996), and
- *BeppoSAX*, named after Giuseppe "Beppo" Occhialini, an Italian physicist, the *SAX* standing for "Satellite per Astronomia a raggi X" (1996–2002; Boella et al., 1997)

This list of course continues until today and will continue even further (see Sect. 2.3 for a detailed description of the observatories that provided the data for this thesis). The rapid development, however, was – and still is – accompanied by an increasing sensitivity of the instrumentation, not only regarding the detection and measurement of X-ray radiation but also to damaging radiation as well as the impact of micrometeorites (see Abbey et al., 2006, for damages due to impact events on two current satellites).

An increasing danger to satellites as well as human space travel, e.g., to the International Space Station (ISS) is space debris: Decommissioned satellites, not only scientific ones but also military or commercial ones, often run out of fuel and de-orbit uncontrollably. Collisions, even if only between space debris parts, leave smaller pieces that are more difficult or even impossible to track. Larger parts falling down back to Earth cannot be controlled to come down in unpopulated regions. The last satellite to re-enter Earth's atmosphere as of January

[1] The acronym "GRS" in various source names stands for "*Granat* source".
[2] Between 1994 and 1998, *GRANAT* observed without attitude control in a non-directed survey mode

2019 was *RXTE*, which burned up due to friction in the atmosphere on April 30, 2018[3]. Luckily, there were no confirmed injuries or damage due to falling satellites so far. For the last years, NASA as well as ESA require missions they participate in in funding to be built in a way that they can safely and especially controlledly be brought to re-enter the atmosphere on a pre-calculated path.

2.2 Focusing and detection of X-rays

For different aims, several methods to collect X-rays have been developed over time. This section now introduces the techniques used in the current observatories. For more details, see, e.g., Trümper & Hasinger (2008), which served as a reference for most of this chapter.

Similar to optical astronomy, it is not only possible to correlate incident X-rays with a source, but also to focus them onto a detector or a grating to dissemble them into different energies. Due to the high energy of X-rays, however, there are some differences.

2.2.1 Wolter mirrors

Not only optical photons can be reflected by mirrors, it is also possible to focus even high energy radiation (see, e.g., Trümper & Hasinger 2008 or Aschenbach 2009 for a detailed description). Snell's law

$$\frac{\sin\alpha_1}{\sin\alpha_2} = \frac{n_1}{n_2} \tag{2.1}$$

with the incident angle α_1 and the angle of the outgoing ray α_2 as well as the refraction indices of the respective material, n_1 and n_2, is still valid. Assuming that the X-rays come from vacuum, the refraction index $n_1 = 1$. For total reflection, the outgoing angle, measured from the perpendicular to the reflecting surface, has to be $\alpha_2 > 90°$. The critical incident angle then is

$$\alpha_{\text{crit}} = \arcsin n_2. \tag{2.2}$$

The refraction index

$$n_2 \equiv n = 1 - \delta - i\beta \tag{2.3}$$

is dependent on the reflecting material. Here, δ accounts for the phase change and β for the absorption, both dependent on the incident photon energy. For X-rays, both constants are small but not zero, implying on the one hand the impossibility of total reflection – some radiation also will be absorbed – and on the other hand a very small deviation from unity. The critical angle thus is close to 90°: To be reflected, incident rays have to be almost parallel the reflecting surface. When using X-rays, it is therefore more common to use the grazing angle, i.e., the angle between the incoming photon and the reflecting surface, instead of the incident angle, i.e., the angle to the perpendicular of the surface. Neglecting for the moment the imaginary part of the refraction index, Equation 2.2 then translates to

$$\cos\alpha_{\text{crit}} = 1 - \delta. \tag{2.4}$$

Wolter (1952) first used this relation to design a set of mirrors which together are able to

[3] https://www.space.com/40592-nasa-rxte-satellite-falls-to-earth.html

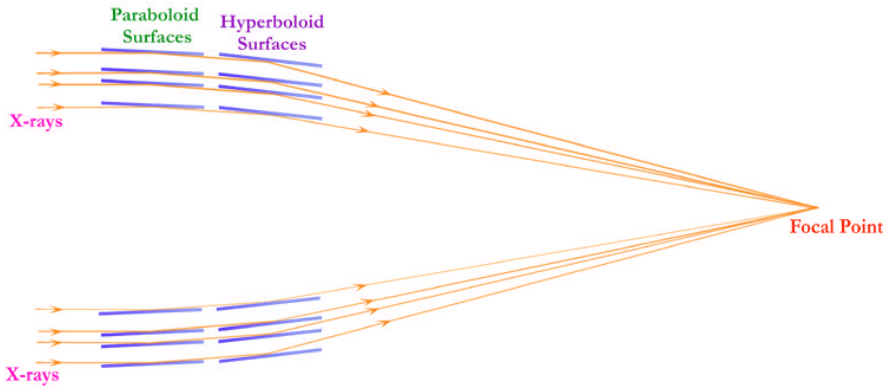

Figure 2.1: Sketch of a Wolter mirror system with four nested paraboloid and hyperboloid mirrors that focus incoming X-rays (http://chandra.harvard.edu/resources/illustrations/teleSchem.html).

focus X-ray radiation properly. To do this, the systems have to satisfy Abbe's sine condition (Abbe, 1881), that in order to get a sharp image of both on-axis and off-axis objects, the distance from the principal surface, i.e., the mirror surface, to the focus has to be equal for all paraxial rays. This is easy to fulfill using optical light and a single mirror, where incident and outgoing angles are very small. For large incident angles or accordingly small grazing angles as needed for X-rays, this is no longer the case. Wolter (1952) solved this with a system of two consecutive mirrors. He proposed several possible arrangements, for one of which several mirror shells can be nested into each other to increase the effective area (Wolter Type I). This configuration consists of first a paraboloid reflection surface followed by a hyperboloid reflection surface. The shells nested inside each other focus the X-rays to one focal point by double reflections (see Fig. 2.1). The shallow angles cause the focal length

$$f = \frac{r}{\sin 4\alpha} \tag{2.5}$$

for an aperture of $2r$ with lengths of up to 10 m to be quite long. This of course is a challenge for satellite missions (Giacconi & Rossi, 1960) where size as well as weight – additional mirror shells to increase aperture are heavy – play an important role in the total costs. A creative solution is shown by the *NuSTAR* satellite with its extendable optical bench that was only deployed once the satellite was in orbit (Harrison et al., 2005). To achieve the best possible image, it is essential to polish the mirror surfaces to a minimum of micro-roughness. Coatings of iridium and gold are common for X-ray satellites.

A relatively new technique are silicon pore optics (SPO; see, e.g., Collon et al., 2006): Rectangular slots are cut out of a silicon wafer with extremely small surface roughness such that only a thin framework of silicon remains. The wafers then are curved to resemble the Wolter shape described above. Although it is only possible to approximate the exact paraboloid and hyperboloid shapes, there are only minor losses in angular resolution, whereas the effective area to weight ratio can be increased massively[4]. The *Advanced Telescope for High Energy Astrophysics* (*Athena*) will be the first observatory using this new technique (Barcons et al., 2012).

[4] https://www.cosmos.esa.int/web/athena/silicon-pore-optics

2.2.2 Coded masks

An alternative to the focusing of the X-rays onto a detector is to put a collimator in front of the detector: X-ray absorbing barriers narrow the field of view. If a detector with a collimator moves over an X-ray source, the counts from this source reaching the detector will first increase up to a maximum value where the source is located directly on the line of sight, and will decrease again when the detector is moving on. The amount of X-rays reaching the detector is called response; the collimator response has the shape of a triangle. With this technique, a single proportional counter is able to roughly reconstruct the brightness of sources it is moving over in a not so crowded region on the sky.

Instead of a temporal modulation of aperture as is the case when moving a collimator over a source, it is also possible to spatially modulate the aperture. This process requires a position-sensitive detector. A patterned mask produces a shadow pattern on the detector for each source in the field of view, which can be limited by an additional classic collimator. These patterns are superimposed on the detector and the original sky image has to be calculated ("unfolded") via the coding equation

$$D(x) = M(x) \times S(x) \tag{2.6}$$

with the observed detector image D, the original sky image S and the modulation function M which describes the coding pattern of the mask. An example for such a coded mask telescope can be seen in Fig. 2.2, right, for the *INTEGRAL* satellite.

There are some major caveats to this method: regardless how ideal the mask pattern is designed, it is not possible to find a unique solution for the original sky image. Depending on the count rates and their Poisson distributed uncertainties, as well as on the diffuse X-ray background present on the sky, the uncertainties on the unfolded sky image can be large. Unwanted counts from incident high energy particles or secondary photons caused by photons or particles cannot be distinguished from the wanted source photons and add an additional uncertainty. Variations in sky background can cause artifacts in the unfolded sky image. Combining the coded mask with a sort of modulated aperture can minimize this effect: Instead of a single, pointed observation, the optical axis is stepped over the region of interest in a given pattern ("dithering"). Currently, both the *INTEGRAL* and *Swift* satellites successfully use coded mask instruments.

2.2.3 Charge coupled devices

Similar to the optical waveband, the detection of X-rays has made a huge step forward with the invention of Charge coupled devices (CCDs, Boyle & Smith, 1970; Amelio et al., 1970), which have been refined for use in X-ray astronomy in the 1980s and 1990s (Clarke, 1990, 1994) and provide an increased timing and spectral resolution.

The basic concept of a CCD (for a detailed description, see Bradt, 2004; Lesser, 2015) is to create a depletion zone in a semiconducting material, mostly a silicon wafer. This zone where there are no electrons in the valence bands of the silicon atoms, can be achieved via doping the silicon crystal with atoms of other species, called a pn junction, as well as the application of a voltage on this pn junction. Incident photons will free electrons in the depletion zone. These electrons are drained from the zone by the electric field before being

able to recombine. The resulting current gives information on the energy of the incident photon. A CCD is a rectangular arrangement of several hundreds of such pn junctions, or "pixels", separated by physical potential barriers between columns ("channel stops") and voltage-induced potential barriers between the rows. The electrons released by the incident photon are thus saved in a potential well for each pixel. Successively reading out these pixels allows to reconstruct the location of the photon on the chip.

Whereas for optical light a depletion zone of only a few micrometers is sufficient, the high energy of X-ray photons necessitate a larger depletion zone (Bradt, 2004). For optical CCDs, the side exposed to the photons typically is the one which also carries the wiring for the pixels, i.e., the front side. Backside-illuminated CCDs are more challenging to manufacture, but have major advantages in X-ray astronomy: They have a larger effective area as there is no shadowing, are more sensitive especially to soft X-rays, and the readout process is more time-efficient. A further increase in time resolution are frame store CCDs, where the charge from the exposed CCD is first moved to another, shielded CCD of equivalent size, which is then read out during the next exposure, leading to a much shorter dead time. The readout time then ranges in the millisecond area.

On the other hand, CCDs do have their caveats (Trümper & Hasinger, 2008): For low energetic photons, the quantum efficiency of an X-ray sensitive CCD is limited by less sensitive layers. Large parts of this low photon energy is not disposed by producing free electrons but by creating lattice vibrations ("phonons") in the crystal. The complicated electronics not only add various noise components but are also subject to radiation damage in space, leading to a decrease in charge transfer efficiency (CTE).

A new generation of detectors uses active pixel sensors (APS; Treis et al., 2004), which unite the detector and a first amplifier in for each pixel. They make charge transfer unnecessary, eliminating the degradation of the CTE. Such a detector will be used for the *Athena* Wide Field Imager (WFI, Barcons et al., 2012)

2.2.4 Transmission Gratings

The atomic processes described in Section 1.6 can be observed in the very soft X-rays. The development of CCDs for the first time allowed observations in this energy region. Physical insights, however, were limited due to the still low energy resolution. Again, it was possible to transfer techniques from optical astronomy into the X-ray region: Transmission gratings put into the spectral path between the Wolter mirrors and the CCD disperse the incoming radiation depending on its energy E according to Bragg's law (Bragg & Bragg, 1913)

$$\sin\alpha = \frac{m\,h\,c}{E\,d}. \tag{2.7}$$

The dispersion angle α thus depends on the diffraction order m and the grating spacing d, together with the speed of light c, the Planck constant h. The improved geometry of Rowland (1882, 1883) reduces optical aberrations.

A grating disperses the radiation into different orders. Depending on the grating spacing and the incident photon energies, it can happen that subsequent diffraction orders are overlapping on the detector. For a CCD, it is relatively easy to distinguish between photons of different orders. In case of a detector without energy resolution, e.g., a microchannel plate

detector as for the *Chandra* low energy transmission grating (Kraft et al., 2000), the grating characteristics have to be chosen such that the even dispersion orders are suppressed, which can be achieved for a ratio of bars to period of $a/d = 0.5$ (Trümper & Hasinger, 2008). When planning observations, one also has to keep in mind that off-axis sources that are in the field of view their spectra should not overlap on the detector.

2.3 Current X-ray satellites

With the rapid technical development of the last decades, today's fleet of X-ray observatories in space is very strong, as specialists from countries around the world join their expertise in international collaborations. The most obvious place to look for X-ray satellites are orbits around Earth. To avoid damage to the mission and contamination of its observations, Earth's inner radiation belt, which contains mainly high energy protons, has to be avoided. Satellites in a nearly circular low Earth orbit are located just below this belt, e.g., *Swift* or *NuSTAR* at a height of $\sim$ 600–650 km. Above the radiation belt, elliptical orbits are preferred to allow for longer uninterrupted observations.

In almost[5] all cases, satellites are launched by rockets either directly into their operational orbit or, e.g., in the case of *INTEGRAL*, into a transfer orbit which is then corrected by the spacecraft's own propulsion system. This way, also a later correction of the orbit is possible, e.g., to avoid collisions with space debris or to re-adjust the evolving orbit after some time.

All satellites orbiting around Earth also follow the Earth around the sun. They cannot, however observe every direction on the sky at every day of the year. The sun is a very bright source which would not only contaminate observations but might even damage instruments on board due to high count rates or due to the increase in temperature. In addition, to ensure the power supply for the electronics, the solar panels of the satellites may only have a maximum angle away from the sun. Similar arguments prevent instruments from having, e.g., the moon or nearby bright planets in their field of view. This leads to observational constraints that are individual for each satellite and have to be taken into account when planning observations.

Following various missions in the microwave, infrared and optical wavebands, *Athena* will be the first X-ray mission that is not in orbit around Earth but around the second Lagrange point[6] of the Earth-Sun system at a distance of $\sim 1.5 \cdot 10^6$ km from Earth. The far-out location, though more difficult and expensive to reach, bears advantages over orbits around the Earth, too: It is easier to maintain a constant orbit over a longer time, as well as to sustain a constant temperature onboard the satellite due to the uniform irradiation of the sun. Long, uninterrupted observations are easy to achieve for this kind of orbit.

International collaboration is not only the core for the development of the missions but also for their maintenance: Data that are collected in space have to be transmitted to the observers on Earth, and the observing schedule with all necessary information has to be uploaded onto the spacecraft. This happens during downlink periods to ground stations

[5] The *Chandra* mission is an exception here, being the only satellite that was deployed by a NASA Space shuttle.
[6] A detailed description of the Lagrange points in the gravitational potential of a two-body system can be found in Chapter 3.

on Earth, e.g., the Deep Space Network[7]. The telemetry rate available also sets limits for observations of bright sources where large amounts of data are collected over a very short time. Different observational modes as well as onboard data processing try to compensate for that.

Each of the observatories has its special abilities, allowing the observers to pick the one that is best suited for the purpose of their observations. This section will now highlight a subset of X-ray satellites, whose observations are part of this work.

2.3.1 Chandra

The *Chandra* mission, named after the Nobel laureate Subrahmanyan Chandrasekhar (1910–1995), is the oldest of the missions used for this work. Launched on July 23, 1999, its specialty are observations of faint sources even in crowded fields with a large collecting area and high spatial resolution. Four nested Wolter I mirror shells coated with iridium, with a focal length of 10.066 m focus the X-rays from a field of view with a diameter of 30' onto the focal plane. There, observers can choose between four different detection methods: The Advanced CCD Imaging Spectrometer (ACIS, Garmire et al., 2003) where CCDs are placed either as a 2×2 imaging array or a 6×1 spectroscopic array, or the High Resolution Camera (HRC) for imaging (HRC-I, 90×90 mm; Murray et al., 2000) or spectroscopic purposes (HRC-S, 300×20 mm; Kraft et al., 2000), consisting of CsI-coated microchannel plate detectors. A Low Energy Transmission Grating (LETG, Brinkman et al., 2000) spectrometer can be inserted for either ACIS-S or HRC-S. It is able to disperse photons in the energy range of 0.07–8.86 keV, depending on which detector is used. The High Energy Transmission Grating (HETG, Canizares et al., 2000, 2005), consisting of a High Energy Grating (HEG, 0.8–10.0 keV) and a Medium Energy Grating (MEG, 0.4–5.0 keV), can be combined with ACIS-S only.

There are two observation modes available[8]: Timed Exposure (TE) and Continuous Clocking (CC) mode. For the TE mode, the exposure of each frame can be chosen between 0.2 and 10.0 seconds for the full frame or a subarray. The ACIS instrument uses frame store CCDs, and as the framestore readout time is 3.2 s for a full frame, exposures below this value, e.g., due to high count rates of bright sources, lead to dead times between individual frames. If one can spare one spatial dimension, however, the CC mode offers a 3 ms timing resolution: Data are then continuously shifted (clocked) through the exposed and the frame store CCD to be read out.

2.3.2 *XMM*

The X-ray Multi-Mirror mission (Jansen et al., 2001), called *XMM*-Newton in honor of Sir Isaac Newton (1643–1727), was launched half a year after *Chandra*, on December 10, 1999. *XMM*[9] features not only one but three Wolter I mirror systems of 58 nested shells each. Two of these mirror systems have a Reflection Gratings Spectrometer (RGS, den Herder et al.,

[7] https://eyes.nasa.gov/dsn/dsn.html
[8] See "Operating Modes" in http://cxc.harvard.edu/proposer/POG/html/
[9] See https://xmm-tools.cosmos.esa.int/external/xmm_user_support/documentation/uhb/ for the user handbook

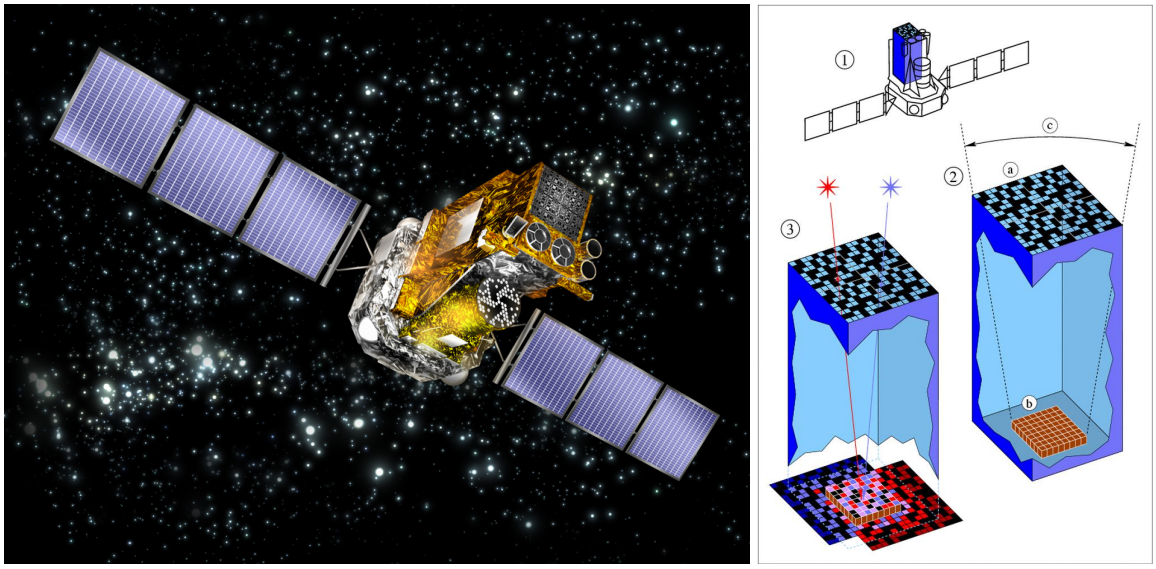

Figure 2.2: Left: Artist's impression of the *INTEGRAL* satellite (https://www.isdc.unige.ch/integral/gallery.cgi?INTEGRAL). Clearly visible are the IBIS (big square) and JEM-X (circles below the square) coded masks and the star trackers (black circles to the right) pointing towards the upper right, as well as the SPI (big cylinder below the square).
Right: Image reconstruction for a coded mask instrument (https://www.cosmos.esa.int/web/integral/instruments).

2001) in their optical paths. The dispersed photons are detected by the RGS focal cameras, consisting of frame store MOS CCDs. The available observation modes are "spectroscopy", which is the standard observation mode, and the "small window" mode, which is only used for extremely bright sources. Time resolution in the "spectroscopy" mode is 4.8 s for the RGS1 and 9.6 s for RGS2, which is only read out by a single node since August 2007. In the "small window" mode, only the central quarter of the CCD rows will be read out, reducing the exposure by a factor of four.

Additionally, *XMM* carries an optical monitor (OM; Mason et al., 2001) and three European Photon Imaging Cameras (EPICs), two of which are Metal-Oxide Semiconductor (MOS) CCDs (Turner et al., 2001), the third being a pn-CCD (Strüder et al., 2001). A wide selection of different observation modes is available for the EPICs[10], with time resolutions of some μs (burst mode) to a few seconds (full frame MOS CCD) and different effective areas. Like *Chandra*, *XMM* is sensible for the soft X-rays below 10 keV.

2.3.3 *INTEGRAL*

Next to *XMM*, the International Gamma-Ray Astrophysics Laboratory (*INTEGRAL*, Winkler et al., 2003) is the second of two missions in this subset built by the European Space Agency (ESA). It was launched on October 17, 2002 and is intended to observe in the hard X-ray range. Complementary to the previously discussed missions, *INTEGRAL*'s main instruments, the Imager on Board the *INTEGRAL* Satellite (IBIS, 15 keV–10 MeV; Ubertini et al., 2003) and

[10]For an extensive description, see the according section of the *XMM*-Newton Users Handbook at https://xmm-tools.cosmos.esa.int/external/xmm_user_support/documentation/uhb/epicmode.html

the SPectrometer on *INTEGRAL* (SPI, 18 keV–8 MeV; Vedrenne et al., 2003) are designed to observe the hard X-ray and Gamma ray photons. SPI consists of an array of 19 Germanium detectors with an energy resolution of 2.2 keV. With a coded mask, it is able to provide an angular resolution of 2.5°. The IBIS, also a coded mask instrument (see Fig. 2.2) has an angular resolution of 12'. two detector planes. The top layer, called Integral Soft Gamma-Ray Imager (ISGRI, Lebrun et al., 2003), consists of 128 × 128 CdTe pixels arranged in 8 modules with 64 × 32 pixels each. Below the ISGRI, the PIxellated Caesium Iodide (CsI) Telescope (PICsIT, Labanti et al., 2003) as a separate detector allows for a reconstruction of the direction of incident high energy photons interacting in both layers (Compton operation mode). IBIS as well as SPI are both shielded from background radiation by a mantle of tungsten and lead.

To ease the identification of Gamma ray sources detected by IBIS and SPI, the Joint European X-Ray Monitor (JEM-X, 3–35 keV; Lund et al., 2003) with its two gas chamber detectors behind yet another coded mask provides arcminute angular resolution of the observed sky region. *INTEGRAL*, too, carries an optical monitoring camera (OMC, Mas-Hesse et al., 2003).

2.3.4 *Swift*

The Neil Gehrels *Swift* observatory (Gehrels et al., 2004), named in honor of its principal investigator Neil Gehrels (1952–2017), was launched on November 20, 2004. It is intended to detect Gamma ray bursts (GRBs) and quickly start follow-up observations. For this purpose, it is designed as a multiwavelength mission, carrying the Burst Alert Telescope (BAT, 15–150 keV; Barthelmy et al., 2005), the X-ray Telescope (XRT, 0.2–10.0 keV; Burrows et al., 2005), and the Ultra-Violet/Optical Telescope (UVOT, 170–650 nm; Roming et al., 2005).

The specialty of *Swift* is its ability to move autonomous, quickly and precisely to a position where a new GRB is detected by the BAT instrument. The coded mask instrument with a large field of view of 1.4 sr can trigger a GRB observation with an initial position of 4' precision, causing the spacecraft to slew to this position for additional observations. With its large field of view, however, BAT provides not only information on GRBs but along the way collects long term hard X-ray survey data of the complete sky.

The XRT instrument consists of a small Wolter I mirror system of 12 nested mirrors with a focal length of 3.5 m. In the focal plane there is an EPIC MOS CCD similar to the ones aboard *XMM*. For non-GRB observations, it can be operated in two different modes: The Photon Counting (PC) mode or the Windowed Timing (WT) mode.

For most sources, the PC mode, offering a 2-dimensional image with a time resolution of 2.5 s can be used without any problems. For bright sources, however, count rates are high and it can happen that more than one photon at a time hits the same or a neighboring pixel (pile up). Patterns as shown in Fig. 2.3 (left) are produced on the CCD. These patterns, however, cannot be distinguished from cases where a single, high energy photon hits the detector near the border of a pixel, depositing a part of its energy in neighboring pixels. In order to minimize the distortion of the spectral form of the observed source, the possible patterns are graded and a threshold is set as to which events are kept and which are discarded due to their patterns not being unique. The standard selection for the PC mode defines grades 0–12 as acceptable and discards all other grades. For bright sources, this can lead to a significant loss of events.

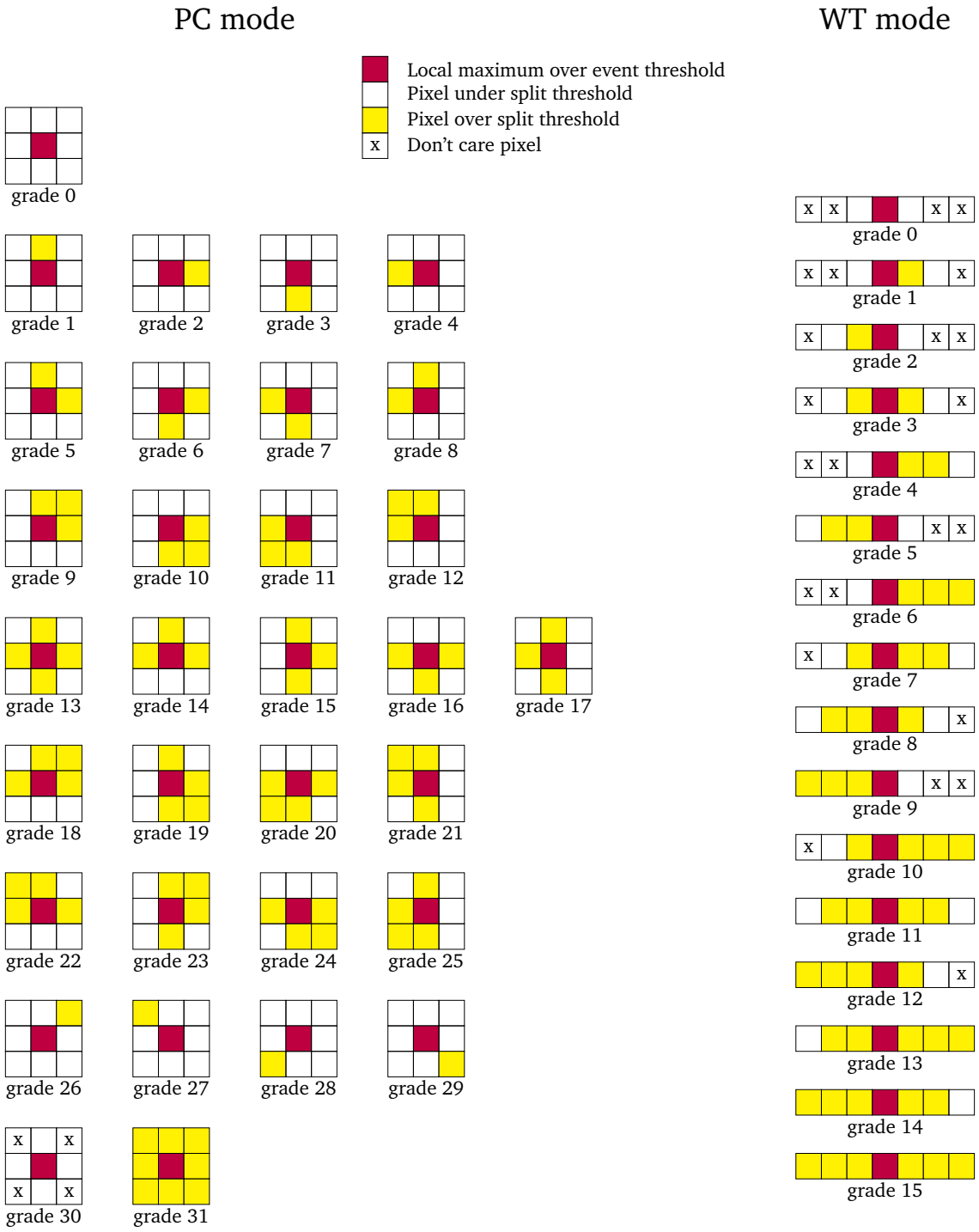

Figure 2.3: Grades for the XRT pixel in PC mode (left, after Capalbi et al., 2005, Fig. 2.2) and WT mode (right, after Capalbi et al., 2005, Fig. 2.3).

Similar to the *Chandra* modes, it is possible for the XRT to increase the timing resolution, thus minimizing the probability that two photons hit next each other during the same exposure, at the cost of one of the spatial dimensions: In the WT mode, only the central 200 columns of pixels are read out in continuous clocking. Thus, vertical information is lost and only a row of 200 pixels is left. To speed up the readout process, every ten rows are collapsed. This can lead to "split events", where a pixel pattern as described above falls between two subsequent 10-row-packages. The time resolution for this method, however, increases to 1.8 ms. Still, events are graded according to Fig. 2.3 (right) and a threshold is set: Only grades 0–2 are acceptable for the observation.

While the improvement of time resolution at the expense of a spatial dimension is a very easy method for observing single bright sources, Chapter 3 will show that it can lead to problems when observing in a crowded field on the sky.

3

There once was a star so immense
It became incredibly dense
  Then collapsed at great rate
  To a terrible fate
And has been a Black Hole ever since.

(Richard Newall)

Low- and intermediate-mass X-ray Binaries

Low mass X-ray binaries (LMXBs), as described in Sect. 1.2.1, are a class of predominantly transient sources. They spend most of their time in the quiescent state. Only if the accretion flow from their companion shows a sudden increase, they become visible in the X-rays in an outburst for some time before fading again into quiescence. It is possible to display such an outburst in a hardness-intensity diagram (HID), where spectral hardness on the X-axis is plotted against the respective source intensity (see Fig. 3.4, right). During an outburst, a LMXB shows a typical "q"-shaped track in this diagram.

This Chapter introduces the intermediate mass black hole binary GRS 1758−258 as an exciting example of a source that shows the basic LMXB properties but is still puzzling the observer with some unique traits, and discusses a variety of models that are proposed to explain the observed behavior of LMXBs during outburst in the HID.

3.1 GRS 1758−258

The persistent black hole binary GRS 1758−258 was discovered by the *Granat* satellite in 1990 during observations of the Galactic Center region (Mandrou, 1990; Syunyaev et al., 1991). It is located near the Galactic Center at a right ascension of $\alpha = 18^\circ\,01'\,12''.40$ and a declination of $\delta = -25^\circ\,44'\,36''.0$ (Heindl & Smith, 2002, see also Fig. 3.1). Nature and mass of the optical companion are still not confirmed. A K giant star filling its Roche lobe was suggested by Rothstein et al. (2002) in agreement with an orbital period of 18.45 ± 0.10 days as detected by Smith et al. (2002a). Recent spectroscopy by Martí et al. (2016), however, hints at the companion being an A-type main sequence star. This is in agreement with Muñoz-Arjonilla et al. (2010) and Luque-Escamilla et al. (2014), who suggest the system to be an intermediate mass X-ray binary. In addition, Hirsch et al. (2018) found the 18 day periodicity varying, which is pointing towards a warped accretion disk rather than the binary orbit to be the origin of the periodic signal.

At most times, GRS 1758−258 can be found in the hard state (Hirsch et al., 2018, and references therein). Apart from GRS 1758−258, there are only few other persistent black hole binaries in our Galaxy and the Magellanic Clouds: 1E 1740.7−2942 and Cyg X-1 predominantly in the hard state (e.g., Main et al., 1999) and 4U 1957+11 (e..g., Nowak et al., 2008)

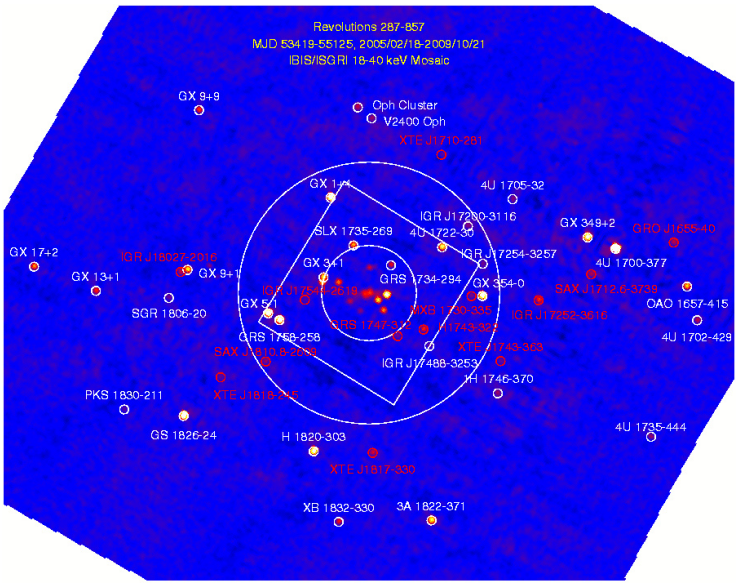

Figure 3.1: *INTEGRAL* IBIS/ISGRI 18–40 keV mosaic image of the Galactic Center region from the Galactic Bulge Monitoring Program (http://integral.esac.esa.int/BULGE/). The white square denotes the fully coded field of view of the IBIS instrument. GRS 1758−258 is the lower of the two bright spots in the left corner of this square, i.e., depending on the roll angle, not all bulge observations cover GRS 1758−258.

as well as LMC X-1 and LMC X-3 (e.g., Wilms et al., 2001) predominantly in the soft state. An overview paper of Tetarenko et al. (2016) place both the long-term accretion rate and the bolometric luminosity of GRS 1758−258 in the same category as bright transients like GX 339−4 or H1743. GRS 1758−258 is considered a microquasar as it shows a radio counterpart (a point source and a double-sided lobes, Rodriguez et al., 1992) with similarities to winged radio galaxies (Martí et al., 2017). An 11 years monitoring of GRS 1758−258 by *RXTE* (Bradt et al., 1993) revealed seven soft states between 1996 and 2007 (Hirsch et al., 2018, see also colored regions in Fig. 3.2). One can clearly see that during these soft states, the X-ray flux above 3 keV decreases significantly. (Soria et al., 2011) showed the total bolometric luminosity stays roughly constant during hard and soft states: GRS 1758−258 shows the typical brightening of the canonical high/soft state only in the very soft X-ray bands below 3 keV. This leads to a characteristic track in the HID (Pottschmidt et al., 2008; Hirsch et al., 2018) during a state transition, which shows a hysteresis curve but no rise from quiescence.

3.1.1 State transition models

There are several models that try to explain the evolution of X-ray binaries in the HID. This summary is taken verbatim from Hirsch et al. (2018):

"One of the first attempts to explain the hysteresis is the picture of two accretion flows set up and applied to GRS 1758−258 by Smith et al. (2002b): Based on Chakrabarti & Titarchuk (1995), they suggest a Keplerian accretion disk in combination with a hot, sub-Keplerian halo accreting proportional amounts of matter. A boost in accretion rate leads to the halo brightening at once (almost free fall timescale), whereas the brightening of the inner regions of the disk is delayed by the inspiral of matter (viscous timescale). Then the additional soft photons are cooling the halo and the spectrum softens. Similarly, a sudden drop in accretion rate would first affect the halo, its Comptonizing component declining rapidly. The Keplerian disk reacts only on the viscous timescale, causing the soft component to decay slower (Smith et al., 2002b, 2007), which is the "dynamical soft state" observed in GRS 1758−258

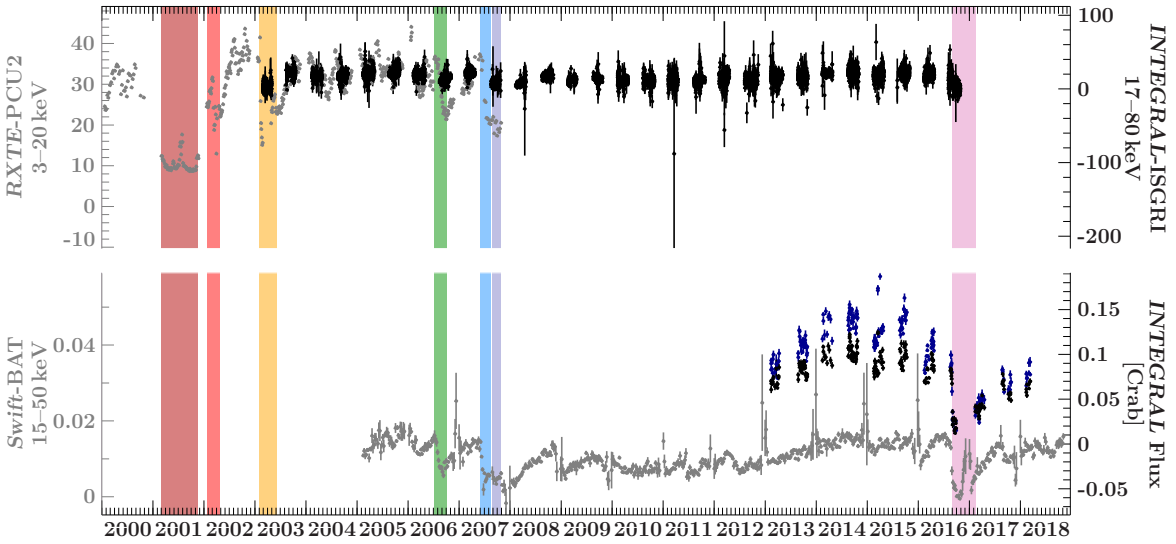

Figure 3.2: Light curve of GRS 1758−258 as seen in different instruments: *RXTE* PCU2 (top, grey), *INTEGRAL* ISGRI (top, black), *Swift* BAT (bottom, grey) and flux values in Crab for the recent *INTEGRAL* observations of GRS 1758−258 in the 20–40 keV band (bottom, black) as well as in the 40–80 keV band (bottom, blue). The *INTEGRAL* fluxes come from the *INTEGRAL* monitoring (see text for details).

and other black hole binaries, e.g., the transient source GX 339−4 (Debnath et al., 2015; Nagarkoti & Chakrabarti, 2016) and many other transients (Gierliński & Newton, 2006) as well as the persistent "twin source" of GRS 1758−258, 1E 1740.7−2942 (Smith et al., 2002b). Soria et al. (2011) refined this idea and suggest a magnetically powered coronal outflow as the source of the hard radiation. The accretion flow could then switch between the hard corona and the soft accretion disk because of changes in the poloidal magnetic field.

The interpretation of two accretion flows fits not only GRS 1758−258 but also other Galactic black hole binaries, With small changes, this picture can also be applied to high-mass X-ray binaries such as Cyg X-1 and LMC X-3 (Smith et al., 2002b, 2007): Here, the mass input is no longer distributed proportionally between disk and halo. State changes are induced by the accretion flow switching between favoring the disk while starving the halo and favoring the halo while starving the disk. Thus, the bolometric luminosity should remain almost unchanged during state transitions in these systems.

Meyer et al. (2000) and Meyer-Hofmeister et al. (2009) study the variability of an optically thin, advection-dominated accretion flow (ADAF), i.e., a hot corona, that is fed by evaporation of disk matter (see Fig. 3.3). For low accretion rates, the accretion rate equals the evaporation rate at the inner parts of the disk, and all matter is transferred to the corona, leading to a hard spectrum (Fig. 3.3, panel 4). If the mass flow increases, the truncated disk extends inwards and the spectrum softens (Fig. 3.3, panel 3) until, for very high accretion rates above the maximal evaporation rate, the disk is not truncated any more and the corona disappears (Fig. 3.3, panel 1). When the mass flow decreases and reaches a point below the maximal evaporation rate (Fig. 3.3, panel 2), the corona is built up again and a gap appears in the disk which widens with further decreasing inflow. An inner part of the disk may be sustained inside the hot corona by re-condensation of the ADAF. They state, though, that the dim soft states of GRS 1758−258 might require another mechanism (Meyer-Hofmeister

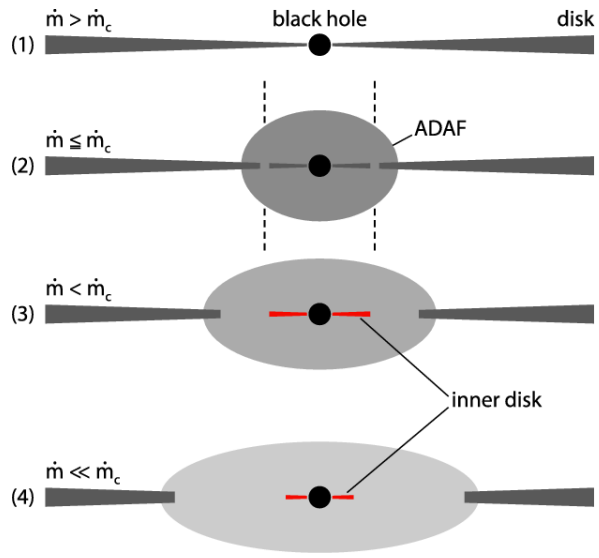

Figure 3.3: Accretion flow geometry depending on the mass accretion rate $\dot{m}$ relative to the critical accretion rate $\dot{m}_c$ for the transition (Meyer-Hofmeister et al., 2009). For a detailed description of the process, see text.

et al., 2009). Recently, Ghosh & Chakrabarti (2018) have found further evidence for an advective and a Keplerian flow analyzing time lags in the spectral slope for different HMXBs and LMXBs. They use a more extensive dataset and a completely different method than Smith et al. (2002b), yet their results lead to the same conclusion.

Other possible explanations for the driving mechanism of the state transitions have been brought forward since. Balbus & Henri (2008) suggested that different magnetic Prandtl numbers account for different X-ray states of black hole binaries: In their simulations, they find higher Prandtl numbers in the inner parts of the disk and lower Prandtl numbers in the outer parts. The critical radius with a Prandtl number of unity is dependent on the accretion rate. They speculate that if small Prandtl numbers correspond to the soft, thermal emission and large Prandtl number regions to lower density, hotter accretion, a change in the accretion rate and thus in the critical radius can easily lead to a change in the dominant disk region and explain a state transition. Further simulations are needed here as to the origin of the hysteresis.

A different proposition has been made by Petrucci et al. (2008) based on the model of Ferreira et al. (2006). From the luminosity differences between the hard-to-soft transition and the soft-to-hard transition, they conclude that changes in the accretion rate cannot be the only parameter to explain the hysteresis, and include a large-scale vertical magnetic field anchored in the accretion disk. Petrucci et al. assume a standard accretion disk (SAD) down to the usual observed disk inner radius. This radius is the transition radius to the inner, magnetized jet emitting disk (JED) with a hot thermal corona at the jet base. This inner disk is able to sustain a jet only for a small range of disk magnetizations: the magnetic field cannot be too strong as the vertical equilibrium has to be obtained via gas and radiation pressure support. On the other hand, it has to be strong enough for the plasma at the disk surface to be accelerated efficiently. This leads to a disk magnetization around $\mu \simeq 1$. Once the accretion rate increases, the total pressure increases and the disk magnetization decreases. This decrease propagates inwards through the SAD towards the transition radius. The JED adapts locally to the change in μ and the transition radius remains unchanged during propagation through the JED. If the accretion rate is such that the magnetization falls below a minimal value $\mu_{\min}$, the JED cannot be sustained, changes into a SAD outside-in, jet and

corona extensions shrink, and the source moves into a soft state. Eventually the transition radius equals the innermost stable circular orbit (ISCO), the JED has completely disappeared and with the large scale open magnetic field the MHD jet structure is probably oscillating between life and death, leading to large amplitude variations. Luminous systems may enter a flaring state with sporadic relativistic blobs being ejected. The JED cannot reappear until the magnetization has increased again significantly by the decrease in accretion rate and the subsequent decrease in total pressure. Only then, the original state can be re-established inside-out.

The model of Petrucci et al. (2008) yields potential to explain many exotic behaviors, e.g., the switching back and forth between the hard and soft state without a real hysteresis similar to Cyg X-1. This happens if the inner JED is never completely disappearing. For GRS 1915+105, which is accreting close to the Eddington limit, the JED competes with the SAD as the transition radius is at the ISCO, and the magnetic field continuously tries to re-adjust itself. This leads to a rapid variability in the order of fractions of seconds. Following up on this, Marcel et al. (2018b) extended this calculations to a two-temperature plasma. With a hybrid disk with an inner JED and an external SAD, the transition radius and mass accretion rate are the only parameters defining the spectral state (Marcel et al., 2018a).

Similarly, Begelman & Armitage (2014) propose a net magnetic field in the accretion disk to be the reason for the hysteretic cycle in black hole state transitions: During the quiescent state at luminosities much smaller than the Eddington luminosity, the black hole has a geometrically thick, hot accretion flow inside an outer thin disk. Vertical loops of magnetic field are generated at random places. If they are created in the inner hot flow, they are advected inward, whereas the ones created within the outer thin disk diffuse away, as a thin disk is not able to advect a vertical field inward (Lubow et al., 1994). A loop close to the interface between the two regions can have one footpoint that will be advected in the inner hot flow, and one that will escape in the outer thin disk. Eventually, this loop opens and an uncompensated net magnetic flux appears in both regions. For the thin disk with its small scale height, the accumulation of this net flux is too slow to be of interest. For the thick hot flow, however, the portions of net flux accumulate stochastically to a large net magnetic field. If now, due to variations in the accretion rate, the luminosity increases, and radiative cooling becomes too efficient to sustain the inner hot flow (Esin et al., 1997). After the transition of the thick region to a thin disk almost down to the ISCO, the magnetic flux will escape over time. The observed reversions of the inner disk to the hot state are due to fluctuations in the accretion rate. Only once the accretion rate has dropped significantly, the inner hot flow is re-established and the system returns to its initial state, starting again to accumulate a net magnetic field. This model, too, is able to explain various observed phenomena like QPOs, transient jets, and a large variety of possible outburst shapes. In this picture, GRS 1758−258 would need to have an accretion rate that is continuously high not to fall into the quiescent state but also low enough to be able to accumulate a net flux in the inner hot flow.

Another model has been proposed by Nixon & Salvesen (2014), who suggest that state transitions occur when the accretion disk is torn apart: If the spin of the central black hole is misaligned to the angular momentum of the geometrically thin, optically thick accretion disk (see Fig. 3.4, 1), an instability in this disk can lead to an accretion event. As the misaligned disk moves inwards (Fig. 3.4, 2), the hot, low-density material inside the outer disk gets compressed, the source gets brighter, and the Lense-Thirring-effect (Lense & Thirring, 1918)

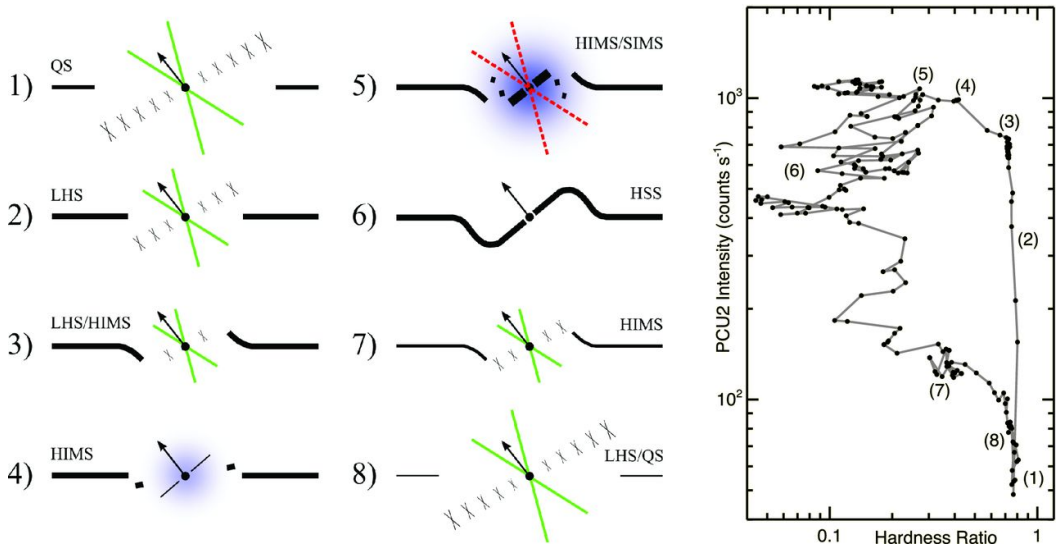

Figure 3.4: Sketch of the different stages of disk tearing (left) in a hysteresis cycle (right; Nixon & Salvesen, 2014, Fig. 1). The "X" demark regions with hot, low-density gas responsible for the hard X-ray continuum. If the black hole spin is misaligned to the accretion disk, the disk is torn apart for higher accretion rates, feeding a corona. More details can be found in the text.

causes the inner part of the disk to warp (Fig. 3.4, 3), until the first ring of gas is torn away (Fig. 3.4, 4). This ring now can precess independently. Interaction with the disk causes shocks and hot gas. The part of the gas cooling quickly falls inward, the part that stays hot fuels the corona. As more and more rings are torn successively, the cooling, infalling gas forms an inner accretion disk aligned with the black hole spin (Fig. 3.4, 5). This phase of tearing only ends once the strong deposition of misaligned material ends. Now the aligned inner disk is connected to the misaligned outer disk by the warp region (Fig. 3.4, 6), and accretion runs out of mass. The surface density drops, cooling becomes inefficient, and the system returns to the initial state (Fig. 3.4, 7 and 8).

This model is very flexible concerning the look of a predicted accretion event, which can look different not only from source to source but also from outburst to outburst in the same source. Small changes in the disk conditions lead to various possible behaviors. Nixon & Salvesen (2014) suggest that a negligible black hole spin or negligible misalignment of the angular momenta may lead to failed state transitions, or that tearing is entirely suppressed for high mass transfer in persistent sources. For GRS 1758−258, as it does not enter the quiescent state, the outer accretion disk in this picture would have to have a sufficient supply of material to constantly keep the hot, low-density region inside the outer disk compressed. Further investigations have to be made, however, to see whether this model is in agreement with the observed timing behavior of GRS 1758−258." (Hirsch et al., 2018).

3.2 The 2016 soft/off state

With its rare soft states differing somewhat from the majority of observed state transitions, GRS 1758−258 is a challenge for these models. *INTEGRAL* observed the source during the Galactic Centre Deep Exposure (GCDE, within its Galactic Bulge Monitoring observations

since 2005[1] (Kuulkers et al., 2007), and during the Galactic Centre Monitoring programme (PI Wilms[2]). As GRS 1758−258 only rarely transits into the soft state, gathering data on the transition itself is challenging. Since 2013, together with my collaborators, I successfully proposed for the GRS 1758−258 data rights in all observations where the source is within the field of view. When a sudden drop in the hard X-ray flux was observed in September 2016 by *Swift* as well as *INTEGRAL*, several Target of Opportunity (ToO) observations were done with *INTEGRAL* ISGRI[3] and *Swift* XRT (see Table 3.1).

The *INTEGRAL* IBIS data were extracted following the data analysis documentation[4], using OSA version 10.2. All *Swift* observations were extracted with the standard pipelines (Capalbi et al., 2005), using HEASoft V6.22.1 and XRTDAS v3.4.0. During the extraction process, various steps have to be made to obtain a final PHA (Pulse Height Analyzer) file with the data in it:

Photon counting mode Bad pixels according to the calibration data base (CALDB) are flagged as well as thresholded events and events from calibration sources. Hot and flickering pixels are calculated and flagged, too. Finally, events are assigned with a grade and put together into a PHA file. For the PC mode, I consider events with grades 0–12 acceptable.

Windowed timing mode Partially exposed pixels are removed and events are assigned with a time. Events are then reconstructed and graded, and bad columns are flagged. For the WT mode, I only consider grade 0 events acceptable, differing from the XRT software guide (Capalbi et al., 2005) which suggests to accept events with grades 0–2. This stricter approach reduces the number of split events[5]: If an event that would be classified as grade 1, 3 or 5–12 in PC mode is split up in the course of condensing every 10 rows for quicker readout in WT mode, two photons of lower energy are registered instead of one photon at higher energy.

Figure 3.5 shows the light curve during the transition into the soft state. The first *Swift* BAT ToO observation is quasi-simultaneous to the *INTEGRAL* ISGRI data collected by the monitoring program and the special ToO observation, shortly after the first massive decline of the source flux. From September 30, 2016, GRS 1758−258 has not been detectable for *INTEGRAL* ISGRI (Pottschmidt et al., 2016, see also Table 3.2 for the flux values). The *Swift* BAT data, too, show increasing error bars as the source flux drops towards non-detection. With three additional, dedicated ToO observations of ~ 2.5 ks during the deep soft state in late October and early November (see Table 3.1), however, *Swift* XRT was able to shed some light onto the soft X-ray spectra. For a comparison with the usual hard state of the source, I used a *Swift* observation of 2009 (ObsID 00030961004, see also Soria et al., 2011). Unfortunately, it was not possible to also observe a full HID cycle including the transition back to the hard state: Soon after GRS 1758−258 became invisible in the X-rays, the source region was hit by the annual sun constraints of both *INTEGRAL* and *Swift*.

[1] http://integral.esac.esa.int/BULGE/
[2] https://integral.esac.esa.int/isocweb/schedule.html?action=proposal&id=1520022
[3] https://integral.esac.esa.int/isocweb/schedule.html?action=proposal&id=1340018
[4] http://www.isdc.unige.ch/integral/osa/11.0/doc
[5] http://www.swift.ac.uk/analysis/xrt/digest_cal.php

Table 3.1: Overview of all used *Swift* observations.

ObsID	Date [yyyy-mm-dd]	Exposure [s]	Pointing Position RA [deg]	Dec [deg]	Roll Angle [deg]	Distance to GX 5−1 [deg]
00030961004[1]	2009-09-10	3316.549	270.232	-25.737	265.695	
00034729001[2]	2016-09-24	2681.228	270.262	-25.702	265.592	0.6236
00034729003[2]	2016-10-23	2355.911	270.300	-25.689	264.205	
00034729004[2]	2016-10-28	2648.209	270.259	-25.741	260.355	
00034729005[2]	2016-11-01	2524.100	270.273	-25.737	260.926	
00030961001[3]	2007-07-03	1356.024	270.218	-25.777	203.146	0.7011
00090044001[3]	2008-04-01	6867.536	270.358	-25.714	89.088	0.6380
00090044002[3]	2008-04-06	3313.899	270.324	-25.728	90.177	0.6500
00090044003[3]	2008-04-07	3438.762	270.317	-25.730	100.250	0.6515
00090044004[3]	2008-04-11	7399.443	270.309	-25.734	95.567	0.6553
00034310007[4]	2016-09-18	2577.927	299.571	35.199	301.965	

[1] Hard state observation and
[2] ToO observations of GRS 1758−258, all in windowed timing mode;
[3] Background observations near GRS 1758−258, in photon counting mode.
[4] Observation of Cyg X-1 to obtain the shape of the point spread function.

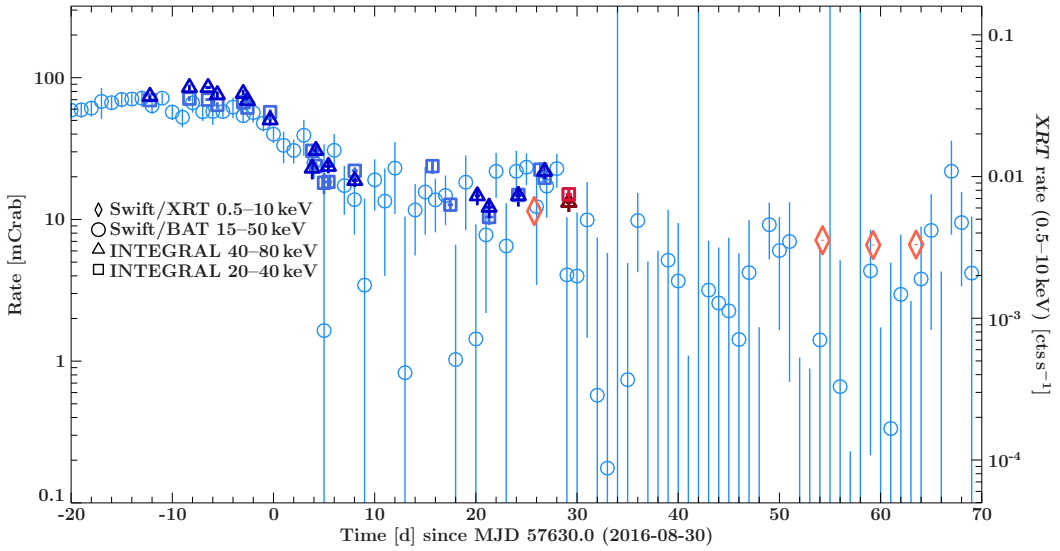

Figure 3.5: Light curve of the 2016 soft state. Blue circles are from the *Swift* BAT light curve. Blue triangles and squares are the *INTEGRAL* ISGRI datapoints from the monitoring campaign. Red triangle and square also contain the extra *INTEGRAL* ISGRI ToO observation on Sept. 30 (Revolution 1730). Red diamonds are from the accompanying *Swift* observation (on day 25) and three additional *Swift* ToO observations.

Table 3.2: Fluxes of GRS 1758−258 detected by *INTEGRAL* during the transition.

Date	20–40 keV		40–80 keV	
	Flux	Countrate	Flux	Countrate
[yyyy-mm-dd]	[mCrab]	[cps]	[mCrab]	[cps]
2016-08-17	69 ± 3	8.7 ± 0.3	74 ± 4	4.8 ± 0.3
2016-09-02	24 ± 2	3.0 ± 0.2	31 ± 2	2.0 ± 0.2
2016-09-27	15 ± 1	1.9 ± 0.2	13 ± 2	0.9 ± 0.1
2016-10-11		≤ 0.4		≤ 0.5

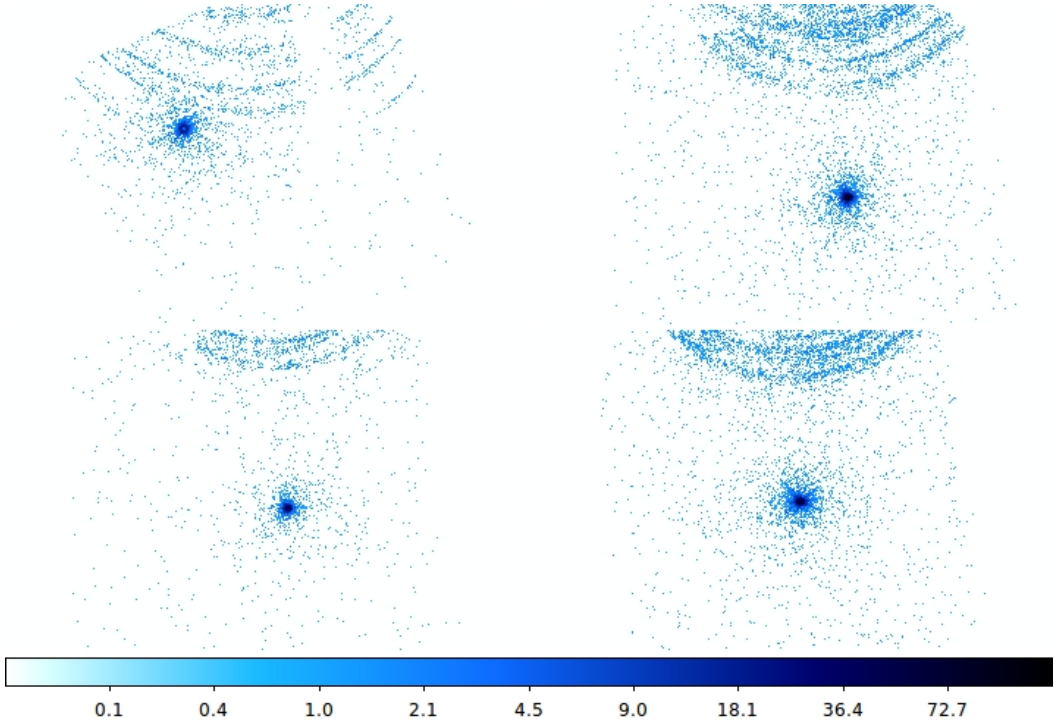

Figure 3.6: Straylight rings for four different *Swift* XRT PC mode observations of GRS 1758−258 (ObsIDs: Top left: 00030961001; top right: 00090044001; bottom left: 00090044002; bottom right: 00090044004); for details on the roll angle and angular distance of the line of sight to GX 5−1, see Table 3.1

3.2.1 Straylight background

As can be seen in Fig. 3.1, GRS 1758−258 is located very near to another bright persistent source, GX 5−1. This becomes a problem for observations of GRS 1758−258 in its dim state, especially when the *Swift* operates in WT mode (see Sect. 2.3.4), where a large part of events detected by the CCD are condensed into a single row: When off-axis photons enter the Wolter telescope at certain angles, it can happen that they are not reflected twice as intended for source photons, but they can pass on to the CCD after only a single reflection. They are thus scattered into the sky image despite of their source being located outside the field of view of the *Swift* XRT. On the CCD, they form a pattern of rings (see Fig. 3.6), whose diameter, width and position are dependent on the distance of the line of sight to the source of the stray photons, and the satellite's roll angle.

As the WT data collapses one direction of the CCD totally and reduces the resolution in the other direction, the stray photon counts get merged into the GRS 1758−258 data, leading to a contamination of the spectra by photons from a different source. As the ToO observations in 2016 were taken in WT mode only, it is not possible to estimate the background directly within the same observation as there is no sky image available. To estimate the impact of different roll angles on the amount of background counts in the source region of the WT mode observations, I rotated a PC mode sky image in steps of 10° and compressed the rotated image in the same way as the compression in the WT mode.

Figures 3.7 and 3.8 show a selection of angles for the WT observations 00030961001 and

00090044001, respectively. A stripe of ±100 pixels around the source position marked in colors denotes the region used in WT mode observations. For the WT mode data, this region is compressed onboard first by a vertical binning of 10 rows for faster readout, second by a sum over the resulting 60 rows for each of the 200 central columns. Thus, all vertical information is lost and what remains is a histogram of counts of 200 bins or columns. All data points outside the 200 central columns (grey in the figures) are lost. The histogram of the total columns is shown in the left panel in black for each angle. Due to the compression, the peak in the center of this histogram contains both the source counts coming from GRS 1758−258 as well as the straylight counts that fell into the respective columns. For the PC mode observations where two dimensional information is preserved, it is possible to estimate source and background counts by selecting a square around the source with the length of the edges equal to the diameter of the extraction region for the default WT mode extraction script. The events outside this box (shown in orange in the figures) are pure background counts. The events inside this box (shown in blue in the figures) are both source counts and – indistinguishable because they fell directly into the source region –some additional background counts. One can clearly see that despite the collapse of all columns into a single row, it is possible to estimate the amount of background counts in the source extraction region by taking the flanks of the histogram into account as well as to extract spectrum of the background contamination from these regions, also in the WT mode observations.

In the ObsID 00030961001 data (Fig. 3.7), it can be seen that, depending on the (simulated) roll angle, the source counts in the central region of the histogram are double-peaked. This is a typical pile up effect for a CCD detector: events are discarded if it is likely that more than one process can create the pattern they leave on the CCD. For a description of the event selection, see Sect. 2.3.4. If the *Swift* XRT countrate is high, as is the case for a point source like GRS 1758−258 in the center of the field of view, more events are discarded in the center than in the flanks of the point spread function[6] (PSF), leading to a double peak in the calculated histogram. The problem increases when the source image on the CCD is asymmetric by distorsion as in ObsID 00090044001 where for some roll angles as many as five peaks can be seen in the histogram. For further background analysis, I therefore use the ObsID 00030961001 data.

To confirm that pile up is the only factor affecting the peak, I compared the flanks of the peak to the measured PSF obtained from an observation without pile up of Cyg X-1 (ObsID 00034310007). This WT mode observation of the black hole binary Cyg X-1 has several good time intervals (GTIs). Fig. 3.9 shows the histogram of the GTI 5 WT mode data. This histogram can be taken as a model for the shape of the *Swift* XRT PSF. The flanks of the peaks in the GRS 1758−258 histograms therefore should have the same shape as this model PSF if the only influence on the GRS 1758−258 peaks is pile up, which only affects the center of the peak.

A fit of the flanks of the PSF obtained from the Cyg X-1 observation excluding the centers of the peaks (see Fig. 3.10) shows a very good agreement of the shapes of the flanks. The GRS 1758−258 peak can therefore be concluded to be double-peaked due to pile up, which, as can be seen for the single Cyg X-1 peak, is much less of a problem in WT mode observa-

[6]The point spread function is the response of a detector to a point source, which is, in most cases, radially symmetric for imaging on-axis point sources or a symmetric peak in a histogram for 2 dimensional observation like in the *Swift* XRT WT mode

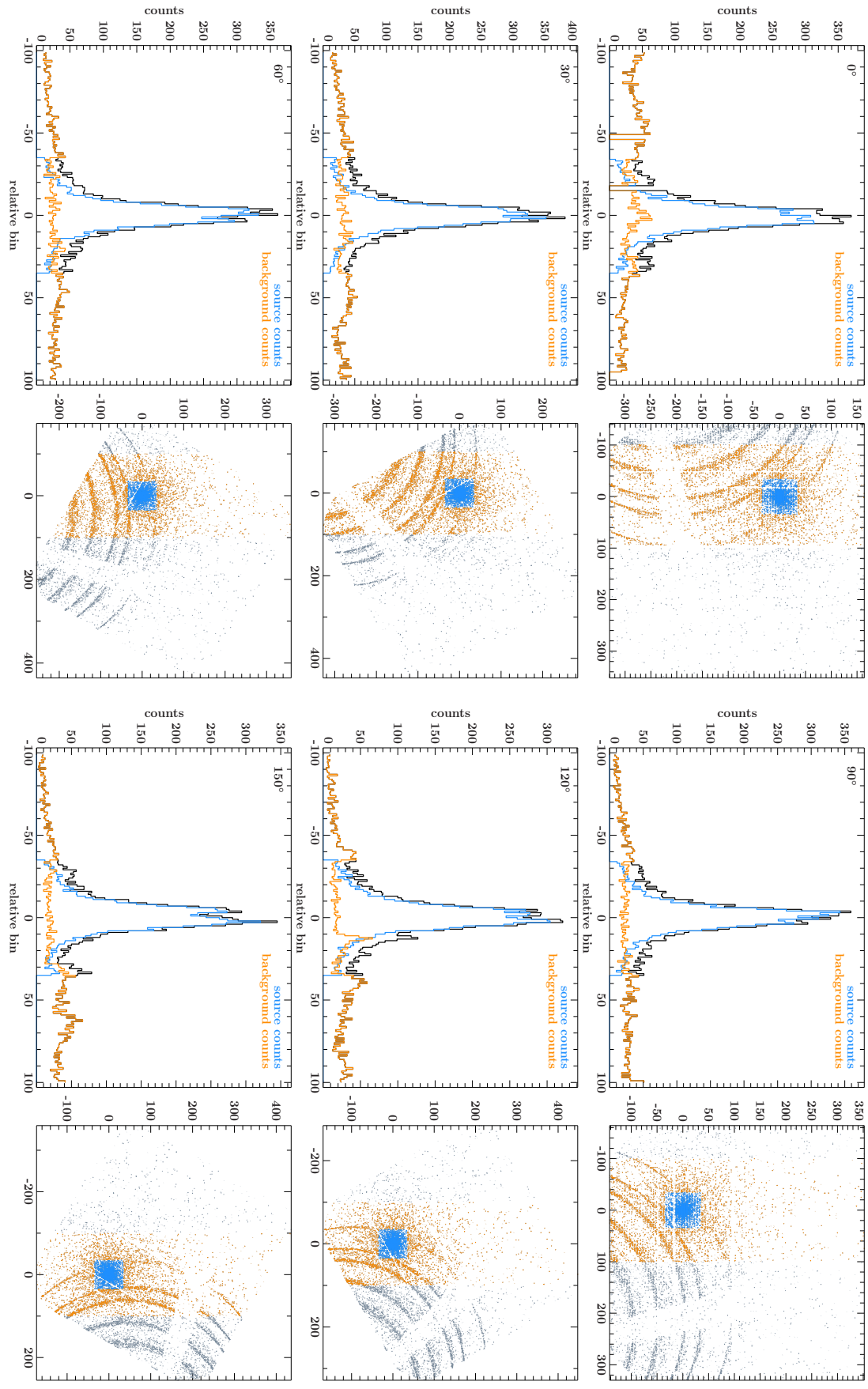

Figure 3.7: Influence of different (simulated) roll angles on the background rate in ObsID 00030961001. Right: Rotated PC mode observation image with the region of interest for the WT mode observations colored in blue (source counts) and orange (background counts). Left: Histogram of the colored regions collapsed onto the x-axis (Blue: Source counts; Orange: Background counts; Black: Total counts).

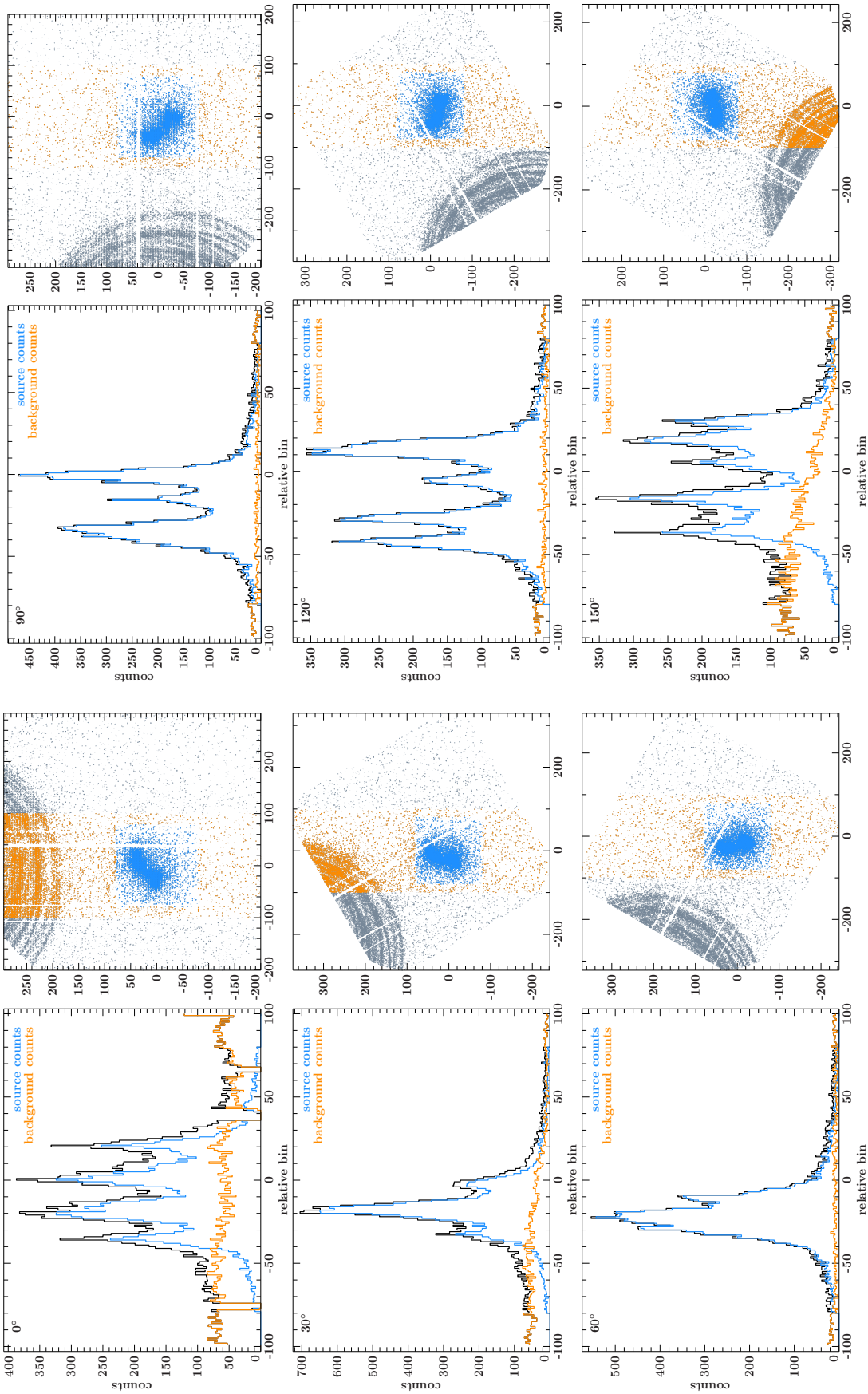

Figure 3.8: Influence of different (simulated) roll angles on the background rate in ObsID 00090044001. Right: Rotated PC mode observation image with the region of interest for the WT mode observations colored in blue (source counts) and orange (background counts). Left: Histogram of the colored regions collapsed onto the x-axis (Blue: Source counts; Orange: Background counts; Black: Total counts).

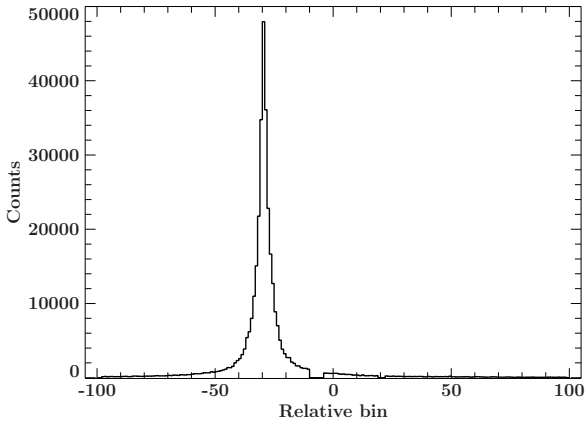

Figure 3.9: Histogram of the Cyg X-1 observation, ObsID 00034310007, GTI 5 data. The break to zero counts between bins -10 and 0 is due to a dead pixel column on the *Swift* XRT CCD.

tions.

The background of the WT mode GRS 1758−258 spectra thus can be described extrapolating from the counts to the left and right of the PSF peaks. I thus selected box regions containing the counts beside the peak for background calculation, and re-extracted the spectra using these boxes as a background region instead of the default annulus. Figure 3.11 shows the background-subtracted spectra for the four ToO observations as well as the hard state observation of 2009. The spectral differences between hard and soft state as well as between the early soft state and the deep soft state are obvious on first sight. Comparing the individual background spectra with the straylight spectrum extracted from ObsID 00030961001 shows that using a different observation at a different time would lead to a spectral distorsion as of course the straylight spectral form changes with the spectral form of its source.

3.2.2 Spectral modeling

The background-subtracted spectra were now rebinned to a minimum signal to noise ratio of $S/N \geq 7$ and modeled in the range of 1–10 keV with a simple absorbed[7] powerlaw. All soft state observations require an additional disk blackbody component (see Sect. 1.3),

$$\texttt{tbnew\_simple(1)} \times \big(\texttt{powerlaw(1)} + \texttt{diskpn(1)}\big).$$

The hard state observation does not show a black body but instead needs a narrow iron Kα emission line[8] at 6.30 ± 0.10 keV,

$$\texttt{tbnew\_simple(1)} \times \big(\texttt{powerlaw(1)} + \texttt{egauss(1)}\big).$$

Fit parameters are summarized in Table 3.3, Fig. 3.12 shows spectra, models and residuals as well as the absorbed and unabsorbed blackbody component for the soft state observations. The equivalent hydrogen column density due to interstellar absorption for all the fits is consistently higher than the $N_{\mathrm{H}} = 1.5 \times 10^{22}\,\mathrm{cm}^{-2}$ reported by Mereghetti et al. (1997). The blackbody disk temperature of ∼300–500 eV, however, are in agreement with the values found by Soria et al. (2011).

[7] `tbnew_simple(1)` uses the abundances of Wilms et al. (2000) and the cross-sections of Verner et al. (1996a) and is available online at http://pulsar.sternwarte.uni-erlangen.de/wilms/research/tbabs/. The `simple` version keeps all parameters fixed that are frozen by default in the original `tbnew` model.

[8] `egauss`, equivalent to the `gauss` line profile but computed on an energy grid

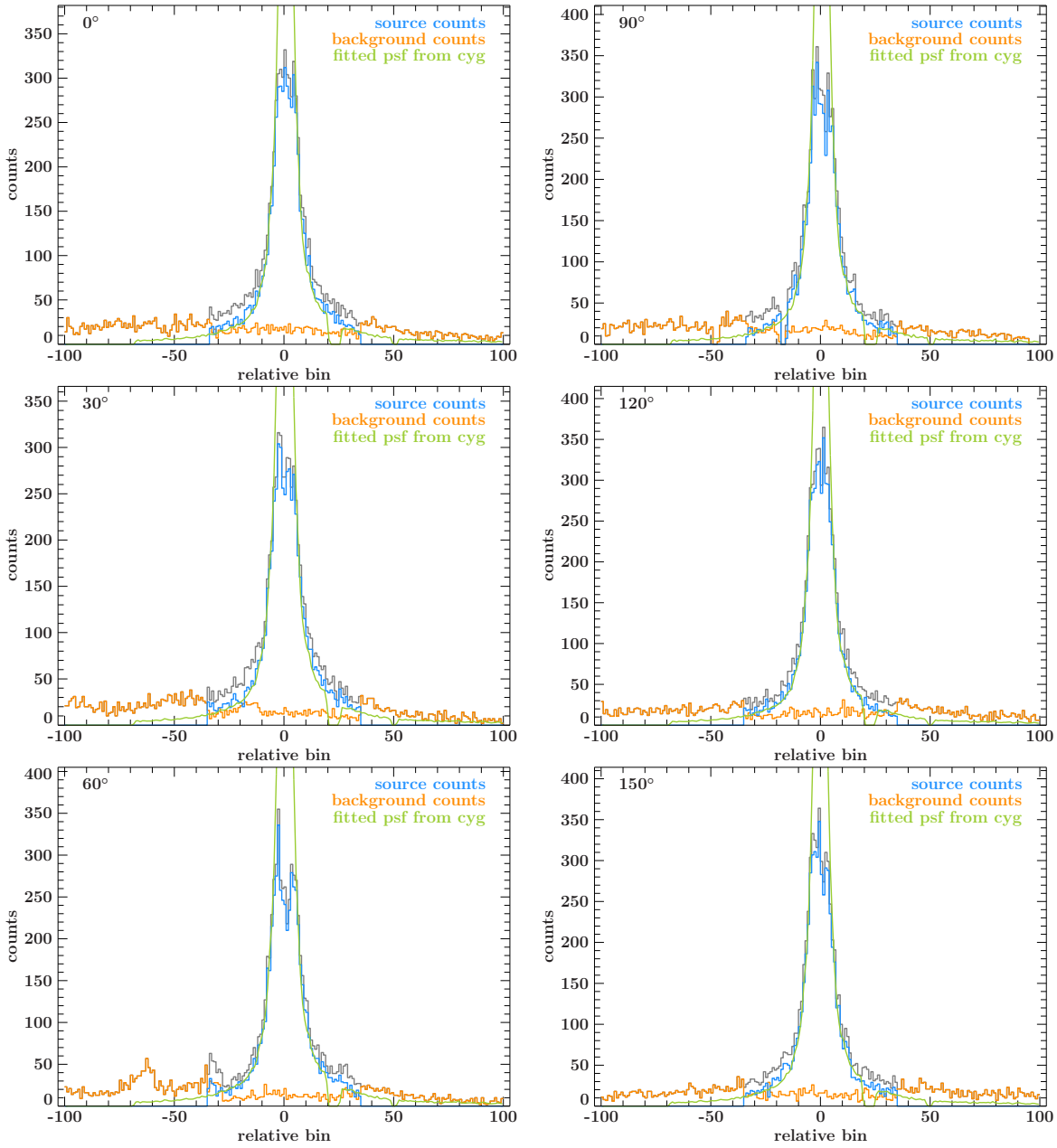

Figure 3.10: Fits of the PSF (green) obtained from the Cyg X-1 observation (ObsID 00034310007) to the flanks of the GRS 1758−258 peaks (ObsID 00030961001) for different (simulated) roll angles. For source (blue) and background (orange) regions, see Fig. 3.7

The photon index of the deep soft state powerlaw appears to be too low for a soft state. Omitting the blackbody disk, however, does not lead to an acceptable fit. Calculating error contours for the powerlaw photon indices and blackbody disk temperatures shows a clear anti-correlation between the two parameters as can be seen in Fig. 3.13.

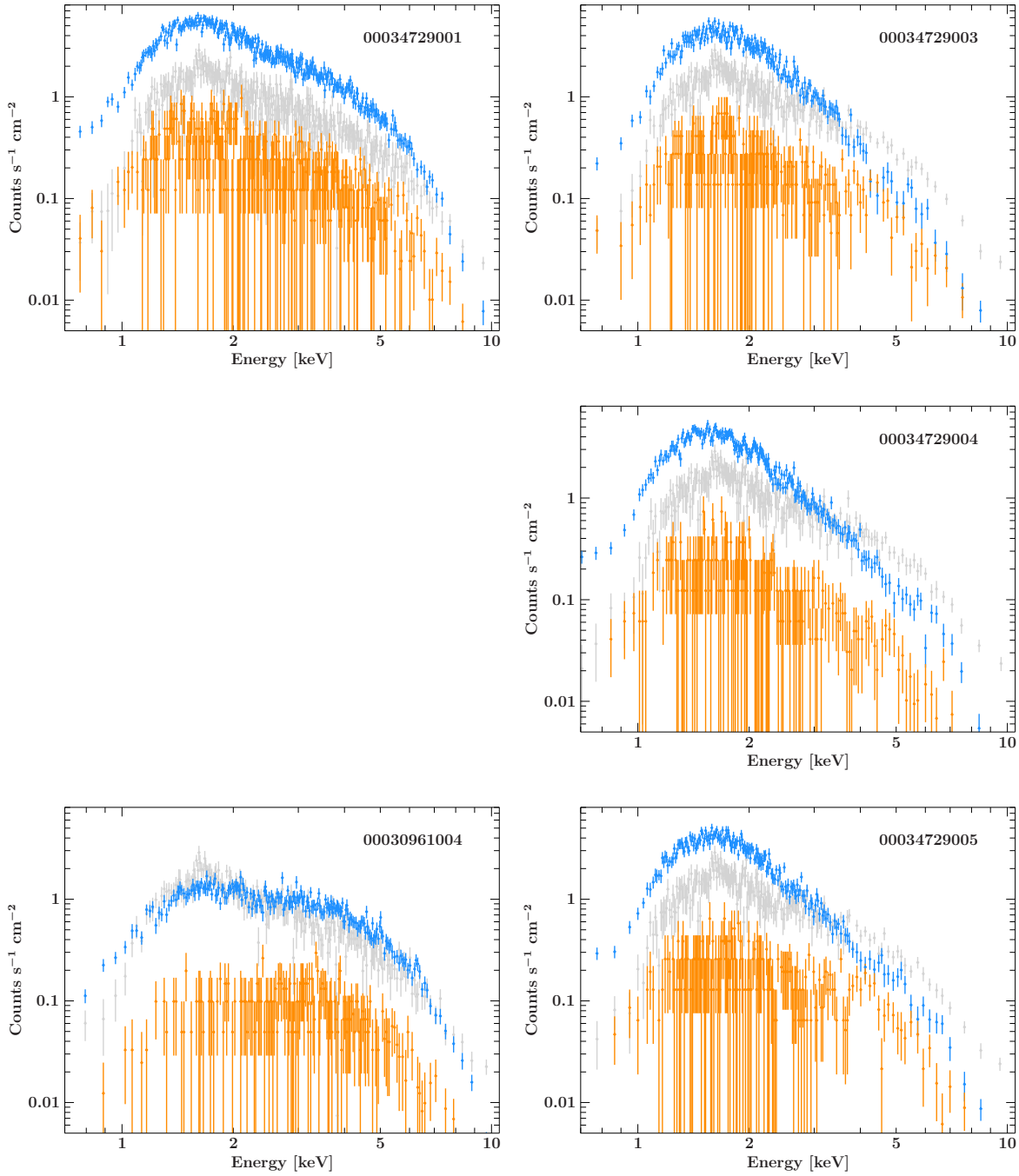

Figure 3.11: Background subtracted spectra (blue) binned to a minimal signal to noise ratio of $S/N \geq 7$ and background spectra (orange) for all ToO observations (top left for the joint *INTEGRAL* observation and right column for the three additional ToO observations) as well as the 2009 hard state spectrum (bottom left) for comparison. Shown in grey in all panels is the PC mode straylight observation (ObsID 00030961001).

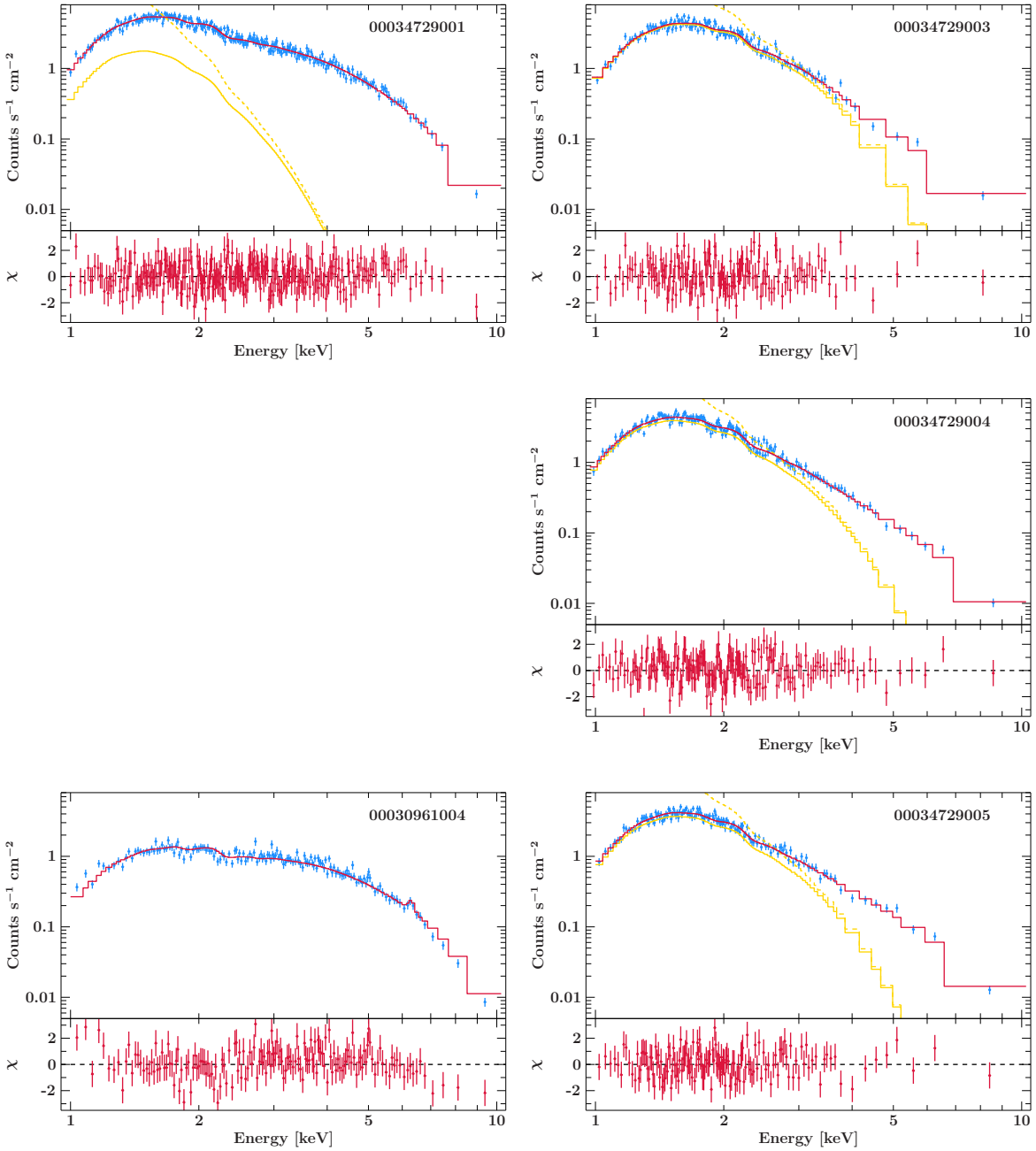

Figure 3.12: Spectra, model and residuals for all ToO observations (top left and right column) as well as the hard state observation (bottom left). Yellow lines denote the blackbody disk component absorbed by the ISM (solid yellow line) and unabsorbed (dashed yellow line).

Table 3.3: Fit parameters for all *Swift* observations.

ObsID	nH	powerlaw		diskpn	
		norm	Γ	norm	T_{max}
	$[10^{22}\,cm^{-2}]$				[keV]
00030961004	2.36 ± 0.15	$0.103^{+0.012}_{-0.010}$	1.53 ± 0.07		
00034729001	$2.73^{+0.33}_{-0.23}$	$0.37^{+0.08}_{-0.07}$	2.28 ± 0.13	$0.09^{+37.29}_{-0.07}$	$0.30^{+0.07}_{-0.06}$
00034729003	$2.59^{+0.15}_{-0.14}$	$\left(8.611^{+0.011}_{-7.312}\right) \times 10^{-3}$	$1.1^{+1.0}_{-1.1}$	$0.016^{+0.007}_{-0.005}$	$0.488^{+0.020}_{-0.031}$
00034729004	$2.27^{+0.15}_{-0.13}$	$0.028^{+0.043}_{-0.018}$	1.7 ± 0.6	$0.018^{+0.009}_{-0.006}$	0.45 ± 0.04
00034729005	$2.53^{+0.18}_{-0.16}$	$0.034^{+0.048}_{-0.021}$	1.7 ± 0.6	$0.023^{+0.014}_{-0.008}$	0.43 ± 0.04

ObsID	Fe line			χ^2_{red}	DoF
	norm	center	σ		
	$[photons\,s^{-1}\,cm^{-2}]$	[keV]	[keV]		
00030961004	$(5 \pm 4) \times 10^{-4}$	6.30 ± 0.10	$\left(6^{+5}_{-6}\right) \times 10^{-4}$	1.26	157
00034729001				0.90	257
00034729003				1.24	141
00034729004				0.99	169
00034729005				0.98	142

Empty cells imply that the respective model component was not required in the observation.

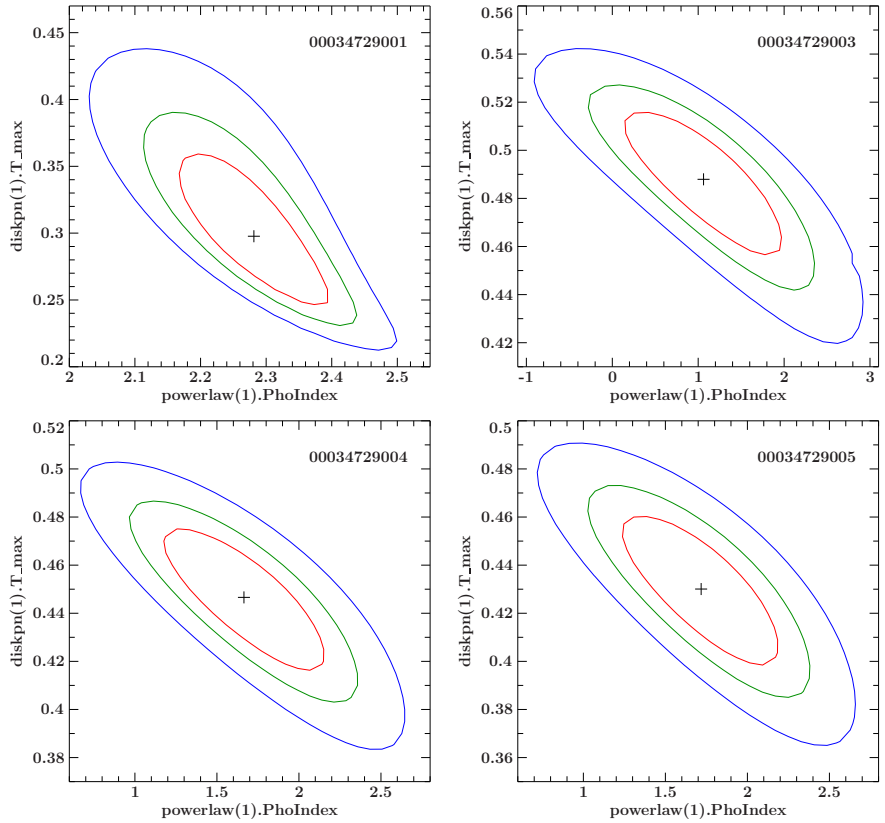

Figure 3.13: Error contours of the powerlaw photon index and the blackbody disk temperature. Red, green and blue lines denote the 1σ, 90% and 99% confidence limits, respectively. A clear anti-correlation is visible. A cross is positioned at the position of the best fit values.

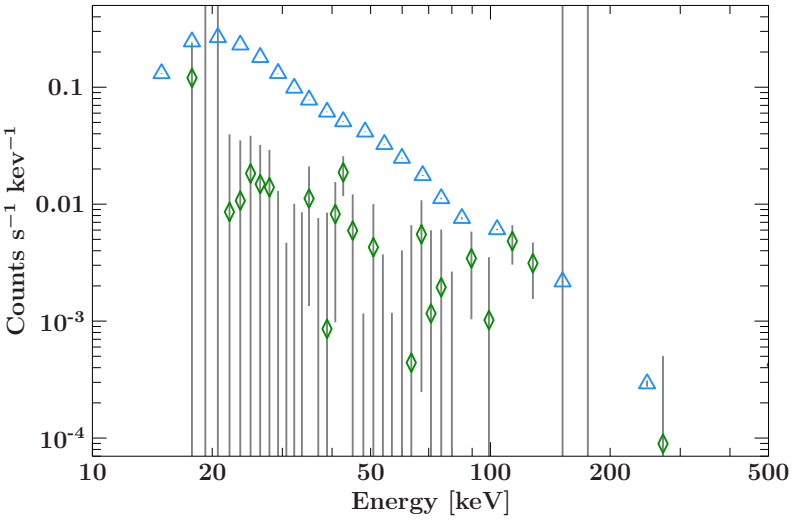

Figure 3.14: Comparison of the expected *INTEGRAL* spectrum (blue triangles, error bars within the plot symbols) simulated for a 168 ks observation and the actually observed spectrum (green diamonds) with a 230 ks total exposure.

3.2.3 *INTEGRAL* observation

Although the *Swift* spectra are mapping the low energy spectrum during the soft state very well, GRS 1758−258 was so dim in the hard X-rays that the *INTEGRAL* IBIS spectrum remained well below the expectations as can be seen in Fig. 3.14. Whereas the *Swift* snapshots showed a spectral variability of GRS 1758−258 even within the soft state, the *INTEGRAL* IBIS data are not sufficient for a fit even epoch-integrated over all available soft state data. It is therefore impossible to draw a conclusion on the broad band spectrum in the soft state from the data currently available.

3.2.4 Outlook

Of course, it is important to continue the monitoring of GRS 1758−258 and try again for a broad band spectrum during the next soft state. There are still open questions:

- What makes the HID of GRS 1758−258 look so special?
- Which state transition model is able to explain the dim, almost off soft states of GRS 1758−258?
- What observations are needed to confirm or discard these models?
- Do the dim soft states have an influence on the timing behavior of GRS 1758−258?
- If yes, are there models that are able to explain the connection?

Especially the latter two points could indeed be addressed in the next years: As a follow-up to the timing analysis of GRS 1758−258 presented in Hirsch et al. (2018), I calculated a dynamic power spectrum[9] (Fig. 3.15) of the *Swift* BAT light curve available from the BAT Transient Monitor[10] (Krimm et al., 2013) after the algorithm of Smith et al. (2002a). Similar to what was found in the *RXTE* PCA monitoring, the *Swift* BAT data also shows a drifting

[9] The evolution of the power spectral density (PSD) over the years using a window of fixed width and moving it over the light curve in steps. For each step, a periodogram is calculated and displayed as a line with the PSD color-coded. A detailed description can be found in Hirsch et al. (2018).

[10] https://swift.gsfc.nasa.gov/results/transients/GRS1758-258/

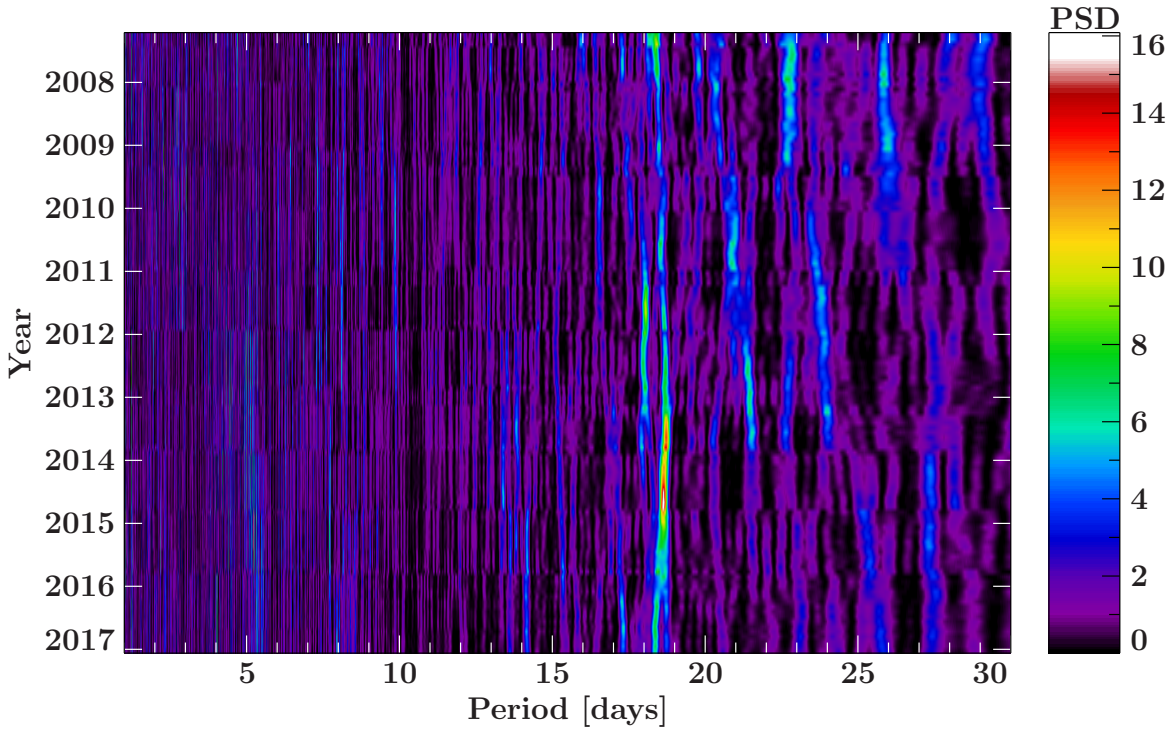

Figure 3.15: "Dynamic power spectrum of the 15–50 keV *Swift* BAT light curve, using the method of Smith et al. (2002a). The high energy light curve also shows a drifting peak. A change in period is obvious in 2016, near the most recent soft state."(Hirsch et al., 2018, , Fig. 13)

periodicity between 18 and 19 days. "The signal is not as strong as in the PCA data, but the behavior is clearly the same in high as in low energies. Note that around the most recent, very dim 2016 soft state (Pottschmidt et al., 2016; Hirsch et al., 2016, Hirsch et al., in prep.) a decrease in period is visible similar to the decrease in the PCA dynamic power spectrum around the very dim 2001 soft state. This additional observation of the drifting periodicity with another satellite than *RXTE*, at another time, in another energy range, further increases the confidence that we are seeing a source-intrinsic signal." (Hirsch et al., 2018). The origin of this signal, however, is yet unclear, and two occurrences of a change in the periodic signal during a dim soft state do not provide much statistics. Further monitoring and simultaneous observations of the next soft state in both hard and soft X-rays is therefore the only possibility to tackle these questions.

4

A computer, to print out a fact
will divide, multiply and subtract.
   But this output can be
   no more than debris
if the input was short of exact.

(Dave Gorski)

Super Soft Sources

Super soft sources have been observed since the very beginnings of X-ray astronomy. First observations with the *Einstein* satellite (Giacconi et al., 1979) in 1981 revealed unusually soft spectra (Long et al., 1981; Seward & Mitchell, 1981). The better resolution and more suitable energy range of *ROSAT* (Trümper, 1982) showed that unlike both black hole binaries and stellar coronae, super soft sources do not show any hard emission but actually peak below the sensible range of *ROSAT* of $\sim$ 0.2–2.5 keV. This chapter introduces the class of objects, focusing on their timing behavior and whether one can draw conclusions from this to how the emission region of the super soft X-rays looks like. The correct estimation of uncertainties is an essential part of this analysis in order to get reliable results.

Super soft sources are difficult to detect as their soft emission is strongly affected by interstellar absorption. The luminosity and effective temperature of the black body emission therefore cannot be measured without information on the column density in the direction and to the distance of the object. An early review of the sources is presented by Kahabka & van den Heuvel (1997). From luminosity and temperature measurements of typical super soft sources, they derive the radius of the emitting object to $\sim$9000 km, which is in the range of white dwarfs. Thus, they suggest accreting white dwarfs as a basic concept for this type of sources.

Depending on the mass accretion rate and the mass of the white dwarf itself, it is possible that the accreted matter starts burning on the surface of the white dwarf: Unlike the much more massive neutron stars and black holes, a white dwarf does not provide enough gravitational potential for accretion to be the most efficient way to release energy (Kahabka & van den Heuvel, 1997): A typical accreting black hole releases about 20 times more energy by accretion of a test mass of hydrogen than what would be released by fusion of the same amount of hydrogen. The fusion process therefore is negligible in those cases. For white dwarfs, on the other hand, fusion is about 30 times more efficient in releasing energy than accretion.

Figure 4.1 (see also Kahabka & van den Heuvel, 1997, and references therein) shows that for a certain range of accretion rates, steady hydrogen burning is possible on the surface of the white dwarf, depending on its mass. If the accretion rate remains below this range, the white dwarf will collect matter until there is a shell providing sufficient pressure and temperature to start burning in a flash that lasts until there is no hydrogen left. The flash subsides and collecting matter starts anew. For very high accretion rates, on the other hand, the radius of the shell of matter expands to large dimensions: A low mass red giant is created (e.g., Kippenhahn et al., 2012; Newsham et al., 2014, and references therein). Burning takes

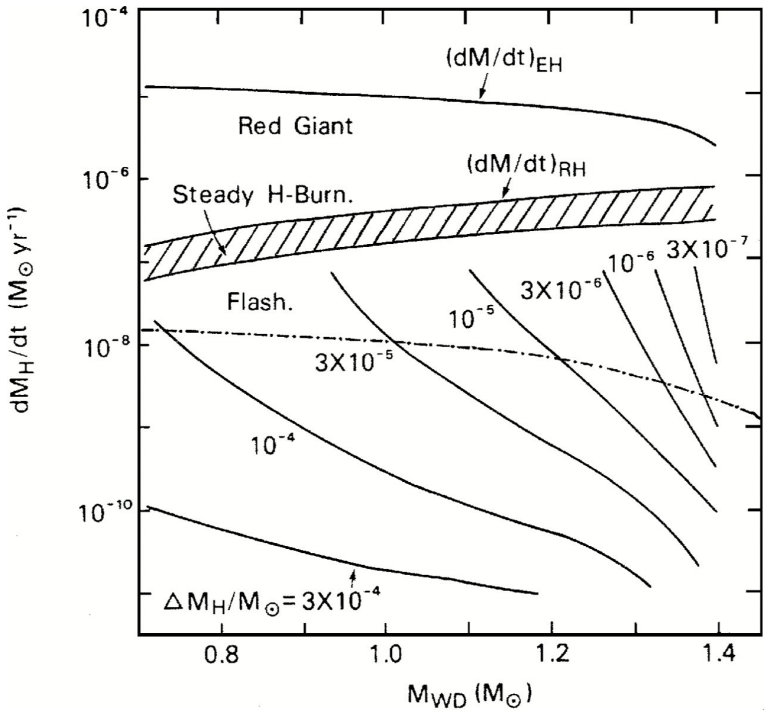

Figure 4.1: States of WD nuclear burning depending on WD mass and accretion rates (dashed region); Steady burning is possible only for a narrow range of accretion rates. Lower accretion rates result in flashing whereas for higher rates, the WD expands to the dimensions of a red giant (Kahabka & van den Heuvel, 1997, Fig. 5).

place steadily in a thin shell around the white dwarf "core". There are calculations (Hachisu et al., 1996), however, that show the onset of a strong, optically thick wind for high accretion rates. That wind would then be opaque to soft X-rays, effectively hiding those sources from view (e.g., Wheeler & Pooley, 2013). High spectral resolution X-ray observations revealed that the emission from super soft sources indeed is not a blackbody but can be represented by atmospheric models with absorption lines and edges (e.g., Lanz et al., 2005), confirming the theory of an accreting white dwarf.

There are persistent super soft sources that accrete at a rate of $4–10\times10^{-7}M_\odot$ where steady burning is possible. The most simple binary to provide this mass flow is a near main sequence (slightly evolved) companion earlier than F5 (Kahabka & van den Heuvel, 1997). Such a companion is more massive than the white dwarf and has a large radius, thus overflowing its Roche lobe (see Chapter 3 for more details). To this class of close binary super soft sources belong, e.g., Cal 83 and Cal 87 (Greiner et al., 1991; Long et al., 1981; Smale et al., 1988; Pakull et al., 1988; Schmidtke et al., 1993; Kahabka et al., 1994). Another possibility is a symbiotic system consisting of a white dwarf with a less massive red giant companion. Depending on the orbit, it is either possible for the red giant to overflow its Roche lobe or, if the red giant is on the Asymptotic Giant Branch (AGB), it can emit a very strong stellar wind for the white dwarf to accrete (Kahabka & van den Heuvel, 1997).

In addition, a third class of super soft sources has been observed: A small number of novae show the characteristics of super soft sources for some years after their nova outburst. This can be the case if some of the accreted matter is left over after the ejection process. Figure 4.2 (see also Hachisu & Kato, 2006a) summarizes such a nova explosion, which is caused by thermonuclear runaway on the white dwarf. In the course of the outburst, the envelope of the white dwarf expands enormously, with large parts of it ejected in a strong, optically thick wind. This wind on the one hand blocks the soft X-ray emission from the white dwarf

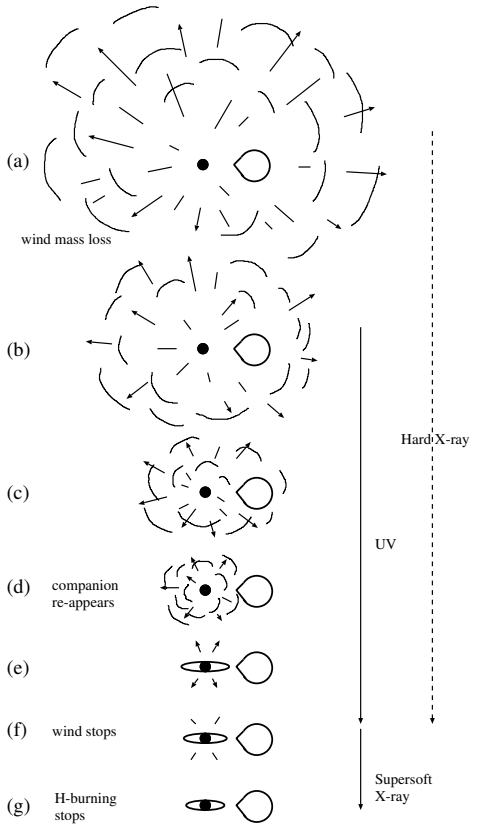

Figure 4.2: Evolution of a nova outburst: (a) the explosion causes an expansion of the photosphere to very large radii, embedding the companion star; hard X-rays are produced during the wind phase in shocks; (b) while the photospheric radius is shrinking again, the spectrum is dominated by free-free emission; the photospheric temperature increases, ultraviolet radiation dominates the spectrum; (c) more and more material is blown away, causing further shrinking until (d) the companion star emerges again from its envelope; (e) the photosphere shrinks further and an accretion disk around the white dwarf appears; (f) the wind stops, dominating emission is now in the supersoft X-ray regime; as most of the hydrogen has been lost during the explosion, (g) hydrogen burning cannot be sustained any more. A cooling phase starts. (Hachisu & Kato, 2006a, Fig. 1)

photosphere within, and on the other hand cools down the photosphere to temperatures that are not high enough for an emission of soft X-rays. The X-ray onset is therefore supposed to happen with the wind subsiding (Hachisu & Kato, 2006a). There are observations, however, that uncover an earlier onset of the soft X-ray emission in the recurrent nova RS Oph (Bode et al., 2006; Hachisu & Kato, 2006b; Osborne et al., 2006a,c). An interaction region with shocks between the fast wind of the white dwarf envelope with the slow wind of the red giant companion could be an explanation for the emission pattern (Vaytet et al., 2007). From simulations, they find an outburst mass ejection of a few times $10^{-7}\,M_\odot$ and an unexpectedly high velocity of $10000\,km\,s^{-1}$ (Vaytet et al., 2011). They find that single temperature emission models, even if several single temperature components are considered, as well as line width measurements, do not reproduce the high temperatures and thus underestimate the shock velocities. More complicated 2D simulations need to be done to investigate the effect of a bipolar outflow on the velocity and temperature distributions (Vaytet et al., 2011).

Whereas the types of companion stars possible for a super soft source can be well constrained by the observed luminosity, temperature, and necessary accretion rate to produce the observed super soft X-ray emission, the details of the white dwarfs themselves as well as of what exactly happens in the burning region are much more difficult to uncover.

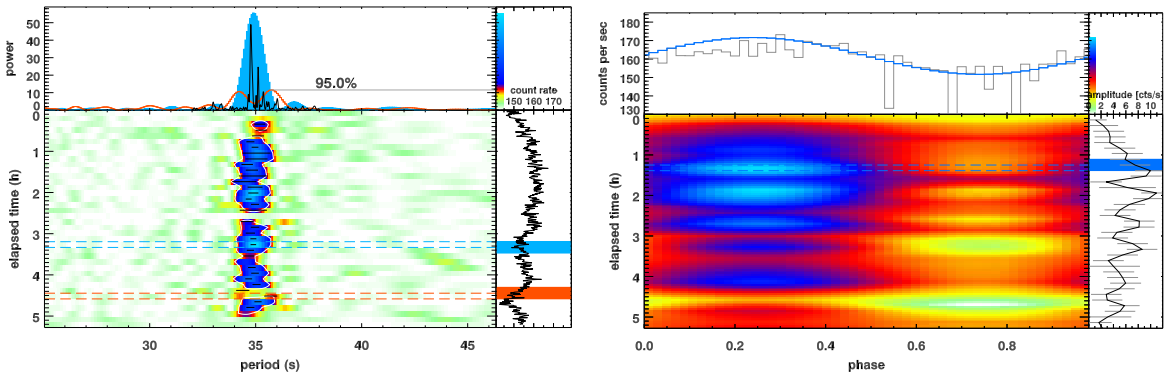

Figure 4.3: RS Oph on day 54 after the nova outburst (Ness et al., 2015, Fig. 2). **Left:** Dynamic power spectrum of the *XMM* RGS2 light curve. Color-coded in the main panel is the power spectral density (PSD). A power spectrum for selected light curve windows are represented at the top (color-coded), together with the PSD of the full light curve in black. The right panel shows the count rate light curve. **Right:** Evolution of the folded light curve, each line synchronized that the maximum occurs at phase 0.25. The top panel shows an example of the light curve together with a sine fit, whereas the right panel tracks the evolution of amplitudes throughout the light curve.

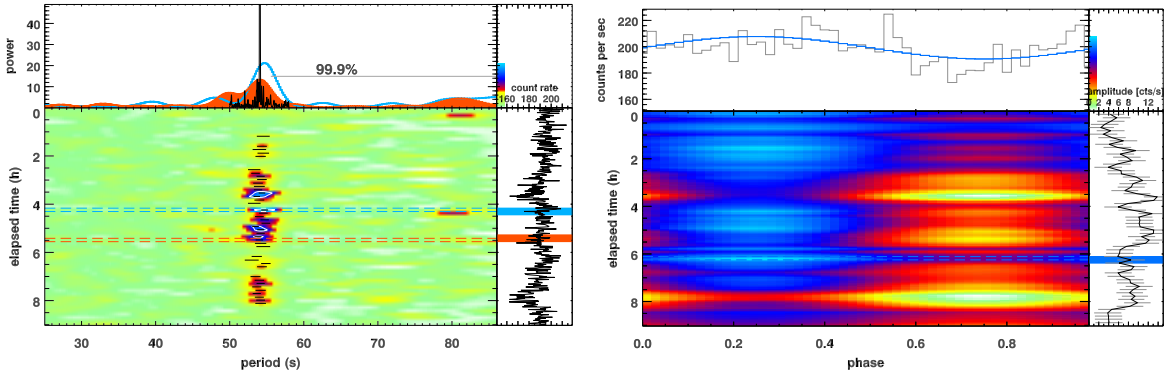

Figure 4.4: V339 Del on day 99 after the nova outburst (Ness et al., 2015, Fig. 6). For a description of the panels, see Fig. 4.3.

4.1 Short period oscillations

It has been first observed in the recurrent nova RS Oph in 2006 that a super soft source shows a transient signal of short period (about 35 s) oscillations during its super soft state (Osborne et al., 2006b, 2011). This signal was confirmed by Ness et al. (2007), who found its origin in the soft X-rays, but not in the hard X-rays coming from the shock emission, as well as by Nelson et al. (2008). Other sources, too, were shown to have a transient periodicity, e.g., KT Eri (35 s, Beardmore et al., 2010) or V339 Del (54 s, Beardmore et al., 2013; Ness et al., 2013). The persistent super soft source Cal 83 also has a transient periodicity of about 67 s, which was suggested to be driven by the rotation period of the white dwarf (Odendaal et al., 2014). Although it seems obvious that the oscillation has its origin on the surface of the white dwarf, where nuclear burning takes place during the time the super soft emission is seen, there are not enough sources observed to draw a conclusion on the process producing these oscillations.

To add to this statistic, Ness et al. (2015) searched for transient oscillations in 18 sources that show super soft emission (see their Table 1). The remainder of this section is based on this paper. My contributions to this work are highlighted in Sect. 4.2. Ness et al. (2015) used light curves with a time resolution of 1 s for sources observed with the *XMM* EPIC and RGS detectors as well as for *Chandra* HRC data and a resolution of 2 s for *Chandra* ACIS data. To focus on the short period oscillations, the light curves were detrended, i.e., the long term variations were either fitted by a higher order polynomial or a Gaussian kernel smoother was applied. The thus generated long term variation light curve was then subtracted from the original data so only the high frequency residuals are left. To find the transient signals in the long light curves, dynamic power spectra were calculated, applying the method of Horne & Baliunas (1986) to overlapping windows of 1000 s each, moving over the light curve in steps of 500 s. For each of these windows, they tested 500 frequencies in the range of 25–100 s. A close-up to the 35 s signal detected in RS Oph as well as the 54 s signal in V339 Del as they evolve in the respective observations can be seen in Fig. 4.3 and Fig. 4.4, respectively. For further details, see Ness et al. (2015).

4.2 Calculating Significances

It is important to correctly consider the significance of a periodicity detected in the process described above. Only for a significant signal, one can speak of a detection and think about implications of this detection. Ness et al. (2015) chose two different ways of calculating an uncertainty of the pulse periods. The first method uses the standard deviation of count rates and the amplitude of a sinusoid fitted to the folded light curve after Larsson (1996, Eq. 4) (see also Scargle, 1982; Horne & Baliunas, 1986). Similar to the analysis in Hirsch et al. (2018), for the second approach I obtained "the standard deviation of pulse periods obtained from Monte Carlo simulated light curves. These lightcurves were obtained by replicating the folded light curve using the same sampling as the original light curve and adding the appropriate Poisson noise. We then calculated the standard deviation of the periods measured from 10000 of such realizations and assign this number as the uncertainty of the period. In general, both approaches yield comparable results" (Ness et al., 2015, p. 5).

Though they are time-consuming to compute, Monte Carlo simulations are the method of choice for a calculation of uncertainties in many cases. They allow the investigation of the following parameters:

The false alarm probability and thus the detection threshold can be estimated by generating synthetic light curves containing only Poisson noise, i.e., random values distributed after

$$P(k,\mu) = \frac{\mu^k}{k!} e^{-\mu} \tag{4.1}$$

around a given mean count rate and analyze them the same way as the original light curves. In this case 10 000 synthetic light curves with a duration of 1000 s were tested for 500 frequencies between 25 s and 100 s. The distribution of PSD values of the highest peak in these PSDs gives a measure of the probability to detect a spurious signal: If a PSD calculated from the observed light curve shows a peak of a certain power in the PSD, the fraction of simulated light curves that show a peak of this power

or more in the PSD gives a measure of the probability that the peak in the original data is not source-intrinsic but a spurious peak.

Systematic errors by sampling If a periodicity that is observed in a light curve is not source-intrinsic but induced by e.g., a beat in the sampling of the light curve, a simulated light curve with the original time stamps but purely Poisson distributed count rates, i.e., a light curve containing no periodic signal would also show the periodicity in the PSD.

Systematic errors by smoothing and the selection of the time windows Equivalently, influences of the smoothing algorithm can be tested using simulated light curves with noise only or with a known sinusoid signal. Variations of the selected time window using a synthetic light curve with a known periodicity can exhibit effects of the chosen window length.

In addition, effects of oversampling, i.e., testing more than just the normal Fourier frequencies to increase sensitivity, as well as implications by multiple testing due to the overlapping time segments, have to be taken into account. The former is accomplished using Monte Carlo simulations with different oversampling factors. The latter is corrected for using the conservative method of Bonferroni (1936). For further details, see Ness et al. (2015).

4.3 Possible driving mechanisms

Out of the 18 sources, the light curves of which Ness et al. (2015) analyzed, four novae and one persistent super soft source with a periodic signal were detected to show periodic behavior with a significance larger than 95 %. The transient super soft sources RS Oph (34.9 ± 0.2 s), KT Eri (35.0 ± 0.1 s), V339 Del (54.1 ± 0.3 s), and LMC 2009a (33.2 ± 0.1 s) all show a transient periodic oscillation. The 66.8 ± 0.5 s signal of the persistent source Cal 83, already observed by Odendaal et al. (2014), is of a transient nature, too (see Ness et al., 2015, Table 2 for more details). Unfortunately, this sample still does not provide much statistics. However, a trend can be seen that the longer periods tend to occur for slower novae, i.e., for lower white dwarf masses (Livio, 1992). So what can be learned from this sample?

Thomson scattering has been shown to be a strong effect in super soft sources (Ness et al., 2012). Thomson scattering is the low energy limit of Compton scattering, where no transfer of momentum takes place between a scattering photon and an electron. As long as the photon energies remain within the Thomson regime, the scattering process is not energy dependent. Chang & Kylafis (1983) investigated the effect of Thomson scattering on the amplitude of oscillations. Based on their calculations, Ness et al. (2015) estimate that the density in the scattering region would have to be very high to have a significant effect on the amplitudes of the modulation. The detectability of an oscillation is therefore not reduced by Thomson scattering.

The rotation period of the white dwarf has been proposed as the driver for the persistent 67 s period in Cal 83 (Odendaal et al., 2014). Although the white dwarf could be sufficiently spun up to reach such a short rotation period, the changes in period observed by Ness et al. (2015) cannot be explained to be induced by accretion only.

A beat between the rotation period of the white dwarf and the plasma surrounding it would require even higher rotation velocities for the white dwarf. If the cause of the modulation is within an extended envelope of gas rotating asynchronous around the white dwarf, the spread in period could be explained (Odendaal et al., 2014), though the exact origin of the modulation as well as quantitative results remain unclear. The transient super soft sources with their even shorter periodicities challenge this picture. If the rotation periods of those white dwarfs were known, it might be possible to further argue into this direction (Ness et al., 2015).

Pulsation modes on the surface of the white dwarf are a promising model to explain the observed oscillations. A contraction or heating leads to an increase in the nuclear burning rate and again to more pressure or heat, causing an expansion. The expansion cools down the burning region, leading to reduced burning and further cooling, until the pressure cannot compensate the gravitational force any more, leading again to a contraction, and the cycle starts anew. This process is called ϵ-mechanism and has been considered for modulations in the white dwarf in planetary nebulae (Kawaler, 1988) as well as in neutron stars that are burning their accreted mass similar to the super soft sources (Piro & Bildsten, 2004). Calculations of Ness et al. (2015), however, show that for the lowest order modes caused by this mechanism, the observed periods are too short. They can be explained if the higher order modes are excited, although the reason for this excitation requires more detailed theoretical research (Ness et al., 2015; Wolf et al., 2018).

If indeed the pulsation modes are the reason for the observed oscillations, this might constrain the mass of the white dwarfs in super soft sources as opposed to other white dwarfs. If the accretion in the super soft sources causes the white dwarfs to grow in mass, it might be worthwhile to consider such systems as progenitors for type Ia supernovae.

More recently, Odendaal & Meintjes (2017) presented an alternative explanation for the modulation in the persistent super soft source Cal 83: They extend the low-inertia magnetic accretor (LIMA) model (Warner & Woudt, 2002) to the more extreme environments of super soft sources (eLIMA). LIMA has first been proposed as a model to explain dwarf nova oscillations. If the white dwarf has a weak magnetic field, it is possible to use this field to transfer angular acceleration from the white dwarf surface to the core. For weak magnetic fields, this coupling is not strong, either, leading to a belt structure on the surface of the white dwarf that is rotating faster than the core. The belt structure is coupled to the inner accretion disk, allowing for a direct influence of the accretion rate on the spin period of the belt. While this model is able to explain the observations of Cal 83, it is yet unclear if and under which circumstances it can also be applicable to the transient super soft sources.

5

If much time near a black hole is spent
You may find a horizon event.
  Getting sucked in is bad
  And will leave loved ones sad,
For they'll wonder all time where you went.

(Anonymous)

High-mass X-ray Binaries

Having discussed systems with white dwarf companions and low mass X-ray binaries, this last chapter will now present an example of a high mass X-ray binary (HMXB). Cyg X-1 provides a perfect environment for observations of a wind-accreting system. The findings in the remaining part of this chapter have in large parts taken verbatim from Hirsch et al. (2019)[1]:

5.1 Cyg X-1

Discovered during a balloon flight in 1964 (Bowyer et al., 1965), Cygnus X-1 is one of the best studied black hole X-ray binaries. The system has previously been reported to be located at a distance of $1.86^{+0.12}_{-0.11}$ kpc (Xiang et al., 2011; Reid et al., 2011), whereas new Gaia measurements favor a slightly larger distance of 2.37 ± 0.18 kpc (Gandhi et al., 2018). It consists of a $(14.8 \pm 1.0)\,M_\odot$ black hole which accretes from the strong stellar wind of the $(19.2 \pm 1.9)\,M_\odot$ supergiant O9.7 Iab star HDE 226868 (Murdin & Webster, 1971; Webster & Murdin, 1972; Walborn, 1973; Herrero et al., 1995; Caballero-Nieves et al., 2009; Orosz et al., 2011). The star and the black hole are in a quasi-circular (eccentricity $e = 0.018 \pm 0.002$; Orosz et al., 2011) 5.599829(16) d orbit (Webster & Murdin, 1972; Brocksopp et al., 1999; Gies et al., 2003) with an inclination of $i = 27.1^\circ \pm 0.8^\circ$ (Orosz et al., 2011). This corresponds to a separation between the center of mass of the star and the black hole of only $42.2\,R_\odot$, or 2.5 stellar radii. Combined with the high mass-loss rate of HDE 226868 ($\sim 10^{-6}\,M_\odot\,\mathrm{year}^{-1}$; Puls et al., 2006; Herrero et al., 1995), this small separation means that the black hole is continuously accreting material from the stellar wind, making Cyg X-1 one of the few persistent black holes in our Galaxy.

With its high absorption column density N_H around 6×10^{21} cm^{-2} (Dotani et al., 1997; Schulz et al., 2002b; Miller et al., 2002; Hanke et al., 2008), Cyg X-1 is associated with an X-ray dust scattering halo (see Bode et al., 1985, for the first analysis of this halo). Xiang et al. (2011) found a dust containing cloud in the interstellar medium (ISM) at $\sim 0.885\,D$, where D is the distance of the system, to be the region responsible for the scattering halo.

Already shortly after the identification of the optical counterpart of Cyg X-1, X-ray light curves were found to show a strong orbital modulation of the X-ray absorption column, N_H, due to absorption of X-rays from the black hole in the stellar wind (Li & Clark, 1974; Remil-

[1] Since the submission of the thesis, this paper has been accepted for publication after further adaption according to the comments of the referee. The submitted version is here reproduced with permission ©ESO.

lard & Canizares, 1984; Bałucińska-Church et al., 2000; Poutanen et al., 2008; Miškovičová et al., 2016; Grinberg et al., 2015). Together with observations of the orbital modulation of optical lines from HDE 226868 (Gies & Bolton, 1986a,b; Gies et al., 2003), these phenomena led to the picture of the stellar wind of HDE 226868 as a line driven wind or CAK wind after Castor et al. (1975) (but see also Friend & Castor, 1982; Morton, 1967) with an asymptotic velocity of $v_\infty \sim 2000\,\mathrm{km\,s^{-1}}$ (Muijres et al., 2012). This wind is disturbed by the presence of the gravitational potential of the black hole, which leads to a focusing of the wind towards the black hole (Friend & Castor, 1982; Gies & Bolton, 1986b). In addition, it is also affected by the X-rays from the compact object: While strong orbital modulation of N_H is seen during the canonical hard state of the black hole, where the X-ray spectrum is dominated by a Comptonized power law (Parker et al., 2015; Nowak et al., 2011; Wilms et al., 2006, and references therein), only little to no modulation is seen during the thermally dominated X-ray soft state (Wen et al., 1999). Optical spectra show the stellar wind to be strongly photoionized during the latter state (Gies et al., 2003; Gies et al., 2008).

Line driven winds are not expected to be smooth flows, but show strong density perturbations or "clumps" (Owocki et al., 1988; Feldmeier et al., 1997; Puls et al., 2006, 2008; Oskinova et al., 2012; Sundqvist & Owocki, 2013). In X-ray binaries, the density contrast could even be further enhanced by the interaction between the wind and the strong X-rays from the compact object (Blondin, 1994; Blondin & Woo, 1995; Manousakis & Walter, 2011; Manousakis & Walter, 2015, and references therein). For Vela X-1 and Cyg X-1 it has been estimated that more than 90% of the wind mass are contained in less than 10% of the wind volume (Sako et al., 1999; Rahoui et al., 2011). When the line of sight to the compact object passes through one of these clumps, X-rays are absorbed by the moderately ionized material in the clump, leading to a so-called "dipping event". This is also observed for other sources (Hemphill et al., 2014; Grinberg et al., 2017). During the hard state of Cyg X-1, such short-term dipping events are observed predominantly during the upper conjunction of the black hole, i.e., when the line of sight passes through the densest region of the stellar wind and is most likely to pass through a clump (Li & Clark, 1974; Mason et al., 1974; Parsignault et al., 1976; Pravdo et al., 1980; Remillard & Canizares, 1984; Kitamoto et al., 1984; Bałucińska-Church et al., 2000; Feng & Cui, 2002; Poutanen et al., 2008; Hanke et al., 2009; Miškovičová et al., 2016; Grinberg et al., 2015). The precise structure of the clumps, i.e., their density and ionization structure, is unknown. Most recent 2D simulations of such a stellar wind show a very complex evolution of velocity and density structures with the formation of characteristic small-scale clumps of various shapes embedded in areas with lower density (Sundqvist et al., 2018). They find a typical clump mass of 10^{17} g and an average clump size of 1% of the stellar radius at a distance of two stellar radii. These results confirm earlier theories and 1D simulations of Oskinova et al. (2012); Sundqvist & Owocki (2013), as well as observations by Grinberg et al. (2015); see also the review paper by Martínez-Núñez et al. (2017).

Cyg X-1 was observed several times by *Chandra* in order to collect a comprehensive dataset of all spectral states during different phases of the orbit (see Fig. 5.1 for an overview of the longest of these observations). Hanke et al. (2009, hereafter paper I) studied the hard state spectrum in superior conjunction of the black hole, i.e., around $\phi_\mathrm{orb} = 0$. They select the non-dip data from the 50 ks light curve of ObsID 3814, using a count rate limit of 82.7 counts per second (cps). Together with a contemporary *RXTE* observation, the continuum during the hard state non-dip phases can be described by an empirical broken powerlaw

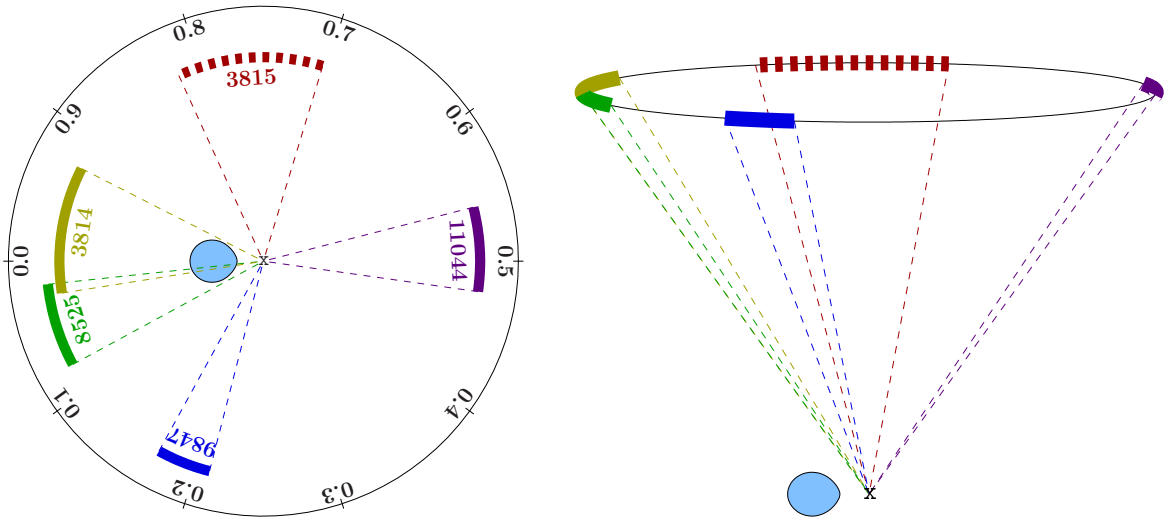

Figure 5.1: *Chandra* observations of Cyg X-1 during different orbital phases. **Left:** View from top (xy-plane, Miškovičová et al., 2016, Fig. 1); **Right:** Side view (xz-plane, Miškovičová, priv. comm.). The light blue region demarks the Roche lobe of the companion star HDE 226868, the black hole is located at the cross.

model with a high energy cutoff and a blackbody disk component. Absorption edges of overabundant elements in the *Chandra* spectrum hint towards the origin of the absorption column being not only in the ISM but also in the wind emitted by the companion star. They find absorption lines of highly ionized ions of several elements, coming from photoionized wind material near the black hole. From the detection of line series of H- and He-like ions they calculate column densities for different elements during non-dip.

In a subsequent paper, Miškovičová et al. (2016, hereafter paper II) compare *Chandra* hard state observations in different orbital phases. They find the intensity of dipping phase dependent with the strong dips happening mostly around $\phi_{\mathrm{orb}} = 0$, whereas near $\phi_{\mathrm{orb}} = 0.5$ the light curve show no dipping. The absorption columns calculated from line series are phase dependent, too. The absorbing material therefore must be source-intrinsic. It is thus not surprising that the Doppler shifts of the observed spectral lines are also found to strongly vary with phase. They infer that the stellar wind is a highly dynamical environment with a complex ionization structure.

5.2 Analysis of the dipping stages

This work follows up on the analysis of the non-dip spectra and discusses the identification and classification of dipping stages as well as spectral changes seen during the dipping episodes. Concentrating on the silicon and sulfur line regions throughout the dips, I show that lower ionization stages appear deeper in the dip. During the times with the highest absorption, the direct line of sight is blocked almost completely, and the photoionized plasma around the black hole can be observed in form of emission lines.

As the text of this chapter is taken from Hirsch et al. (2019), the phrasing “we” is used as it is the convention for publications in this field. Unless explicitly noted otherwise, however,

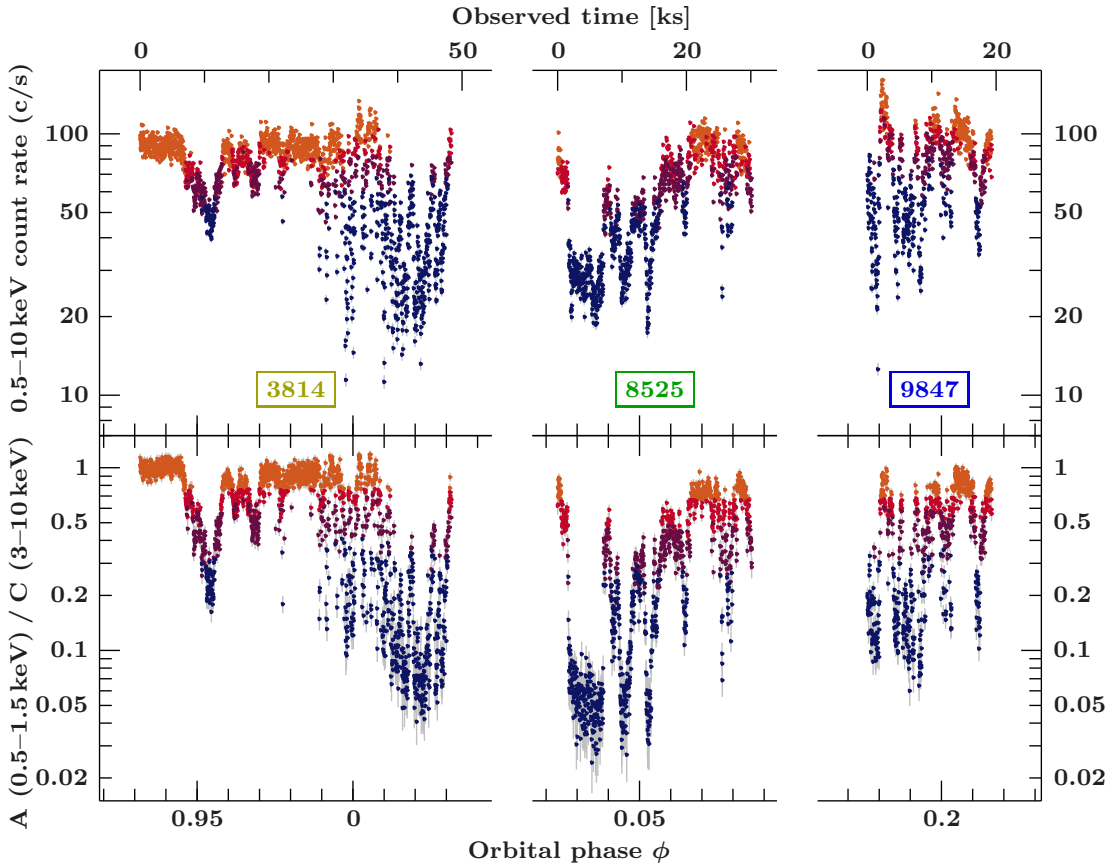

Figure 5.2: *Upper panel*: Light curves of all three observations as a function of orbital phase. *Lower panel*: Corresponding hardness ratios. All observations were in the low/hard state. Dips are strongest at $\phi_{\rm orb} \sim 0.0$, become weaker at $\phi_{\rm orb} \sim 0.2$ and $\phi_{\rm orb} \sim 0.75$, and completely fade at $\phi_{\rm orb} \sim 0.5$ (see also paper II). Colors indicate the selected dipping stages (see right panel of Fig. 5.4 for the color denotation and Sect. 5.2.1 for details on the data selection).

the work was carried out by the first author, so the reader may substitute “we” by “I”.

5.2.1 Data reduction

Out of the *Chandra*-HETGS observations discussed in paper II for their non-dip properties, we select a subsample of three observations (Table 5.1), namely ObsIDs 3814, 8525 and 9847, that show distinct dipping episodes in their light curves (Fig. 5.2, Sect. 5.2.1). All of these observations were performed in timed exposure (TE) mode. In this mode the usual frame time is 3.2 s exposure before the data are transferred into a framestore for readout. Cyg X-1 is a bright source even in the low/hard state. Therefore, for the discussed observations only a half array of the chips (512 CCD rows) was read out to avoid pile up by reducing the frame time to 1.7 s. We re-extracted the data using the Chandra Interactive Analysis of Observations (CIAO) software version 4.6 with all parameters set to default except for the HETG width factor, which we reduced from 35 to 10 in order to have a better coverage at the short wavelength end.

For the light curves and spectral analysis we use the first order spectra of the high and

Table 5.1: *Chandra*-HETGS Observations used in this paper

ObsID	Start date Date yyyy-mm-dd	MJD	Mode	$T_{\rm exp}$ [ks]	$\phi_{\rm orb}$
3814	2003-04-19	52748	TE/g	48.3	0.93–0.03
8525	2008-04-18	54574	TE/g	30.1	0.02–0.08
9847	2008-04-19	54575	TE/g	19.3	0.17–0.21

TE/g: Timed Exposure, graded; $T_{\rm exp}$: exposure time; $\Phi_{\rm orb}$: orbital phase according to the ephemeris of Gies et al. (2003).

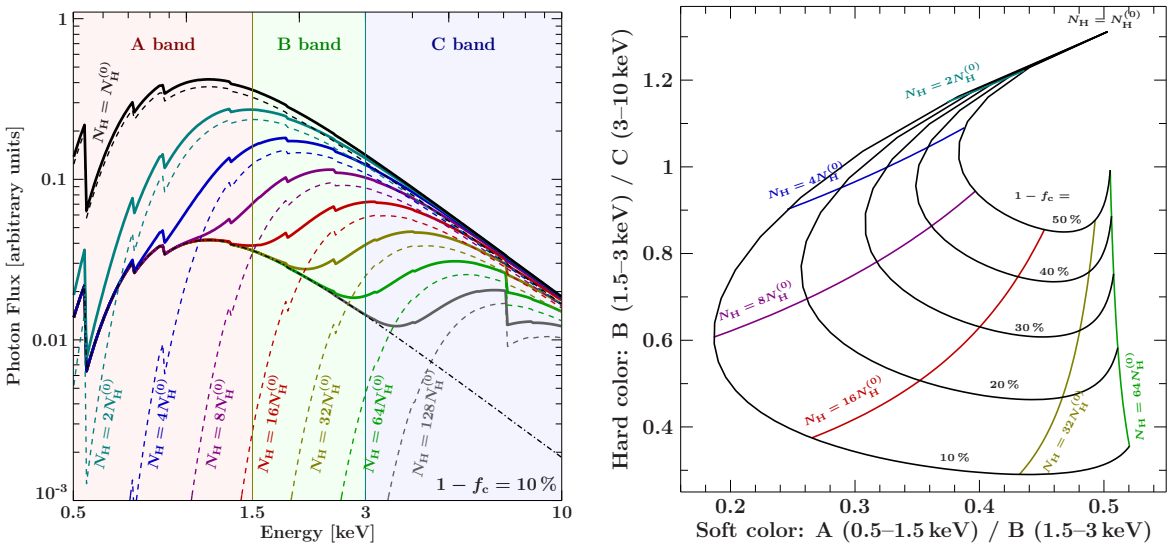

Figure 5.3: Left: Effect of partial absorption with increasing $N_{\rm H}$ at constant covering fraction with $N_{\rm H}^{(0)} = 0.54 \times 10^{22}$ after paper I (Hanke, 2011, Fig. 2.64). Right: Color-color diagram showing the tracks for different covering fractions and column densities of the second absorber. See text for details.

medium energy gratings (HEG, MEG Canizares et al., 2005). Because of the excellent background discrimination of the data extraction process (order sorting), any remaining background is negligible compared to the bright source. We therefore do not subtract any background from the final spectra. All further data analysis was performed with the Interactive Spectral Interpretation System version 1.6.2 (ISIS; Houck & Denicola, 2000; Houck, 2002; Noble & Nowak, 2008).

Light curves

Hanke (2011) already stated that the light curves of ObsIDs 3814 (∼48 ks) and 8525 (∼30 ks) slightly overlap in orbital phase ($\phi_{\rm orb} = 0.93$–0.03 and $\phi_{\rm orb} = 0.02$–0.08) and show a very similar morphology of strong absorption dips. ObsID 9847 (∼19 ks) at $\phi_{\rm orb} = 0.17$–0.21 was taken within the same binary orbit as ObsID 8525; it contains absorption dips as well, though they are less pronounced than at $\phi_{\rm orb} \sim 0$. Dips can last from several seconds to more than 10 minutes (Kitamoto et al., 1984). To uncover also the shorter dips we extracted light curves with a 25.5 s resolution. For a detailed description of the dataset as well as for

a detailed analysis of the non-dip spectrum of individual observations we refer to paper I and paper II. Paper II also discusses ObsID 11044 (∼30 ks), which at $\phi_{\rm orb} = 0.48$–0.54 for the first time provides high-resolution spectroscopy of Cyg X-1 during lower conjunction, i.e., when our line of sight passes outside of the focused wind. As this light curve is virtually free of dipping, except for maybe extremely short dips beyond the resolution of the light curve, which do not affect the spectrum (paper II), we do not discuss it here in detail. Cyg X-1 was in a comparable hard state during ObsIDs 3814, 8525 and 9847 according to the ASM classification by Grinberg et al. (2013); see also the more detailed discussion of the source state in paper II. We do not use ObsID 3815 as it shows much less dipping than the other hard state observations, not allowing for a distinction between different dip stages (paper II, see also Miškovičová et al., 2011).

Color-color diagrams

As we will discuss in more detail below, the dips are due to absorption events caused by material in the line of sight to the primary source of X-rays. Dipping events such as the ones seen in Cyg X-1 are transient events characterized by quickly varying spectral shape. This strong variability complicates the spectral analysis. Ideally, one would want to study how the spectral shape – photon index, absorption/emission lines, and continuum absorption – varies with time, but the limited signal to noise of our observations renders this impossible. We therefore have to resort to some kind of averaging technique in which we extract spectra from time intervals where we believe that the spectral shape is at least representative for a given part of a dip. We find these time intervals by looking at the time resolved spectral behavior of the source as represented in so-called "color-color diagrams".

Figure 5.3, as already shown in Hanke (2011), shows how absorption affects an observed primary power law continuum with $\Gamma = 1.73$ (typical for Cyg X-1 in the hard state, e.g., Grinberg et al., 2013) that is fully covered by material with a fixed column density $N_{\rm H}^{(0)}$ (e.g., the outer parts of the stellar wind or absorption in the interstellar medium). For this paper, we set $N_{\rm H}^{(0)}$ to the fit result of paper I, $N_{\rm H}^{(0)} = 0.54 \times 10^{22}\,{\rm cm}^{-2}$. In most astrophysical sources, the structures responsible for dipping will not cover the whole primary X-ray source, rather a partial coverer is present in these systems which covers a fraction $f_{\rm c}$ of the source with a column $N_{\rm H}$ (i.e., $1 - f_{\rm c}$ remains uncovered). A possible physical picture for such a partial coverer would be an optically thick cloud that is smaller in (angular) size than the X-ray source, or a cloud that passes very quickly over the X-ray source, covering the source only for part of the integration time. The observer therefore sees the sum of the uncovered spectrum (dash-dotted line in Fig. 5.3) and the covered spectrum (dashed lines). The summed spectrum is shown as solid lines in Fig. 5.3. The left panel of Figure 5.3 shows the observed spectral shapes for a constant covering factor $f_{\rm c} = 90\%$ and for varying optical depths of the covering medium (up to $128 N_{\rm H}^{(0)}$). As $N_{\rm H}$ is increased, the partial coverer removes most of the flux at soft energies and only the direct component remains visible (Hanke, 2011).

Because absorption events are typically of rather short duration, the detailed spectral shape is often not directly observable. It is, however, possible to characterize the spectral shape using X-ray colors or hardness ratios (see, e.g., Hanke et al., 2008; Nowak et al., 2011, for similar approaches). Here, we define the X-ray hardness ratio as the ratio of the count rates in two energy bands. In order to be consistent with paper I we define the ratio such that

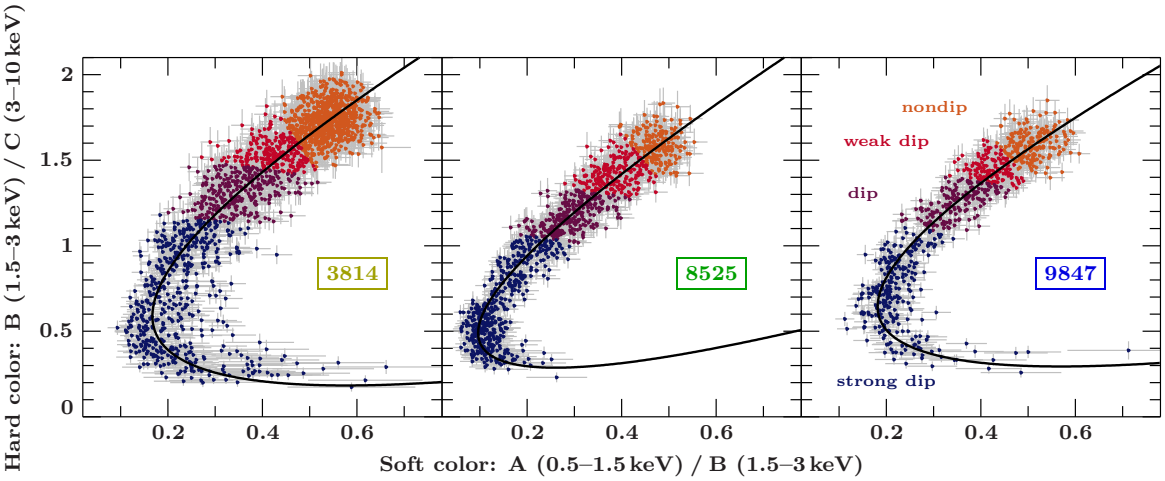

Figure 5.4: Color-color diagrams for all three observations, showing hardness ratios calculated for soft, intermediate, and hard X-ray bands. As discussed in the text, the observed tracks are determined by absorption: following the track from the upper right corner, representing the persistent flux, to the lower left corner, showing dips, absorption increases and therefore both colors become harder. During the deepest dips, the softer color becomes softer again, while the hard color does not change. This behavior can be explained by partial covering (Sect. 5.2.1). The spectrum hardens considerably during these dips. The colors denote the four different dip stages (see right panel), the black line indicates our polynomial fit to the track, see Sect. 5.2.1 for details.

its value increases as the spectrum softens, so technically this ratio is a "softness ratio". We calculate hardness ratios using the fluxes measured in three energy bands – denoted as A (0.5–1.5 keV ≡ 24.8–8.27 Å), B (1.5–3.0 keV ≡ 8.27–4.13 Å), and C (3.0–10.0 keV ≡ 4.13–1.24 Å) – to characterize the spectral shape in this way.

The right hand panel of Fig. 5.3 displays the locus of such colors for the spectral shape discussed above and several different covering fractions. For a constant f_c, a characteristic track in the color-color diagram becomes apparent, as already described by Hanke (2011): At low $N_H \sim N_H^{(0)}$, the covered component dominates the spectrum and the source is found in the top right of the diagram. Since photoabsorption first influences the soft bands, increasing N_H will decrease both, A/B and B/C, and the source will move towards the lower left of the diagram. At intermediate N_H, the A-band is dominated by the (constant) uncovered fraction, but increasing N_H still decreases B and C. For this reason, A/B starts to increase again, while B/C continues to decrease, such that the track the source in the color-color-diagram starts to turn towards the right. When the contribution of the covered component to both A and B bands is almost negligible, A/B remains constant, while B/C increases with increasing N_H. This behavior leads to a horizontal track where the source moves to the right in the color-color diagram. Finally, for the largest N_H the entire covered fraction will be removed from the observable spectrum such that we expect the X-ray color to move asymptotically back to its unabsorbed value (Hanke, 2011).

Dip selection

We now apply the ideas discussed above to Cyg X-1. Figure 5.4 shows the hardness ratios measured during the three observations considered here. The data show a behavior similar to that expected from partial covering: Data outside of dips (orange data points) are barely

Table 5.2: Exposure time, t_{exp}, and dip stage averaged count rates for the total observations and silicon (1.605 to 2.045 keV ≡ 7.725 to 6.063 Å) and sulfur (2.295 to 2.7 keV ≡ 5.402 to 4.6 Å) bands for all observations.

			Counts		
		t_{exp}	Total	Si	S
		[ks]	[10^3 counts s^{-1}]		
3814	nondip	21.096	1838	37	92
	weak dip	6.095	445	10	26
	dip	7.345	461	13	31
	strong dip	12.559	458	21	49
8525	nondip	5.079	450	11	22
	weak dip	5.313	394	11	26
	dip	6.834	406	13	28
	strong dip	12.200	401	20	41
9847	nondip	4.880	499	12	24
	weak dip	3.273	294	8	16
	dip	4.083	307	9	19
	strong dip	6.618	303	15	29

absorbed, as the source enters deeper dips (bluer colors), it follows a track that resembles the theoretical tracks shown in Fig. 5.3, including a turning point where the soft color becomes softer, while the hard color barely changes.

To study the spectral shapes during different phases of the dips in more detail, we extract data from time intervals that correspond to various stages of dipping. A direct comparison of the data with theoretical tracks shows, however, that there are deviations from the simple picture discussed above. Such deviations could be indicative of changes in both, the covering fraction and N_H, as well as due to the fact that the underlying X-ray continuum is more complex than a simple absorbed power law. We therefore determine the shape of the track empirically by fitting[2] a curve to the scatter plot. This curve is described through a parameterized polynomial of 2nd degree for each of the two colors in the diagram. To find the polynomial coefficients, a χ^2 minimization algorithm is used to optimize the shortest distance of each data point to the curve.

To select data from the dips, we first remove the non-dip data as defined in paper II[3]. This ensures consistency with the earlier results from paper II. For the remaining data, corresponding to various degrees of dipping, the goal is to find the highest possible resolution in terms of number of dipping stages, while maintaining a good enough signal-to-noise ratio to be able to constrain the spectral fits well. To find this balance, we start out with a large number of twelve segments, which are chosen such that each slice contains roughly the same number of counts. Then, starting at the deepest dipping stage (lower right-hand corner of

[2]The fits were performed by Natalie Hell, priv. comm.
[3]Note that the simpler non-dip selection in paper II was done using only the ratio A/C.

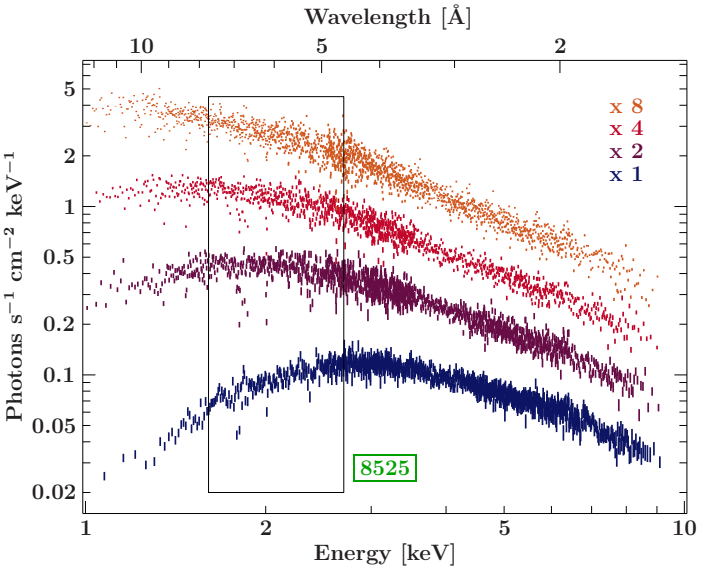

Figure 5.5: Rebinned HEG spectra of the different dipping stages of ObsID 8525. For clarity, the nondip spectrum (orange, S/N $\geq$ 13) is scaled by a factor of 8, the weak dip spectrum (red, S/N $\geq$ 15) by a factor of 4, and the dip spectrum (violet, S/N $\geq$ 15) by a factor of 2. The strong dip spectrum (blue, S/N $\geq$ 17) is not scaled. The box marks the region containing the Si and S lines. The color scheme is the same as in Figures 5.2 and 5.4.

the color-color diagram) we successively combine these small segments until the signal to noise ratio of the resulting spectra is sufficient to detect all possible lines of the Si and S series, but keep the number of segments for this as low as possible to be able to distinguish more different dip stages. These combined segments constitute the selection for the deepest dipping stage for further analysis. Subsequently, the selection of the next dipping stages follow the same approach until all twelve segments are sorted.

For all observations we obtain the best results by defining three dipping stages in addition to the non-dip phase, each consisting out of four of the smaller segments. Consequently, the three stages each have roughly the same number of counts within an observation. The four dipping stages for each observation are classified as 'non-dip', 'weak-dip', 'dip', and 'strong dip' (see Fig. 5.4 as well as Table 5.2 for the count rates and exposure of each dip stage).

5.2.2 Spectral evolution from non-dip to dip

Figure 5.5 shows the evolution of the spectrum during dipping for ObsID 8525. In addition to the general change in spectral shape due to photoelectric absorption, we see strong changes between the individual dipping stages in the region between 1.6 keV and 2.7 keV (7.7–4.6 Å), where absorption lines of silicon and sulfur ions are the most prominent spectral features (box in Fig. 5.5, see also Miškovičová et al. 2011). We will therefore concentrate on these Si and S lines.

Si and S regions

For a detailed analysis of the Si and S absorption lines, we take into account the ±1 order HEG and MEG spectra. We combine both spectra for the HEG and the MEG, and fit the spectra without rebinning them. For clarity reasons, all figures show the combined HEG and MEG spectra, where the higher resolution of the HEG is rebinned to the lower resolution of the MEG. This combination of HEG and MEG, however, only applies to the display of the data, not to the actual fitting.

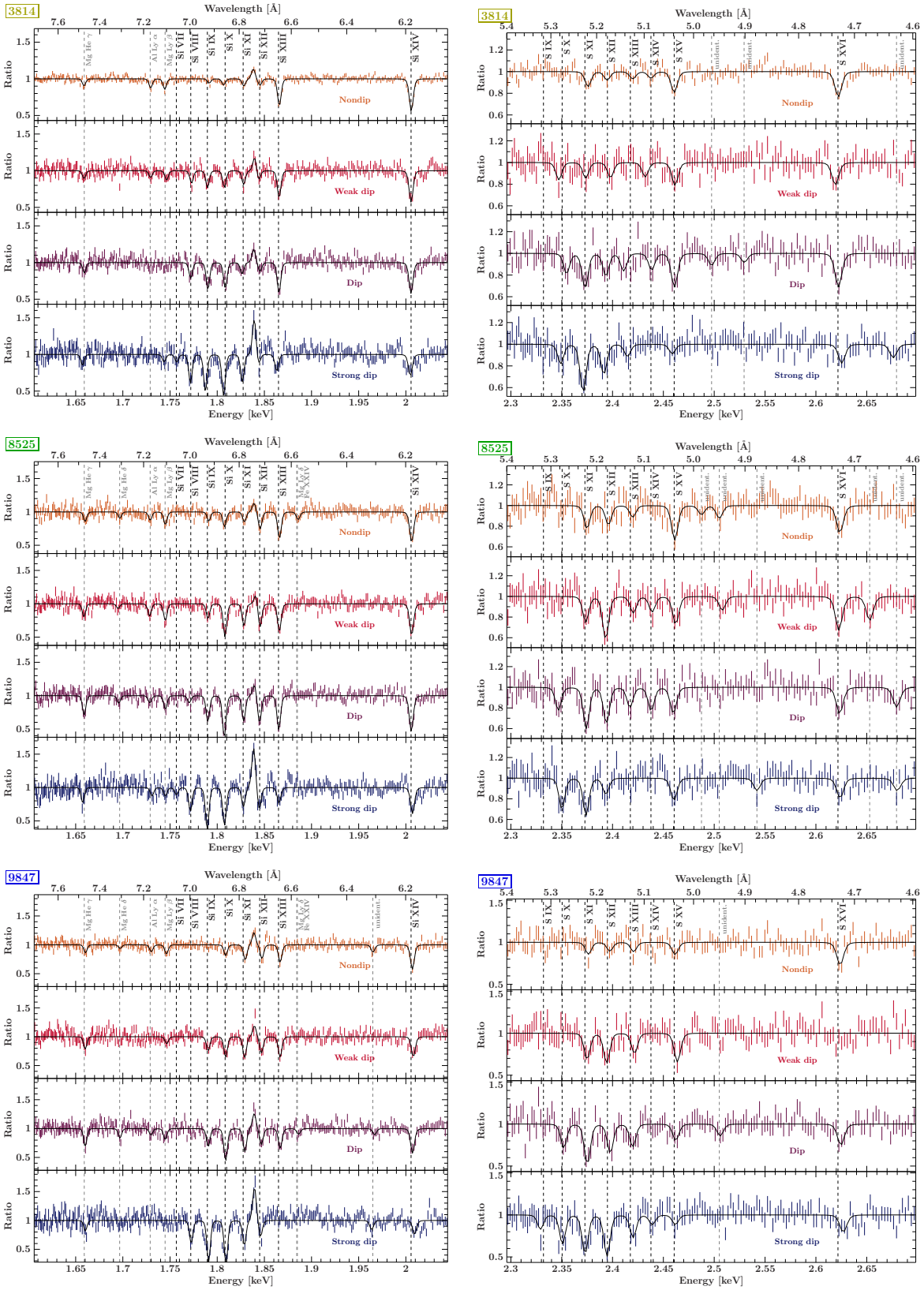

Figure 5.6: Evolution of silicon and sulfur lines with dipping stages. The panels show combined HEG and MEG ± first order spectra normalized to their respective continua. The solid black line shows the line fits.

Table 5.3: Detector constants and continuum parameters for all observations. Note that the powerlaw fits are applied to a very local continuum (1.605–2.045 keV ≡ 7.725–6.063 Å for the Si region and 2.295–2.7 keV ≡ 5.402–4.6 Å for the S region). The detector constant accounts for the different flux normalizations of the HEG and the MEG.

3814		detector constant	power law norm [photons keV^{-1} cm^{-2} s^{-1}]	photon index
Si region	nondip	0.779 ± 0.005	$0.709^{+0.017}_{-0.016}$	1.12 ± 0.04
	weak dip	0.830 ± 0.010	$0.493^{+0.024}_{-0.023}$	0.84 ± 0.08
	dip	0.873 ± 0.010	$0.306^{+0.015}_{-0.014}$	0.43 ± 0.08
	strong dip	$0.958^{+0.014}_{-0.013}$	0.057 ± 0.004	-0.83 ± 0.10
S region	nondip	0.948 ± 0.010	$1.14^{+0.13}_{-0.12}$	1.60 ± 0.12
	weak dip	0.966 ± 0.018	$0.87^{+0.22}_{-0.18}$	1.42 ± 0.25
	dip	$0.985^{+0.018}_{-0.017}$	$0.74^{+0.18}_{-0.15}$	1.37 ± 0.23
	strong dip	1.010 ± 0.018	$0.088^{+0.023}_{-0.018}$	-0.31 ± 0.25
8525		detector constant	power law norm [photons keV^{-1} cm^{-2} s^{-1}]	photon index [$\times 10^{-4}$]
Si region	nondip	0.791 ± 0.009	0.63 ± 0.04	0.95 ± 0.09
	weak dip	$0.832^{+0.011}_{-0.010}$	$0.457^{+0.025}_{-0.023}$	0.70 ± 0.09
	dip	0.900 ± 0.012	$0.247^{+0.014}_{-0.013}$	0.20 ± 0.09
	strong dip	0.989 ± 0.016	$0.0368^{+0.0025}_{-0.0023}$	-1.27 ± 0.11
S region	nondip	$1.000^{+0.022}_{-0.021}$	$1.04^{+0.25}_{-0.20}$	1.45 ± 0.23
	weak dip	0.960 ± 0.020	$0.56^{+0.17}_{-0.13}$	0.87 ± 0.28
	dip	0.987 ± 0.019	$0.44^{+0.12}_{-0.10}$	0.84 ± 0.26
	strong dip	$1.022^{+0.020}_{-0.019}$	$0.082^{+0.025}_{-0.017}$	$-0.33^{+0.29}_{-0.26}$
9847		detector constant	power law norm [photons keV^{-1} cm^{-2} s^{-1}]	photon index [$\times 10^{-4}$]
Si region	nondip	0.728 ± 0.008	0.84 ± 0.04	1.08 ± 0.08
	weak dip	0.773 ± 0.012	0.62 ± 0.04	0.84 ± 0.11
	dip	0.846 ± 0.013	$0.374^{+0.026}_{-0.024}$	$0.43^{+0.12}_{-0.11}$
	strong dip	0.970 ± 0.018	0.062 ± 0.005	-1.12 ± 0.12
S region	nondip	0.925 ± 0.019	$1.29^{+0.26}_{-0.27}$	$1.50^{+0.20}_{-0.25}$
	weak dip	$0.958^{+0.030}_{-0.029}$	$1.4^{+0.5}_{-0.4}$	$1.74^{+0.29}_{-0.30}$
	dip	$0.978^{+0.029}_{-0.028}$	$0.64^{+0.20}_{-0.16}$	$1.01^{+0.29}_{-0.30}$
	strong dip	$1.003^{+0.030}_{-0.029}$	$0.16^{+0.06}_{-0.04}$	0.1 ± 0.4

As the emphasis of this paper is on the behavior of the Si and S lines, we do not attempt to model the broad-band Chandra continuum or the continuum absorption, but rather describe the local spectra in the Si (1.605–2.045 keV ≡ 7.725–6.063 Å) and the S (2.295–2.7 keV ≡ 5.402–4.6 Å) region. These regions are narrow enough in energy that the curvature due to

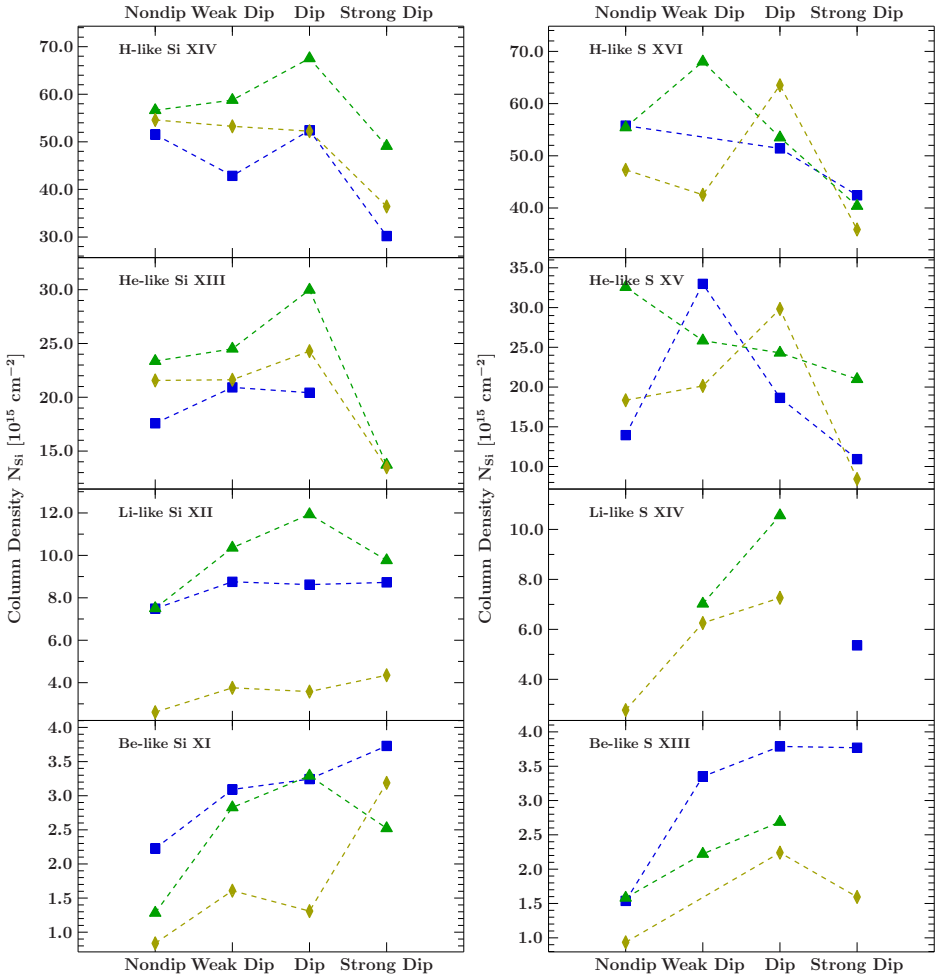

Figure 5.7: Column density for each dip stage derived from the respective equivalent width for H-like through Be-like Si and S ion lines detected in ObsIDs 3814 (yellow diamonds), 8525 (green triangles) and 9847 (blue squares). The column densities of lower charged ions become stronger with increasing dip depth, whereas column densities of highly charged ions become less prominent. Note that Be-like Si XI and Li-like Si XII lines are contaminated by the Si He z emission line. The figure is continued on the next page with B-like through O-like ions.

the absorption is negligible. We can therefore describe the local absorbed continuum by a simple power law (obviously, the photon indices of the continuum will be different in both bands).

A further complication is that due to the source brightness the nondip, weak dip, and to a lesser extent also the dip spectra are affected by slight pileup. The major effect that pileup has on our narrow-band data is a change in count rate, which is seen as a change in the relative flux normalization of both spectra, as pileup affects the MEG more strongly than the HEG due to the significantly smaller spectral resolution[4]. We can compensate for this effect by including a multiplicative, detector dependent constant in the spectral modeling. Due to the narrow energy bands considered here, a further pileup correction is not necessary:

[4]See 'The Chandra ABC Guide to Pileup', CXC, 2010, http://cxc.harvard.edu/ciao/download/doc/pileup_abc.pdf

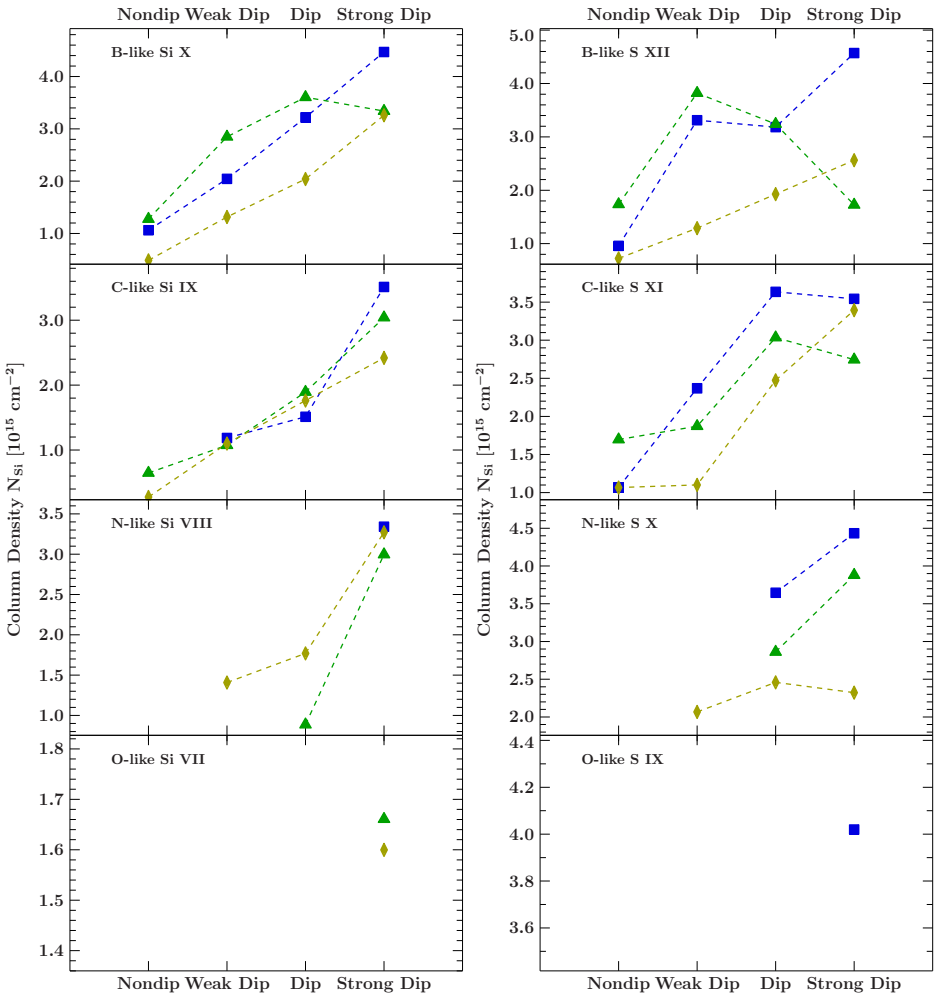

Figure 5.7: Continued from page before: Column density for each dip stage derived from the respective equivalent width for B-like through O-like Si and S ion lines detected in ObsIDs 3814 (yellow diamonds), 8525 (green triangles) and 9847 (blue squares). The column densities of lower charged ions become stronger with increasing dip depth, whereas column densities of highly charged ions become less prominent.

The pileup fraction is a slowly changing function of energy such that it does not appreciably affect the equivalent width of the lines considered here (due to the nature of X-ray gratings line energies are not affected).

The local continuum being accounted for (see Table 5.3 for parameters), we model the absorption lines in both regions using additive Gaussian line profiles (Fig. 5.6). These profiles give a slightly better description of the line shapes than Voigt profiles. For the absorption lines, the line width σ was frozen at 1.2 eV (silicon) and 1.8 eV (sulfur), well below the detector resolution. Lines were identified using energies from Hell et al. (2016), Porquet et al. (2010), and from AtomDB, version 2.0.0[5]. We find blended line complexes for L-shell ions, He w lines for He-like ions, and Ly α lines for H-like ions of both silicon and sulfur. In addition to the K α absorption line series, there is the forbidden He-like Si XIII z line in emission (1.8394 keV $\equiv$ 6.7405 Å, $1s2s\,^3S_1 \rightarrow 1s^2\,^1S_0$, Porquet et al., 2010, this line is sometimes

[5]see http://www.atomdb.org; line energies without a reference refer to AtomDB.

also called the He-like Si XIII f line). Note that there is a degeneracy between the Be-like Si XI and Li-like Si XII absorption lines at 1.8275 keV ≡ 6.7844 Å and 1.8450 keV ≡ 6.7200 Å (both energies from Hell et al., 2016) and the forbidden He-like Si XIII z emission line. This increases the uncertainty of the respective fit values.

Table 5.4: Observed silicon and sulfur line centers for all observations.

3814	Ion		E_{obs} [keV]			
			nondip	weak dip	dip	strong dip
	H-like	Si XIV	2.00574(23)	2.0055(5)	2.0054(6)	2.0048(26)
	He-like	Si XIII	1.86588(22)	1.8656(6)	1.8655(4)	1.8632(11)
	Li-like	Si XII	1.8452(17)	1.8440(28)	1.8451(26)	1.8437(14)
	Be-like	Si XI	1.8283(8)	1.8280(7)	1.8264(19)	1.8267(7)
	B-like	Si X	1.8069(17)	1.8077(11)	1.8086(8)	1.80678(43)
	C-like	Si IX	1.7916(13)	1.7897(8)	1.7902(9)	1.7875(6)
	N-like	Si VIII	–	1.7728(8)	1.7719(7)	1.7717(5)
	O-like	Si VII	–	–	–	1.7571(15)
	H-like	S XVI	2.6220(9)	2.6191(22)	2.6222(11)	2.6254(20)
	He-like	S XV	2.4606(9)	2.4614(24)	2.4608(12)	2.459(6)
	Li-like	S XIV	2.4378(22)	2.4321(30)	2.4385(19)	–
	Be-like	S XIII	2.420(4)	–	2.4110(88)	2.4147(29)
	B-like	S XII	2.3947(25)	2.3980(24)	2.3934(21)	2.3914(19)
	C-like	S XI	2.3759(16)	2.374(7)	2.3730(18)	2.3710(11)
	N-like	S X	–	2.3472(23)	2.3548(22)	2.3490(35)
	O-like	S IX	–	–	–	–

8525	Ion		E_{obs} [keV]			
			nondip	weak dip	dip	strong dip
	H-like	Si XIV	2.0061(5)	2.0061(5)	2.0057(4)	2.0070(7)
	He-like	Si XIII	1.8660(5)	1.8659(5)	1.8653(4)	1.8656(11)
	Li-like	Si XII	1.8454(8)	1.8452(18)	1.8448(6)	1.8446(9)
	Be-like	Si XI	1.8289(10)	1.8284(5)	1.8281(4)	1.8278(6)
	B-like	Si X	1.8078(9)	1.80823(47)	1.80748(31)	1.80772(41)
	C-like	Si IX	1.7911(13)	1.7903(9)	1.7901(7)	1.78944(38)
	N-like	Si VIII	–	–	1.7705(27)	1.7716(6)
	O-like	Si VII	–	–	–	1.7568(21)
	H-like	S XVI	2.6236(17)	2.6225(13)	2.6234(18)	2.6238(22)
	He-like	S XV	2.4612(11)	2.4621(17)	2.4598(15)	2.4604(19)
	Li-like	S XIV	–	2.4389(24)	2.4380(17)	–
	Be-like	S XIII	2.4198(27)	2.4204(23)	2.4171(16)	–
	B-like	S XII	2.3959(29)	2.3932(9)	2.3940(11)	2.3934(23)
	C-like	S XI	2.3749(17)	2.3737(18)	2.3742(10)	2.3739(20)
	N-like	S X	–	–	2.3467(17)	2.3502(15)
	O-like	S IX	–	–	–	–

Table 5.4 (continued)

9847	Ion		E_{obs} [keV]			
			nondip	weak dip	dip	strong dip
	H-like	Si XIV	2.0069(4)	2.0079(10)	2.0070(7)	2.0092(12)
	He-like	Si XIII	1.8668(6)	1.8667(6)	1.8668(7)	–
	Li-like	Si XII	1.8474(6)	1.8468(10)	1.8468(9)	1.8459(10)
	Be-like	Si XI	1.8297(6)	1.8291(5)	1.8293(6)	1.8287(5)
	B-like	Si X	1.8089(9)	1.8090(8)	1.8090(5)	1.80928(37)
	C-like	Si IX	–	1.7904(13)	1.7905(14)	1.79092(37)
	N-like	Si VIII	–	–	–	1.7725(5)
	O-like	Si VII	–	–	–	–
	H-like	S XVI	2.6238(12)	–	2.6246(19)	2.6269(39)
	He-like	S XV	2.4615(23)	2.4637(14)	2.4621(30)	2.4618(36)
	Li-like	S XIV	–	–	–	2.4391(33)
	Be-like	S XIII	2.4207(23)	2.4216(16)	2.4198(25)	2.4202(17)
	B-like	S XII	2.397(4)	2.3942(16)	2.3978(15)	2.3945(11)
	C-like	S XI	2.3763(20)	2.3750(18)	2.3752(11)	2.3730(14)
	N-like	S X	–	–	2.3520(17)	2.3508(22)
	O-like	S IX	–	–	–	2.3291(26)

Finally, in the strong dip spectrum of ObsID 9847, there are indications for a O-like S IX K α line which appears once the HEG data are rebinned to match the (unbinned) MEG grid and both are combined for display. This line is too weak for us to be able to constrain its parameters such that we only claim a tentative detection of O-like S IX. The values for central line energies and equivalent widths of all detected silicon and sulfur absorption lines can be found in Tables 5.4 and 5.5. Note that the lower ionization stages (N-like and O-like ions) only appear deeper in the dips. This hints towards a shell-like ionization structure of the clumps with a hot, highly ionized surface and cooler and less ionized parts in the core.

In addition to these lines from S and Si we also find an Al XIII Ly α[6] absorption line (1.7285 keV $\equiv$ 7.1729 Å), Mg He γ (1.6591 keV $\equiv$ 7.4730 Å, $1s^2\,{}^1S_0$–$1s4p\,{}^1P_1$) and He δ (1.6961 keV $\equiv$ 7.3100 Å, $1s^2\,{}^1S_0$–$1s5p\,{}^1P_1$) absorption lines, and we detect Mg XII Ly β (1.7447 keV $\equiv$ 7.1063 Å) and, in some cases, a hint of Mg Ly δ (1.8843 keV $\equiv$ 6.5799 Å) blended with an Fe XXIV transition (1.8851 keV $\equiv$ 5.5771 Å, $1s^22s\,{}^2S_{1/2}$–$1s^27p\,{}^2P_{3/2}$). These lines imply the presence of Mg Ly γ at 1.840 keV $\equiv$ 6.738 Å, i.e., blended with He-like Si z. We expect Mg Ly γ to be very weak but it may slightly contaminate our measurements of the Si He z and the Li-like Si XII line, thus further contributing to the uncertainty of the fit values.

Equivalent widths / line strengths and column densities

The equivalent widths of the silicon and sulfur lines vary around 1 eV, with rather large error bars for the weaker lines (Table 5.5). Note that the He-like Si XIII z emission line additionally increases the uncertainties of the Si XI and Si XII lines. Comparing the lines in the different dipping stages reveals that the line strengths of the low charge states – and thus the re-

[6] Lines denoted here as part of the Lyman series typically have two unresolved components with the configuration of $1s_{1/2}\,{}^2S_{1/2}$–$np_{3/2}\,{}^2P_{3/2}$ and $1s_{1/2}\,{}^2S_{1/2}$–$np_{1/2}\,{}^2P_{1/2}$, respectively. α, β, γ etc. are represented by the principal quantum number $n = 2, 3, 4, \ldots$. The line energy given in the text corresponds to the components' mean energy, weighted with the respective statistical weight (2:1).

Table 5.5: Evolution of the equivalent widths of the silicon and sulfur lines during the dipping stages for all observations.

3814	Ion		Equivalent Width [eV]			
			non-dip	weak-dip	dip	strong-dip
	H-like	Si XIV	-2.48 ± 0.14	$-2.42^{+0.29}_{-0.28}$	$-2.38^{+0.29}_{-0.28}$	-1.7 ± 0.4
	He-like	Si XIII	-1.92 ± 0.14	-1.93 ± 0.28	-2.16 ± 0.27	-1.2 ± 0.4
	Li-like	Si XII	-0.46 ± 0.16	$-0.7^{+0.4}_{-1.0}$	-0.6 ± 0.4	$-0.8^{+0.5}_{-0.6}$
	Be-like	Si XI	-0.49 ± 0.13	-0.95 ± 0.25	$-0.77^{+0.27}_{-0.26}$	-1.88 ± 0.28
	B-like	Si X	-0.42 ± 0.14	$-1.13^{+0.26}_{-0.25}$	-1.76 ± 0.24	-2.81 ± 0.26
	C-like	Si IX	-0.28 ± 0.14	-1.13 ± 0.25	$-1.80^{+0.25}_{-0.24}$	$-2.48^{+0.27}_{-0.26}$
	N-like	Si VIII	–	-0.83 ± 0.26	-1.05 ± 0.26	-1.94 ± 0.29
	O-like	Si VII	–	–	–	-0.5 ± 0.4
	H-like	S XVI	-2.2 ± 0.4	-1.9 ± 0.8	-2.9 ± 0.7	-1.6 ± 0.7
	He-like	S XV	-1.6 ± 0.4	-1.8 ± 0.7	-2.7 ± 0.6	-0.8 ± 0.7
	Li-like	S XIV	-0.5 ± 0.4	-1.1 ± 0.7	-1.3 ± 0.7	–
	Be-like	S XIII	-0.6 ± 0.4	–	-1.3 ± 0.7	-1.0 ± 0.7
	B-like	S XII	-0.6 ± 0.4	-1.1 ± 0.7	-1.7 ± 0.7	-2.3 ± 0.7
	C-like	S XI	-1.1 ± 0.4	-1.2 ± 0.9	-2.6 ± 0.7	-3.6 ± 0.7
	N-like	S X	–	-1.3 ± 0.8	-1.5 ± 0.8	-1.4 ± 0.8
	O-like	S IX	–	–	–	–

8525	Ion		Equivalent Width [eV]			
			non-dip	weak-dip	dip	strong-dip
	H-like	Si XIV	$-2.58^{+0.29}_{-0.28}$	-2.67 ± 0.30	-3.07 ± 0.28	-2.2 ± 0.4
	He-like	Si XIII	-2.08 ± 0.28	-2.18 ± 0.29	-2.67 ± 0.28	-1.2 ± 0.4
	Li-like	Si XII	-1.3 ± 0.4	-1.8 ± 0.4	-2.1 ± 0.4	-1.7 ± 0.4
	Be-like	Si XI	-0.76 ± 0.26	-1.67 ± 0.25	-1.94 ± 0.25	-1.5 ± 0.4
	B-like	Si X	-1.10 ± 0.25	$-2.46^{+0.24}_{-0.23}$	$-3.11^{+0.22}_{-0.21}$	-2.88 ± 0.28
	C-like	Si IX	-0.66 ± 0.25	-1.10 ± 0.26	-1.94 ± 0.25	$-3.11^{+0.27}_{-0.26}$
	N-like	Si VIII	–	–	-0.52 ± 0.30	-1.8 ± 0.4
	O-like	Si VII	–	–	–	-0.5 ± 0.4
	H-like	S XVI	-2.5 ± 0.8	-3.1 ± 0.8	-2.4 ± 0.8	-1.8 ± 0.8
	He-like	S XV	-2.9 ± 0.7	-2.3 ± 0.7	-2.2 ± 0.7	-1.9 ± 0.7
	Li-like	S XIV	–	$-1.3^{+0.8}_{-0.7}$	-1.9 ± 0.7	–
	Be-like	S XIII	-0.9 ± 0.7	-1.3 ± 0.8	-1.6 ± 0.7	–
	B-like	S XII	-1.5 ± 0.7	-3.4 ± 0.7	-2.9 ± 0.7	-1.5 ± 0.8
	C-like	S XI	-1.8 ± 0.7	-2.0 ± 0.8	-3.2 ± 0.7	-2.9 ± 0.7
	N-like	S X	–	–	$-1.8^{+0.8}_{-0.7}$	$-2.4^{+0.8}_{-0.7}$
	O-like	S IX	–	–	–	–

Table 5.5 (continued)

9847	Ion		Equivalent Width [eV]			
			non-dip	weak-dip	dip	strong-dip
	H-like	Si XIV	$-2.34^{+0.28}_{-0.27}$	-1.9 ± 0.4	-2.4 ± 0.4	-1.4 ± 0.5
	He-like	Si XIII	-1.56 ± 0.28	-1.9 ± 0.4	-1.8 ± 0.4	–
	Li-like	Si XII	-1.3 ± 0.4	-1.6 ± 0.5	$-1.5^{+0.4}_{-0.5}$	-1.5 ± 0.5
	Be-like	Si XI	-1.31 ± 0.24	-1.82 ± 0.29	-1.91 ± 0.29	-2.2 ± 0.4
	B-like	Si X	-0.92 ± 0.24	-1.76 ± 0.29	-2.78 ± 0.26	$-3.86^{+0.27}_{-0.26}$
	C-like	Si IX	–	-1.2 ± 0.4	$-1.55^{+0.31}_{-0.30}$	-3.60 ± 0.28
	N-like	Si VIII	–	–	–	-2.0 ± 0.4
	O-like	Si VII	–	–	–	–
	H-like	S XVI	-2.5 ± 0.7	–	-2.3 ± 0.9	-1.9 ± 0.9
	He-like	S XV	-1.2 ± 0.7	-2.9 ± 0.8	-1.7 ± 0.9	-1.0 ± 0.9
	Li-like	S XIV	–	–	–	-1.0 ± 0.9
	Be-like	S XIII	-0.9 ± 0.7	-2.0 ± 0.8	-2.3 ± 0.8	-2.3 ± 0.8
	B-like	S XII	-0.8 ± 0.7	-2.9 ± 0.8	-2.8 ± 0.8	-4.0 ± 0.8
	C-like	S XI	-1.1 ± 0.7	$-2.5^{+0.9}_{-0.8}$	-3.9 ± 0.8	-3.8 ± 0.8
	N-like	S X	–	–	$-2.3^{+0.9}_{-0.8}$	-2.7 ± 0.9
	O-like	S IX	–	–	–	-1.4 ± 1.0

spective column densities – increase with dipping, while those of the higher charge states decrease (Fig. 5.7). This shift in charge balance alone is already strong evidence supporting the theory of a highly structured medium where "clumps" of colder, denser material are embedded in a highly ionized plasma (Oskinova et al., 2012; Sundqvist & Owocki, 2013, and references therein).

For optically thin absorption lines, the equivalent width directly translates into the column density of the parent ion, N_i. We derive the column densities for all Si and S ions visible in our spectra from (paper I, Eq. 11)

$$N_i = \frac{m_e c^2 W_\lambda}{\pi e^2 f_{ij} \lambda_0^2} = \frac{9.11 \times 10^{15}\,\mathrm{cm}^{-2}}{f_{ij}} \frac{W_E}{\mathrm{eV}}, \tag{5.1}$$

where W_λ and W_E are the equivalent width in wavelength and in energy space, respectively, and where f_{ij} is the oscillator strength, taken here as the sum of all transitions blending into the absorption line of the respective ion. We use the compilation of Verner et al. (1996b) for H-like ions, and the compilation of Palmeri et al. (2008) for He-like ions and XSTAR (Kallman & Bautista, 2001) calculations that take Auger damping into account for all other ionization stages. All other symbols have their usual meanings.

Summing the column densities for all ions of an element then yields a lower limit for the element's total column density. For comparison with the continuum fitting values, the abundance of the element can then be utilized to convert this column density into a corresponding N_H-value. The values listed in Tables 5.6 and 5.7 list two N_H-values. One value is based on the solar abundances as summarized by Wilms et al. (2000). In our second conversion we consider that in their analysis of the optical spectrum of HDE 226868 Herrero et al. (1995) found that helium is overabundant by a factor of 2.53 with respect to the solar value. Assuming that metals scale with the same factor as helium with respect to hydrogen, we scale the

solar abundances of Wilms et al. (2000) by this factor and use these corrected abundances to derive the corresponding hydrogen column.

Figure 5.7 shows how the single ion column densities vary with depth of the dip. As we enter the dip, for the lowest ionization states (Fig. 5.7, lower panels) the columns increase towards the deepest dip stages. This trend reverses for the highest ionization states (Fig. 5.7, upper panels). This behavior, too, is indicative of an absorber with a layered ionization structure, i.e., a medium whose outer regions are more highly ionized than the central core region.

For the non-dip data, column densities of H-like and He-like silicon have already been presented in paper I. Despite the fact that our dip selection criterion for the non-dip data has not changed, there is a slight difference in the equivalent width determined for He-like Si XIII, where paper I finds an equivalent width of -1.73 eV, while we find -1.92 eV, resulting in a $\sim$10% difference in the column. Both values are still in agreement within their uncertainties. The difference in equivalent width for H-like Si XIV, on the other hand, is a surprising factor 1.3. A possible explanation is that the non-dip data allowed a global fit, including interstellar absorption, more than a hundred lines, and a pileup correction. The three dip stages, however, do not have enough signal to constrain such a model, and consequently for consistency we also model the non-dip data with local fits. Differences at the 15% level would therefore be expected due to these different analysis approaches. Taking into account these additional 15%, the H-like Si XIV columns, too, are consistent within their uncertainties.

Figure 5.8 shows the column densities as a function of the ionization potential of the respective ions. The closed shell ions He-like Si XIII and S XV exhibit enhanced column densities as expected. However, whereas the appearance of lower ionization stages in the strong dip points to a lower temperature in the core of a clump, it is also possible that we see a constant temperature clump with a higher density in its core: As the absorber is ionized, the column density measured from continuum absorption is only a lower limit; we cannot see the fully ionized material. The figure also clearly illustrates the large column of the hydrogenic lines. It is therefore very likely that a significant amount of the S and Si in the system are fully ionized and thus cannot be detected.

Doppler shifts

To analyze the morphology of the absorbing material, we next take a look at the bulk motion, measuring the Doppler shifts of the lines in the Si and S regions for each dipping stage. Since the uncertainty of the theoretical rest-wavelengths is on the order of the expected line shifts (Hell et al., 2013), we measured the centroids of the line blends for each ion in the laboratory, using an electron beam ion trap and a microcalorimeter (Hell et al., 2016). For the shifts of the He- and H-like 1s $\rightarrow$ 2p transitions, we use the tables of Drake (1988) and Garcia & Mack (1965), respectively, as reference. These are the same reference publications that we also used for the calibration of the laboratory data.

Figure 5.9 shows the resulting velocities for each line in the different dipping stages of each observation. Overall, for the same spectral lines the Doppler shifts are consistent throughout the different dipping stages. This is more obvious for the uncontaminated lines in the Si spectra, where statistics are much better than for the S lines and line centers can be determined more accurately. The O-like S IX line detected in ObsID 9847 is the only outlier. As the width of this line is narrow (only one energy bin), and since we only claim a tentative

Table 5.6: Column densities as calculated from the silicon line equivalent widths.

		$N_{\text{H-like}}$	$N_{\text{He-like}}$	$N_{\text{Li-like}}$	$N_{\text{Be-like}}$	$N_{\text{B-like}}$	$N_{\text{C-like}}$	$N_{\text{N-like}}$	$N_{\text{O-like}}$	N_{Si}	$N_{\text{H,Wilms}}$	$N^{\dagger}_{\text{H,Herrero}}$
						$[10^{15}\,\text{cm}^{-2}]$				$[10^{15}\,\text{cm}^{-2}]$	$[10^{21}\,\text{cm}^{-2}]$	$[10^{21}\,\text{cm}^{-2}]$
3814	nondip	$54.6^{+3.0}_{-3.1}$	21.6 ± 1.6	2.6 ± 0.9	0.84 ± 0.22	0.49 ± 0.16	0.28 ± 0.13	–	–	80 ± 7	2.27 ± 0.20	0.90 ± 0.08
	weak dip	53 ± 7	22 ± 4	$3.8^{+5.1}_{-2.0}$	1.6 ± 0.5	$1.31^{+0.29}_{-0.30}$	1.10 ± 0.24	1.4 ± 0.5	–	84 ± 15	2.4 ± 0.5	0.94 ± 0.18
	dip	52 ± 7	24 ± 4	3.6 ± 1.9	1.3 ± 0.5	2.04 ± 0.28	$1.76^{+0.23}_{-0.24}$	1.8 ± 0.5	–	87 ± 15	2.5 ± 0.5	0.97 ± 0.16
	strong dip	36 ± 8	13 ± 4	$4.4^{+3.0}_{-2.4}$	3.2 ± 0.5	3.26 ± 0.30	$2.42^{+0.26}_{-0.27}$	3.3 ± 0.5	1.6 ± 1.1	68 ± 18	1.9 ± 0.6	0.76 ± 0.20
8525	nondip	57 ± 7	23 ± 4	7.5 ± 1.8	1.3 ± 0.5	1.28 ± 0.29	0.65 ± 0.25	–	–	91 ± 15	2.6 ± 0.4	1.01 ± 0.16
	weak dip	59 ± 7	24 ± 4	$10.4^{+2.0}_{-2.1}$	2.8 ± 0.5	$2.85^{+0.27}_{-0.28}$	1.07 ± 0.26	–	–	100 ± 15	2.8 ± 0.5	1.12 ± 0.17
	dip	68 ± 7	30 ± 4	$11.9^{+1.9}_{-1.8}$	3.3 ± 0.5	3.60 ± 0.25	1.89 ± 0.24	0.9 ± 0.5	–	119 ± 15	3.4 ± 0.5	1.33 ± 0.16
	strong dip	49 ± 8	14 ± 5	9.8 ± 2.3	2.5 ± 0.6	3.3 ± 0.4	3.04 ± 0.26	3.0 ± 0.6	1.7 ± 1.2	86 ± 19	2.4 ± 0.6	0.96 ± 0.21
9847	nondip	52 ± 6	18 ± 4	7.5 ± 1.8	2.2 ± 0.4	1.06 ± 0.28	–	–	–	80 ± 14	2.3 ± 0.4	0.89 ± 0.16
	weak dip	43 ± 9	21 ± 5	8.8 ± 2.4	3.1 ± 0.5	2.0 ± 0.4	1.2 ± 0.4	–	–	79 ± 20	2.2 ± 0.6	0.88 ± 0.22
	dip	52 ± 8	20 ± 5	8.6 ± 2.3	3.2 ± 0.5	$3.22^{+0.29}_{-0.30}$	1.51 ± 0.30	–	–	89 ± 19	2.5 ± 0.6	1.00 ± 0.21
	strong dip	30 ± 10	–	8.7 ± 2.6	3.7 ± 0.6	$4.47^{+0.30}_{-0.31}$	3.51 ± 0.27	3.3 ± 0.6	–	54 ± 20	1.5 ± 0.6	0.60 ± 0.22

† Herrero et al. (1995) provide a scaling factor for the observed overabundance of helium, which we apply to the solar abundances of Wilms et al. (2000); See text for further details.

Table 5.7: Column densities as calculated from the sulfur line equivalent widths.

		$N_{\text{H-like}}$	$N_{\text{He-like}}$	$N_{\text{Li-like}}$	$N_{\text{Be-like}}$	$N_{\text{B-like}}$	$N_{\text{C-like}}$	$N_{\text{N-like}}$	$N_{\text{O-like}}$	N_{S}	$N_{\text{H,Wilms}}$	$N^{\dagger}_{\text{H,Herrero}}$
		$[10^{15}\,\text{cm}^{-2}]$								$[10^{15}\,\text{cm}^{-2}]$	$[10^{21}\,\text{cm}^{-2}]$	$[10^{21}\,\text{cm}^{-2}]$
3814	nondip	47 ± 8	18 ± 4	2.8 ± 2.0	0.9 ± 0.6	0.7 ± 0.4	1.1 ± 0.4	–	–	71 ± 18	2.0 ± 0.5	0.79 ± 0.20
	weak dip	43 ± 17	20 ± 8	6 ± 4	–	1.3 ± 0.8	1.1 ± 0.8	2.1 ± 1.2	–	70 ± 40	2.1 ± 1.1	0.8 ± 0.5
	dip	64 ± 14	30 ± 7	7 ± 4	2.2 ± 1.2	1.9 ± 0.8	2.5 ± 0.7	2.5 ± 1.2	–	110 ± 40	3.1 ± 0.9	1.2 ± 0.4
	strong dip	36 ± 15	8 ± 8	–	1.6 ± 1.2	2.6 ± 0.8	3.4 ± 0.7	2.3 ± 1.3	–	50 ± 40	1.5 ± 1.0	0.6 ± 0.4
8525	nondip	55 ± 16	33 ± 7	–	1.6 ± 1.2	1.7 ± 0.8	1.7 ± 0.7	–	–	90 ± 40	2.6 ± 1.0	1.0 ± 0.4
	weak dip	68 ± 17	26 ± 8	7 ± 4	2.2 ± 1.2	3.8 ± 0.8	1.9 ± 0.7	–	–	110 ± 40	3.1 ± 1.1	1.2 ± 0.5
	dip	53 ± 16	24 ± 8	11 ± 4	2.7 ± 1.2	3.2 ± 0.8	3.0 ± 0.6	2.9 ± 1.2	–	100 ± 40	2.8 ± 1.1	1.1 ± 0.5
	strong dip	40^{+16}_{-17}	21 ± 8	–	–	1.7 ± 0.8	2.7 ± 0.7	3.9 ± 1.2	–	70 ± 40	2.0 ± 1.1	0.8 ± 0.4
9847	nondip	56 ± 14	14 ± 8	–	1.5 ± 1.1	1.0 ± 0.8	1.1 ± 0.6	–	–	70 ± 40	2.1 ± 0.9	0.8 ± 0.4
	weak dip	–	33 ± 9	–	3.3 ± 1.4	3.3 ± 0.9	2.4 ± 0.8	–	–	42 ± 19	1.2 ± 0.6	0.47 ± 0.20
	dip	51^{+18}_{-19}	19^{+9}_{-10}	–	3.8 ± 1.3	3.2 ± 0.9	3.6 ± 0.7	3.6 ± 1.3	–	80 ± 50	2.4 ± 1.2	0.9 ± 0.5
	strong dip	42 ± 19	11 ± 10	5 ± 5	3.8 ± 1.4	4.6 ± 0.9	3.5 ± 0.8	4.4 ± 1.4	$4.0^{+2.8}_{-2.9}$	80 ± 50	2.2 ± 1.3	0.9 ± 0.5

† Herrero et al. (1995) provide a scaling factor for the observed overabundance of helium, which we apply to the solar abundances of Wilms et al. (2000); See text for further details.

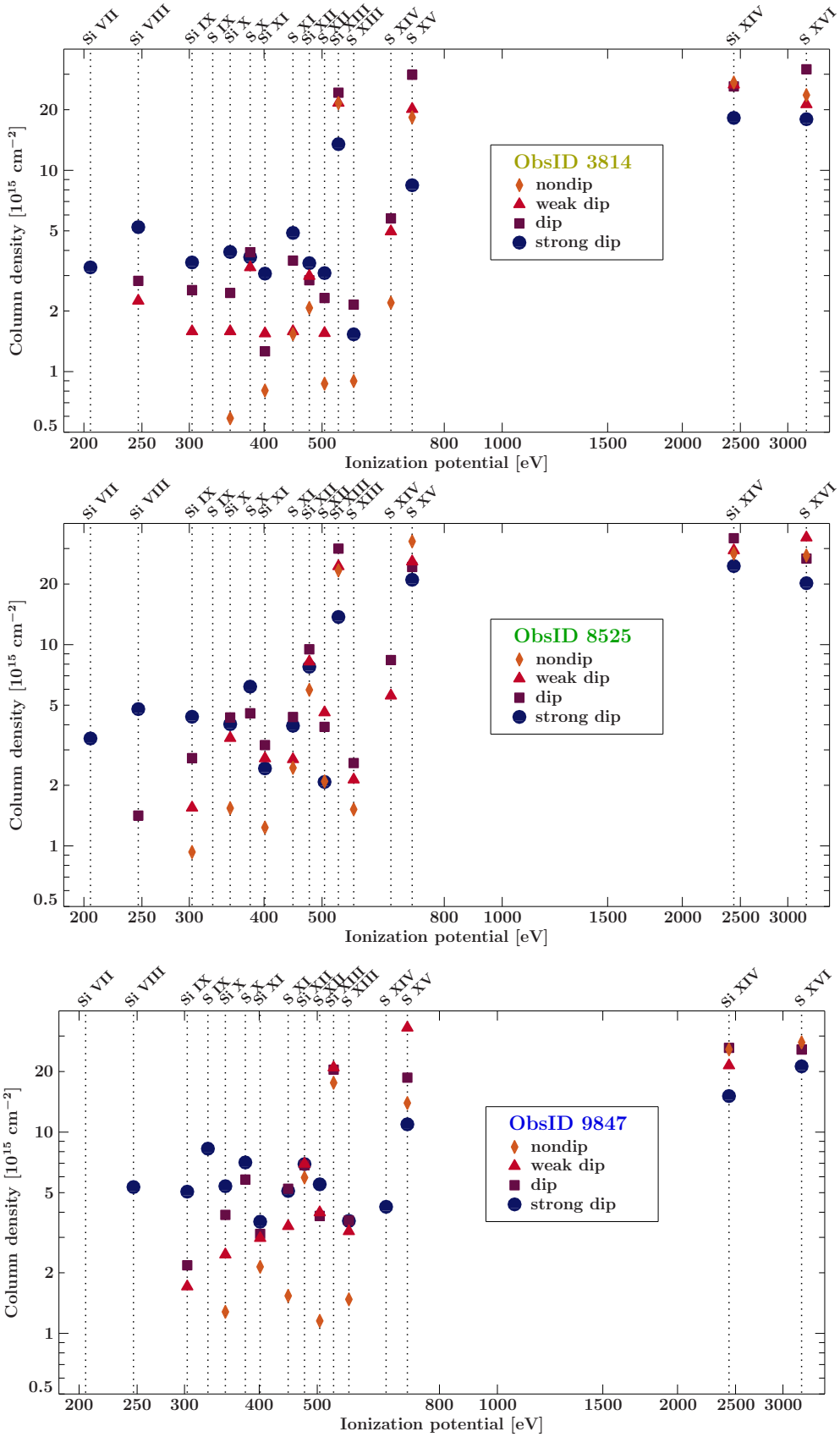

Figure 5.8: Column densities versus ionization potential for the respective silicon and sulfur ions in all dip stages.

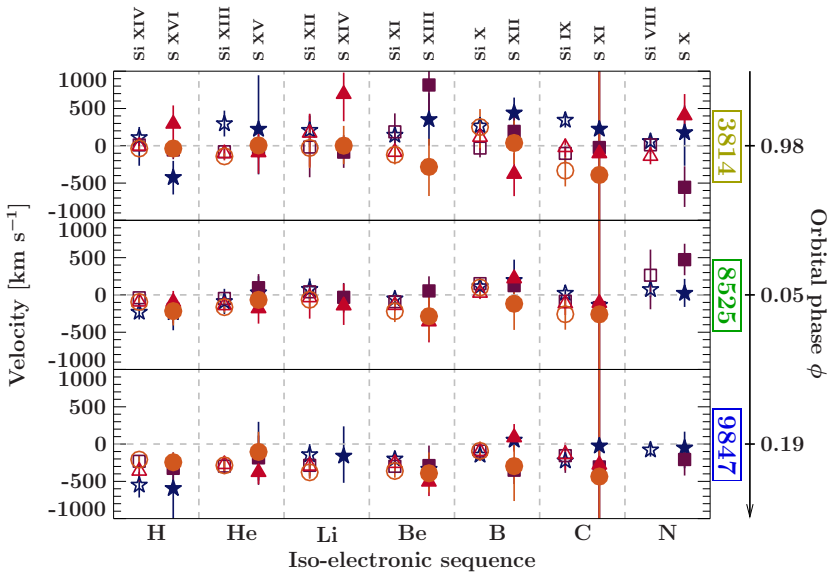

Figure 5.9: Doppler velocities for the various ionization states of Si VIII – Si XIV (empty) and S X – S XVI (filled) in all dipping stages (non-dip: orange circles, weak-dip: red triangles, dip: violet squares, strong-dip: blue stars) over all observations in the different orbital phases.

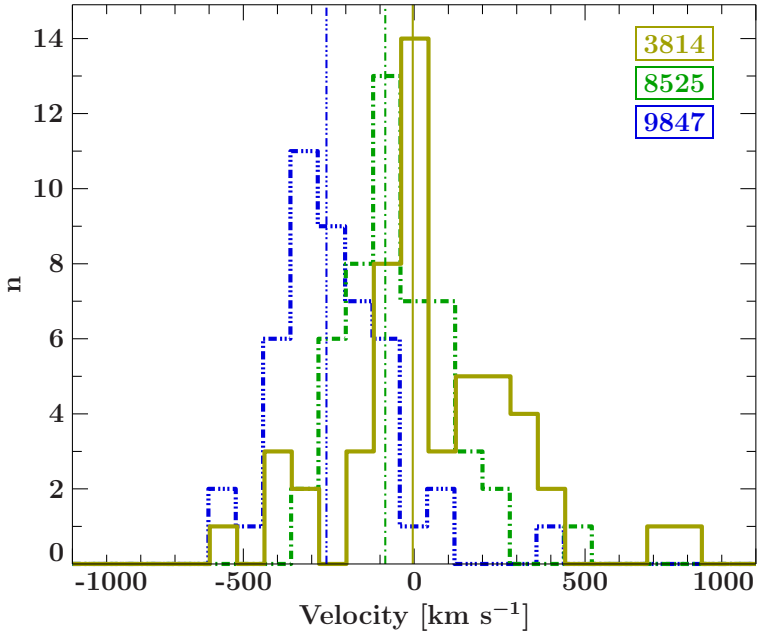

Figure 5.10: Distribution of velocity shifts of all Si and S lines detected in the three ObsIDs with their medians. The peak velocity clearly shifts between the observations.

detection of this line (see Sect. 5.2.2), the derived Doppler velocity is probably inaccurate and we do not include the line in Fig. 5.9.

Figure 5.10 shows the distribution of the Doppler shifts in the three observations. For ObsID 3814, the velocities scatter around 0 km s^{-1}. For ObsID 8525, the velocities increase toward negative values and scatter around −60 km s^{-1}, and for ObsID 9847, the scatter moves down to around −230 km s^{-1}.

This Doppler shift cannot be due to the free fall velocity of donor material onto the black hole: As we are looking at the system near $\phi_{\mathrm{orb}} = 0$, the free fall velocity would cause a redshift, not a blue-shift of lines as seen in the spectra. The Keplerian velocity of the black hole also cannot be the cause for the energy shift, as we would expect the maximum amplitude of the shift to be of the order of 100 km s^{-1} and not much larger than that (the projected

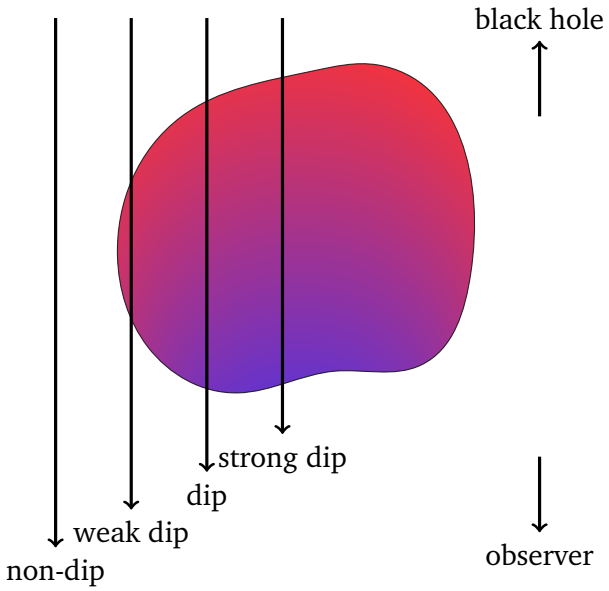

Figure 5.11: Sketch of a clump passing our line of sight and causing the different dip stages. Red color indicates more highly ionized regions, blue color regions with lower ionization balance.

semi-amplitude of the black hole is $K_{BH} \sim 91\,\mathrm{km\,s^{-1}}$, e.g., Brocksopp et al., 1999; Gies et al., 2003; Orosz et al., 2011).

A clumpy absorber

The consistency of the Doppler shifts of the lines during dipping provides evidence for inhomogeneities in the absorber which are forming a unified structure that has some kind of density stratification. We will call these structures "clumps", even though we do not want to imply that the structures are static phenomena as opposed to transient structures. Either due to self shielding, or because the material is in some kind of approximate pressure equilibrium similar to the clouds in active galaxies (Krolik et al., 1981), the part of the clump facing away from the black hole will be less ionized. As the clump moves through the line of sight (Fig. 5.11), we first look through its outer, more ionized regions. We only see the lower ionization stages during the deeper dip where the middle of the clump is located in our line of sight.

Regarding the orbital phase dependency, already from the three ObsIDs analyzed here one can see a trend towards higher Doppler velocities further away from $\phi_{\mathrm{orb}} \sim 0$. This is consistent with paper II. Figure 5.12 shows the median, mean, first, and third quartile of the velocity distribution of the Si and S lines in comparison to the nondip results shown in Fig. 11 of paper II. The phase dependence of the Doppler shifts measured within the dips as well as the amplitude are roughly consistent with paper II. The material producing the dips thus seems to be at the same distance from the black hole as what can be seen during nondip.

The projected wind velocities in this figure are calculated using a CAK-model with a focused wind based on Gies & Bolton (1986b, see paper II for more details[7]). The model consists of a radially symmetric wind that is focused onto the black hole in a cone of 20°. Gies & Bolton (1986b) state that their model is valid only out to $0.9\,d$, where d is the distance between

[7]Note that there was a sign error in the code that produced the figure in paper II. This led to a flip of sign for the velocity curves as well as a slight phase shift. These changes do not have an influence on the interpretation of the figure in paper II. Figure 5.12 shows the corrected velocity curves.

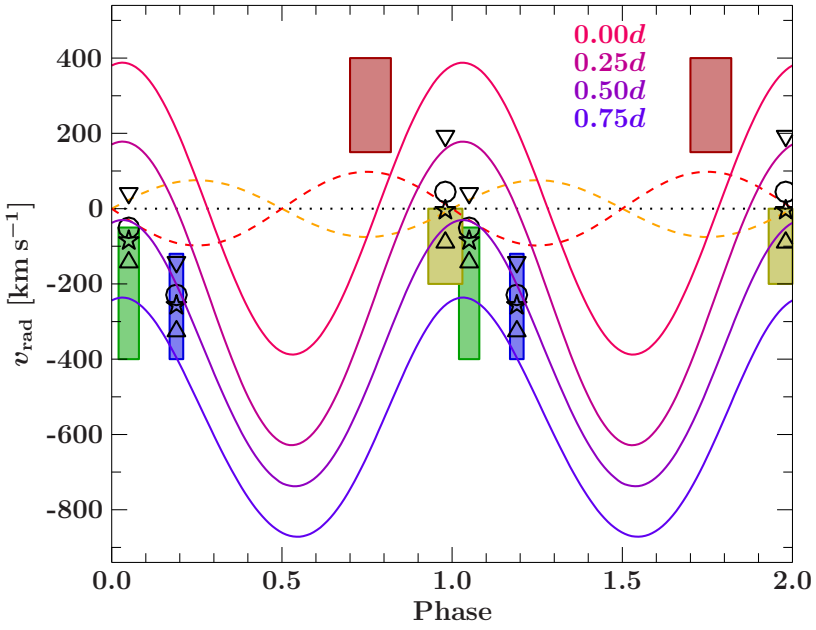

Figure 5.12: Radial velocities of the black hole (red dashed line) and the companion (orange dashed line), and wind velocities projected onto the line of sight as a function of distance from the black hole. Distances are given in units of the distance between the black hole and its donor, d. Colored boxes indicate the range of measured nondip Doppler shifts from the *Chandra* observations (red: ObsID 3815, yellow: ObsID 3814, green: ObsID 8525, blue: ObsID 9847, modified and corrected from paper II, Fig. 11). Symbols show the median (star), mean (circle), first (point-up triangle) and third quartile (point-down triangle) of the distribution of Doppler shifts for the Si and S lines.

the star and the black hole, as the density at this distance is already too small to produce a significant contribution to the absorption line profiles. One might argue if this is only the case for a smooth wind, and clumps have to be treated differently. Even for $\phi_{\rm orb} = 0$ the regions we are interested in (distances of 0–0.75 d from the black hole, in the direction of the line of sight at different phases) are mostly outside of the valid region of the model of Gies & Bolton (1986b), but as our observations are near $\phi_{\rm orb} = 0$, where the distance to the star is not much more than 0.9 d, we still take the model for a rough estimate. However, both measured nondip and dip Doppler shifts fit neither the projected wind velocity (difference in phase) nor the black hole (difference in amplitude). Thus, we cannot make an exact statement on the location of the clumps in the system from our data, though a comparison of the amplitude implies a distance of less than 0.25 d from the black hole.

In order to investigate the origin of the observed ionization, we use XSTAR (Kallman & Bautista, 2001), which models the photo-ionization structure of spherically symmetric gas clouds which are irradiated by a central source of arbitrary spectral energy distribution[8]. We assume gas clouds of solar chemical composition (Grevesse et al., 1996) with a covering fraction of 100%, temperature of 10^6 K, a constant total hydrogen particle density of $n = 10^{10}\,\mathrm{cm}^{-3}$, and an incident 1–1000 Ry luminosity of $L = 1.4 \times 10^{37}\,\mathrm{erg\,s}^{-1}$. In this configuration, the definition of the ionization parameter is $\xi = L/\left(nR^2\right)$, where R the inner radius of the shell. Our incident spectral energy density (SED) is adapted from Pepe et al. (2015). In order to gauge the influence of the strong UV photon field of the donor star, we perform

[8]The XSTAR simulations were performed by Ralf Ballhausen, priv.comm.

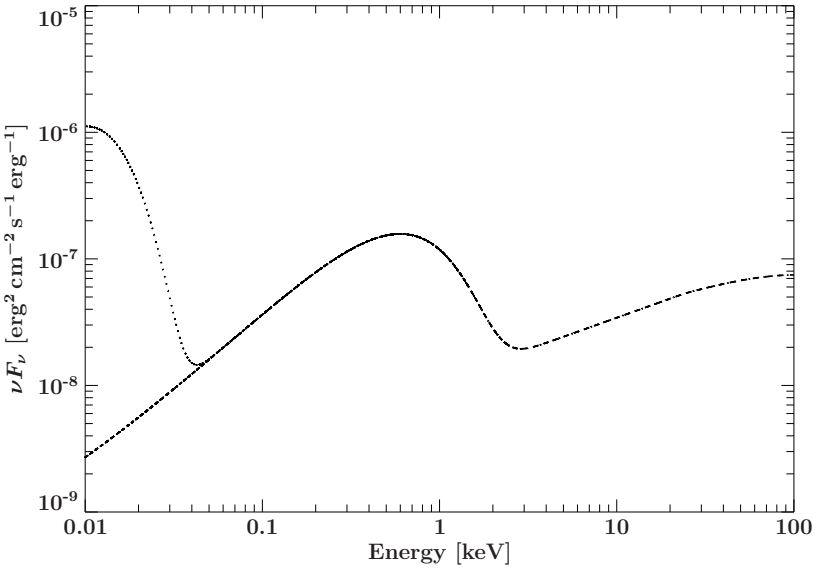

Figure 5.13: Incident SED used for the XSTAR simulations. The dotted and dashed lines show the SED with and without the optical companion star, respectively. Note that the SED is always re-normalized to the assumed model luminosity.

simulations with and without a stellar contribution to the total SED (see Fig. 5.13).

We calculate model grids by varying ξ and the total hydrogen column, $N_{\rm H} = n\ell$, where ℓ is the geometric size of the cloud. Since L and n are fixed, this approach effectively models photoionized clouds of varying size and distance from the source of ionizing photons. To compare these models with the observations, for all observed ions we then determine contours in the $\log\xi$-$N_{\rm H}$-plane where the theoretical column of the ion equals the measured one. Figure 5.14 shows the results for Si and S. We note that the inclusion of the optical companion has only a marginal effect on the observed ion column densities of Si and S (Fig. 5.14c and d). This is important because the binary geometry of the system with two sources of radiation cannot be accounted for by the XSTAR simulation. Neglecting the optical companion will therefore only introduce a small systematic effect on ionization structure modeling of these ions.

In the ideal case of a simple medium of constant density and temperature, all of these contours would intersect in a single point, modulo measurement errors, which are, however, small compared to the large dynamic range shown in Figure 5.14. In practice, assuming that the dip is produced by a single absorbing cloud, we would expect some kind of a density variation in the cloud, as discussed above. We can use our simple XSTAR simulations to identify regions of particular interest. From Fig. 5.14, columns of moderately ionized ions can be roughly reproduced with hydrogen column densities around $3\times10^{20}\,{\rm cm}^{-2}$ and ionization parameters of $\log\xi\sim$1–2. The high ionization states of silicon and sulfur, on the other hand, require column densities and an ionization parameter which are roughly an order of magnitude higher. This result points at a more complex origin for the ionization structure than photoionization alone. One possible explanation would be ionization due the strong shocks that are present in radiation hydrodynamical models for massive X-ray binary systems (Blondin et al., 1990, 1991; Blondin, 1994; Manousakis & Walter, 2011; Manousakis & Walter, 2015, and references therein) as well as in winds from early type stars (Owocki et al., 1988; Sundqvist & Owocki, 2013, and references therein).

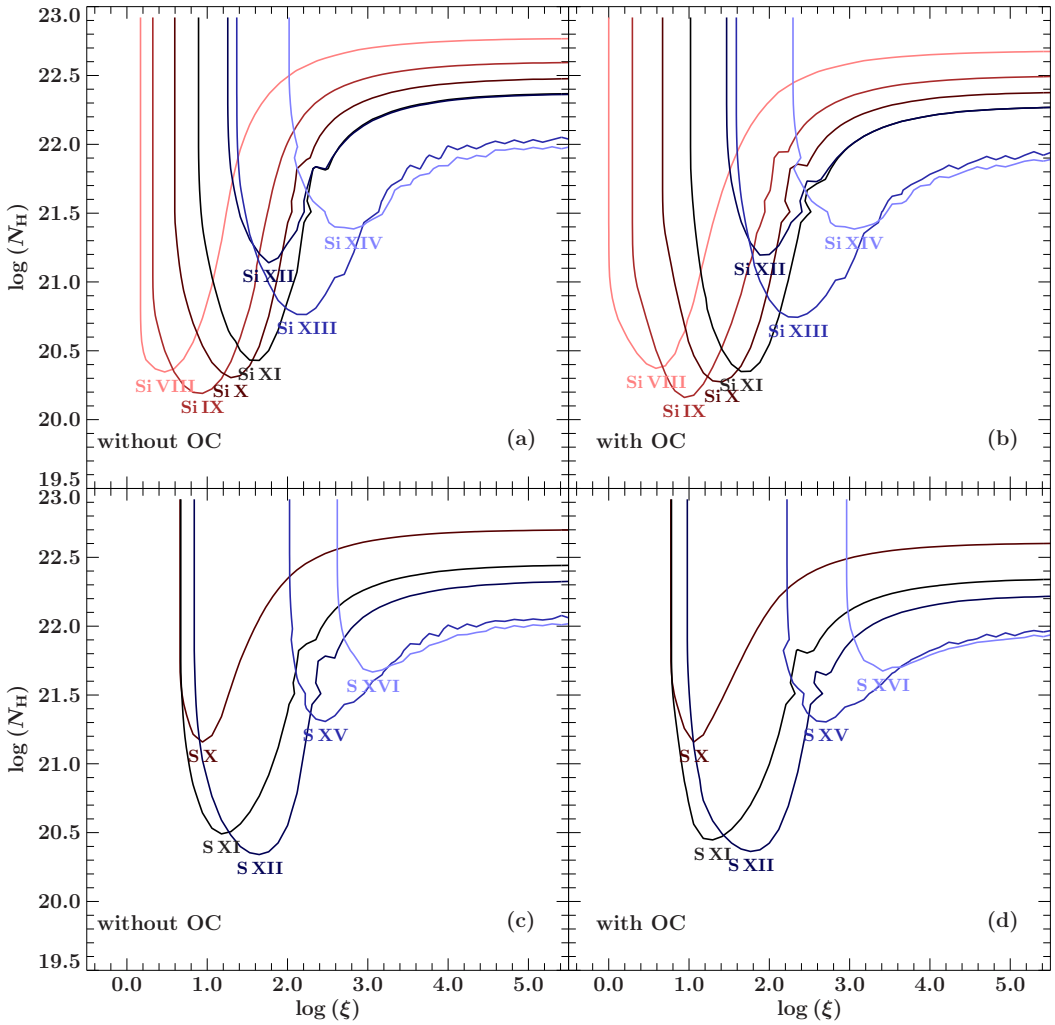

Figure 5.14: Contours of the measured ion columns in the N_H-log(ξ)-map. Color-coded are the different ionization states. Panels (a) and (b) show the silicon columns for an incident SED with and without the optical companion, respectively. Panels (c) and (d) show the same comparison of the effect of the incident SED for sulfur.

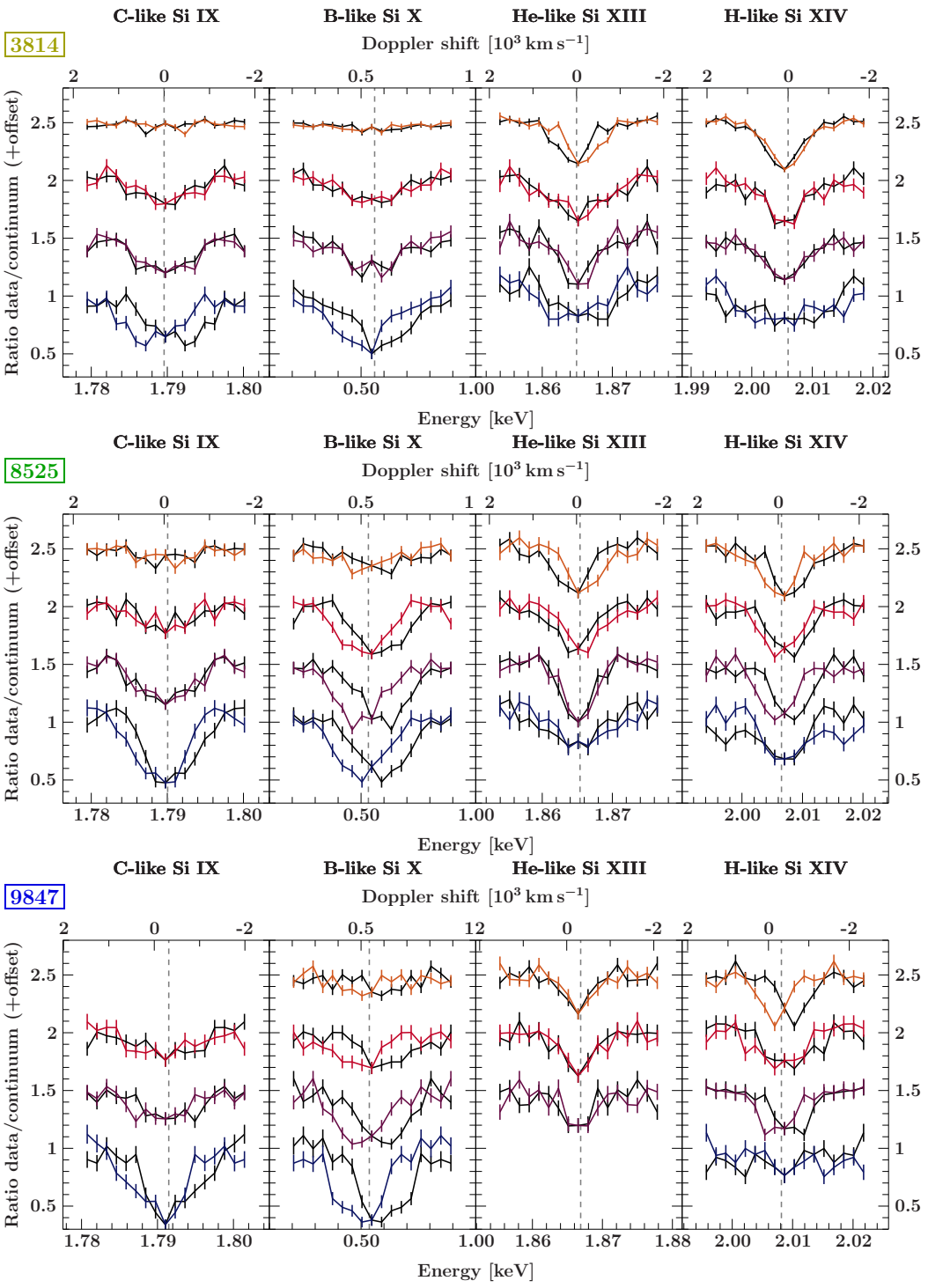

Figure 5.15: Original line profiles (colored) for the nondip (top, orange), weak dip (second from top, red), dip (third from top, purple) and strong dip (bottom, blue) Si lines for selected ions, as well as the same data flipped (black, see also text for further information) at the energy corresponding to adding a constant Doppler shift for each observation (grey dashed line) to the line's laboratory energy. For an ideal, symmetric line, the colored and black curves should match. Most of the lines observed here have complex line profiles.

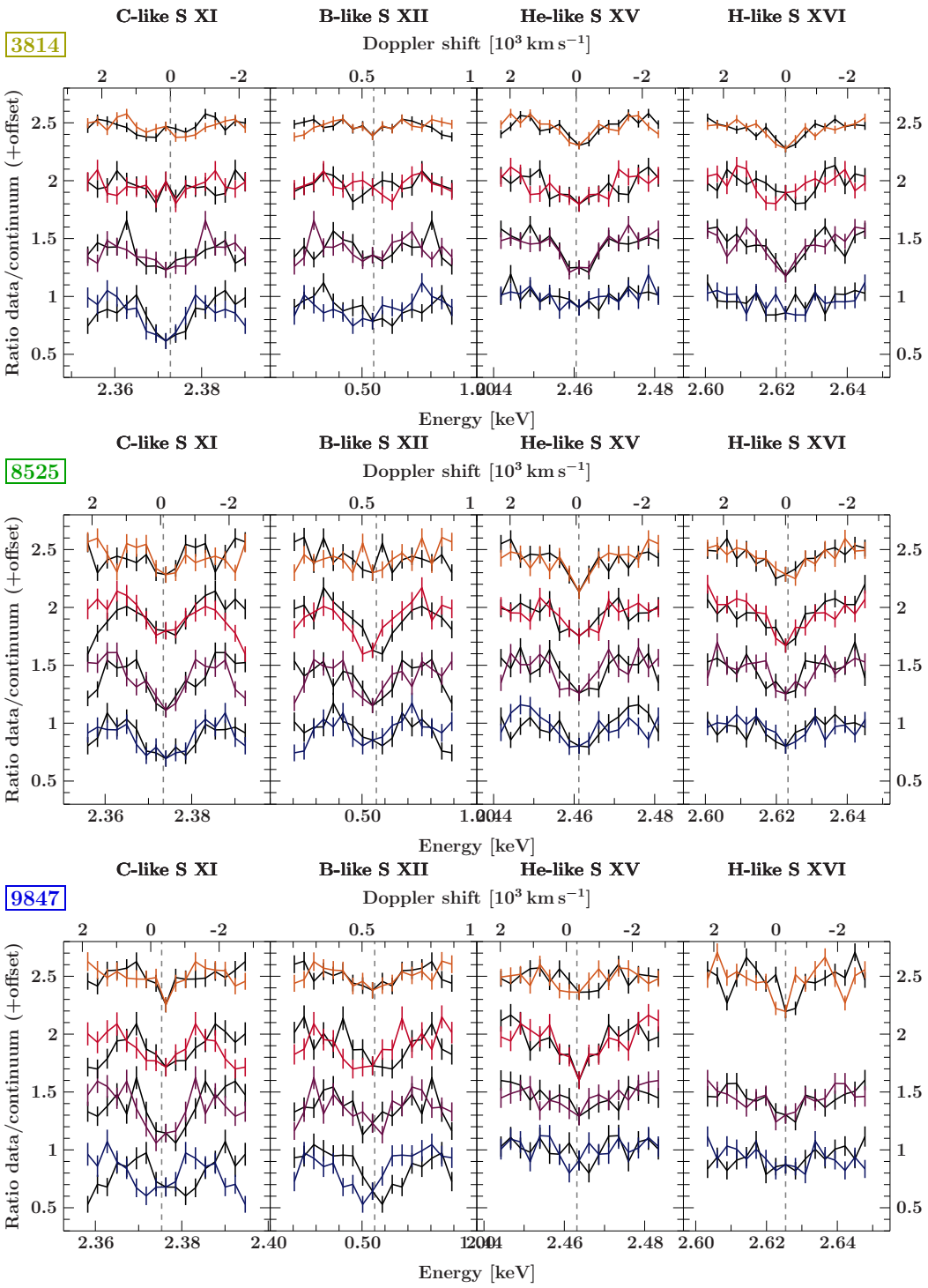

Figure 5.15: (Continued) Original line profiles (colored) for the nondip (top, orange), weak dip (second from top, red), dip (third from top, purple) and strong dip (bottom, blue) S lines for selected ions, as well as the same data flipped (black, see also text for further information) at the energy corresponding to adding a constant Doppler shift for each observation (grey dashed line) to the line's laboratory energy. For an ideal, symmetric line, the colored and black curves should match. Most of the lines observed here have complex line profiles.

Line symmetry

Although the detailed analysis of the complex photoionization line profiles observed in Cyg X-1 is beyond the scope of this paper, we can at least take a quantitative look at the line shapes in the region of ±8 bins around the respective rest energy, adjusted for the most probable Doppler shift for each ObsID (3814: 0 $\mathrm{km\,s^{-1}}$, 8525: $-80\,\mathrm{km\,s^{-1}}$, 9847: $-320\,\mathrm{km\,s^{-1}}$; see also Fig. 5.10). Figure 5.15 shows the original data (colored) and the same data flipped (black) around the center of the bin containing the adjusted rest energy (grey dashed line). For a symmetric line shape, the original and flipped data should match, as is the case, e.g., for 8525 He-like Si XIII in the dip data, or 3814 H-like Si XIV nondip, weak dip and dip data. However, often we see the lines shifted by one or even two bins (e.g., 3814 C-like Si IX strong dip or 9847 B-like S XII weak dip, dip and strong dip). There are also signs of asymmetry (e.g., 9847 C-like Si IX strong dip or 3814 C-like S XI dip), as well as lines that show both asymmetry and a shift (e.g., 3814 C-like Si IX strong dip or 8525 B-like Si X nondip and dip).

Clear P Cygni-like profiles for Cyg X-1 were reported only at $\phi_{\mathrm{orb}} = 0.5$ during ObsID 11044 (Miškovičová et al., 2011). Schulz et al. (2002b) also found indications of P Cygni profiles at $\phi_{\mathrm{orb}} = 0.74$. In the UV, P Cygni profiles were found by Vrtilek et al. (2008), also at $\phi_{\mathrm{orb}} = 0.5$, where the stellar wind is focused towards the observer by the black hole. At around $\phi_{\mathrm{orb}} = 0$, asymmetries are expected as well as the focused wind is moving away from the observer towards the black hole and the redshift and ionization are highest. This was observed, e.g., by Feng et al. (2003) and discussed in paper II. Our observations fit in this picture.

Emission in the deepest dips

While the absorption lines discussed so far show a clear dependency on the depth of the dip, this is not the case for the He-like Si XIII z emission line, with its total line flux being constant throughout the dip stages. This result could either indicate that the emitting material originates in a geometrically much larger region than the absorber, such that the emission line is not affected by the absorber, or, alternatively, that the emission line originates in an area where the line of sight does not pass through the absorber.

A possible origin for the Si XIII emission line could be the photoionization region in the stellar wind which surrounds the X-ray emission region. As discussed in paper I, the Strömgren sphere around the X-ray source is comparable in size to the separation of the black hole and its donor star, i.e., it is much larger than the absorbing cloud. Given the low optical depth of this region we expect a region whose X-ray emission is dominated by emission lines, similar to that seen, e.g., in Vela X-1 (Schulz et al., 2002a; Watanabe et al., 2006; Grinberg et al., 2017) or in Cen X-3 (Wojdowski et al., 2003). The flux from the photoionization region, however, is much fainter than the X-rays from the accretion flow. The region has therefore been mainly studied in edge-on systems, in which during eclipses our line of sight onto the bright X-ray source is blocked by the donor star. While the Cyg X-1/HDE 226868 system does not show eclipses, we can utilize the strong dipping to at least partially block the line of sight to the black hole. The best opportunity for this is presented by the long, deep dip at the beginning ObsID 8525, which is the most pronounced of all the dips in our observations. The deep part of this dip (according to our dip stage identification, i.e., the blue data points in Fig. 5.2 belonging to that dip) lasted for 5.3 ks (1.5 hours), which is long enough to accumulate a decent gratings spectrum of one single dip. Because of the strong absorption, pileup is no concern in the resulting spectrum and the HEG and MEG spectra

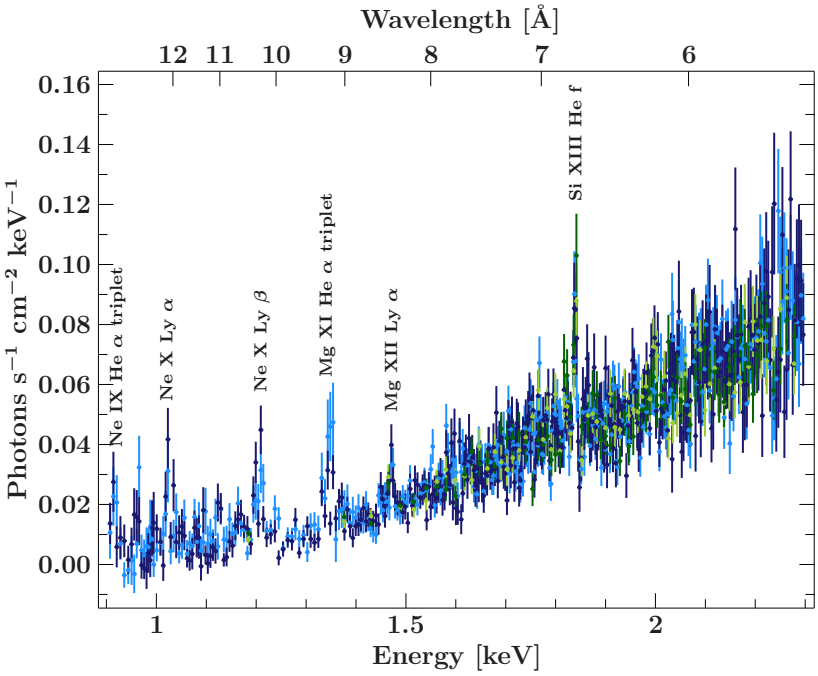

Figure 5.16: "Deep dip" spectrum from ObsID 8525 from a subset of the 'strong dip' data in the 0.9–2.3 keV (13.8–5.4 Å) range, with the data rebinned to $S/N \geq 5$, revealing emission lines from the photoionized zone around the black hole.

agree with each other.

As shown in Figure 5.16, during the deepest parts of the dip in ObsID 8525, the photoionized zone around the black hole indeed dominates the spectrum, resulting in the presence of emission lines. Already noted by (Hanke, 2011), the most prominent lines detected are Si XIII He z (1.8394 keV ≡ 6.7405 Å, Porquet et al., 2010), Mg Ly α (1.4723 keV ≡ 8.4211 Å), the Mg He α triplet (∼1.3522 keV ≡ 9.1691 Å), as well as Ne Ly β (1.2109 keV ≡ 10.2390 Å), Ne Ly α (1.0280 keV ≡ 12.0601 Å) and the Ne IX He α triplet (∼0.9220 keV ≡ 13.4473 Å). Unfortunately, however, the signal to noise in the lines is too low to allow a further characterization of their parameters.

5.2.3 Implications and outlook

Our analysis gives us a glimpse at the properties of the structures causing the dips. From the light curve, we can constrain the duration of a dip, and thus of a passage of the clump through our line of sight, to 0.5 ks for the shorter dips up to 5 ks for the longer dips. This assumption is only valid if a dip is caused by a single, bigger clump with a cold or dense core instead of many small clumps in the line of sight.

Assuming a distance of $0.25\,d$ between the clump and the black hole (d being the distance between black hole and donor, see Sect. 5.2.2), a simple Keplerian approach (i.e., the clump orbiting the black hole) gives a velocity of ∼460 km s^{-1} perpendicular to the line of sight. From the velocity of the clump and the duration of the dip, we can estimate the diameter of the clumps to $(2.3 \ldots 23) \times 10^8$ m, equivalent to $(0.33 \ldots 3.3)\,R_\odot$ or $(0.02 \ldots 0.2)\,R_*$. As an advancing clump grows in size (Sundqvist et al., 2012), we can calculate its ejection size (Grinberg et al., 2015) to about a third of the size that we measure at the distance of $0.25\,d$.

With the current data we can only speculate whether this picture of single, big clumps is the

correct one. The morphology of the light curve in ObsID 8525 supports this idea, whereas ObsID 3814 with its rapid variability appears to be more in favor of a large number of small clumps in our line of sight. For a sufficiently high number of smaller clumps, the ones closer to the black hole are partly shielding the outer ones from the ionizing radiation, which is in agreement with our observation of lower ionization stages during strong dipping. A possible explanation would then be a mixture of some larger clumps causing the distinct dips in the light curve, and many smaller clumps.

This idea is consistent with the picture of structured, radiation pressure driven O-star winds (Castor et al., 1975). As shown, e.g., by Owocki & Rybicki (1984), the stationary solution for a line-driven wind is unstable. These instabilities grow quickly and result in strong shocks. Hanke (2011) already wrote that "non-stationary hydrodynamic simulations show that dense cool shells of gas form already in deep wind regions close to the photosphere of the O-star (Feldmeier et al., 1997; Dessart & Owocki, 2003; Oskinova et al., 2012; Sundqvist et al., 2018). Large density, velocity, and temperature variations due to the de-shadowing instability further compress the gas in these shells and fragment them into "clumps"." Theory predicts thus that the wind is actually a two phase medium consisting of tenuous, hot gas (covering most of the volume), and embedded cool, dense clumps (containing most of the mass). Observational evidence for this clumping has been found for isolated O-type supergiants (Eversberg et al., 1998; Markova et al., 2005; Bouret et al., 2005; Fullerton et al., 2006; Oskinova et al., 2006), but also for high mass X-ray binaries (e.g., Torrejón et al., 2015).

Speculatively, the picture of the dip behavior would then be that observations at phase 0, which sample the region of the stellar wind closer to the donor star, should show a wide spectrum of clump sizes. Observations at phase 0.75 sample regions that are farther away from the wind, where the clump size distribution has changed, probably favoring larger clumps, resulting in less short term N_{H} variation. Clearly, however, using only three observations from different orbits as well as the need to perform joint spectroscopy of multiple dips do not give us sufficient statistics to make a firm statement about the distribution and size of the clumps. Our estimates are in agreement with the recent 2D simulation results of Sundqvist et al. (2018), however, who find a typical length scale for clumps of $0.01\mathrm{R}_{*}$ at a distance of two stellar radii from the star. We cannot distinguish between quasi-spherical clumps and, e.g., pancake shaped clumps as proposed by Oskinova et al. (2012) which would have different optical depths for different lines of sight. Sundqvist et al. (2018) even find various different clump shapes co-existing in their simulations. *Athena* with its larger effective area will provide more insight as it will be able to look at single dips (Hirsch et al., 2019).

6

We all place a great deal of reliance
On the theory and practice of science
But the hopeful intentions
Of so many inventions
Can be quite buggered up in appliance.

(Anonymous)

Summary and Conclusions

With the three examples for different kinds of X-ray binaries, it becomes obvious that there still are plenty of open questions around in all areas of X-ray astronomy. This last chapter summarizes the three examples and presents a short outlook on current and future projects that try to tackle the open questions.

Super Soft Sources

White dwarfs accreting mass from their binary companions form a hydrogen burning shell on their surface. Depending on the accretion rate, a steady burning or a burning in flashes is possible. These sources emit a super soft X-ray spectrum while there is no emission in the hard X-rays. A similar behavior is observed for some novae for a short time after their outbursts.

Accreting white dwarfs are considered as possible progenitor systems for type Ia supernovae. Such a supernova explosion is one of the most extreme phenomena known in physics so far. It is thus a question of huge interest to know as much as possible about the systems that find such a violent end.

For various of such systems, temporary periodicities have been observed during their super soft emission time. Depending on the origin of these modulations, they can put constraints on the masses of the white dwarfs, an important parameter for the evolution of a system. Similar to most problems in astrophysics, there simply are not enough observational evidence yet to distinguish between different possible explanations.

GRS 1758−258

The physics behind the state changes in X-ray binaries has been under discussion for decades. Many models have been brought forward, most of which agree with the current observational results. Until now, there is no possibility, however, to distinguish between these different models. The intermediate mass X-ray binary GRS 1758−258 might be a test case for such models: It shows not only the classical state transitions though being a persistent source, but sometimes the soft state evolves into a very dim, almost off phase where GRS 1758−258 is not detectable any more in the hard X-rays.

After years of monitoring the source in the hard state, such a state change happened in 2016. With several ToO observations of *Swift*, the spectral change can be seen clearly, and a blackbody disk component appears. The temperature ranges of a few hundred eV are consistent with earlier results (Soria et al., 2011). Unfortunately, GRS 1758−258 dimmed

and turned off in the hard X-rays during the *INTEGRAL* observation, such that these data cannot be used to put further constraints on the power law photon index, which is anti-correlated to the black body temperature in the fits of the *Swift* XRT data.

In addition to this sometimes unusual soft state behavior, GRS 1758−258 also has special requirements for the accretion disk in a state change model: Already the long *RXTE* monitoring showed an evolving periodicity around 18 days for the source that could be due to a warped accretion disk (Hirsch et al., 2018). The periodicity as well as its evolution was confirmed to be present also in the hard X-rays in the *Swift* BAT light curve. There are indications that a kink in periodicity could be correlated with an almost off soft state, as it is seen in the 2001 as well as the 2016 dim soft state.

The obvious open task here is to collect more observational data, of GRS 1758−258, its timing behavior and its dim, soft states, as well as from other sources, to put constraints on the currently existing models and hopefully fine one that is able to explain the complex physics of this class of sources in all its details.

Cyg X-1

I analyzed three *Chandra*-HETGS observations of the high mass X-ray binary Cyg X-1 around superior conjunction of the system, where the structure of the stellar wind causes absorption features, so-called "dips", in the X-ray light curve. With the help of color-color diagrams, we divide the data into four different dip stages containing a comparable total number of counts. For each dip stage, we fit the silicon and sulfur regions of the spectrum by applying a local powerlaw continuum and Gaussian lines to model the absorption lines for different ionization stages of silicon and sulfur. We find

- lower charge ions appearing in the deeper dip stages,
- equivalent widths / absorption columns rising for deeper dip stages,
- phase dependent Doppler shifts for the lines,
- asymmetric line shapes,
- emission lines emerging in the deepest dip.

The lower charge states of both elements only appear in the deeper dip stages, pointing towards colder material shielded from the irradiation by the black hole. The total columns in the dip stages derived from the equivalent widths of the lines represent lower limits to the real values, as we cannot see the fully ionized material adding to the column, which is likely to carry most of the mass. The derived N_{H} values of $N_{\mathrm{H}} \sim 2 \ldots 4 \cdot 10^{21}\,\mathrm{cm}^{-2}$ are in agreement with previous results from paper I, although there are slight differences due to differences in the continuum.

The Doppler shifts of the lines with respect to measured laboratory values (Hell et al., 2016) show a scatter between the different dip stages, but the same trend within a single observation, pointing towards a single structure containing different ionization stages, which moves as a whole with a certain speed. The Doppler velocities show a clear modulation with orbital phase and are in agreement with the results found in paper II. However, they match neither the expected wind velocities calculated from a toy model after Gies & Bolton (1986a) nor free-fall nor the Kepler velocity around the black hole. Thus, from the line shifts it is not possible to tell where the material causing the absorption dips in the lightcurve is located.

For the three observations around $\phi_{\rm orb} = 0$, the lines show asymmetries. This is expected from previous observations near superior conjunction (see paper I and references therein). Clear P Cygni-like profiles are reported only near $\phi_{\rm orb} = 0.5$.

Within the deepest dip, there is an emission line spectrum emerging that is outshone otherwise. Together with the Si xiii emission line which does not change its total line flux during the dip stages, this emission line spectrum indicates a much larger area responsible for the emission than what is absorbed by the wind structures, or an area distant from the absorber such that the line of sight towards it is not affected. A possibility is the almost fully ionized photoionization region in the stellar wind surrounding the X-ray emission region. (Hirsch et al., 2019)

A larger effective area and improvements in spectral resolution are needed to be able to look at single, consecutive dips and thus probe the structure of the stellar wind at close range. The silicon and sulfur line measurements also stress the need for more experimental data for plasma physics, not only to compare results from lab and space but also to improve the codes used to calculate line positions, strengths and ratios.

Outlook

While time is the key feature for building up a comprehensive sample of super soft sources and their timing behavior as well as to continue the monitoring of the peculiar behavior of GRS 1758−258, a huge step forward in spectral resolution, even for short integration times, is needed to gain more insight into the clumpy wind structure of Cyg X-1.

It has been a while since the launch of *Chandra* and *XMM*, *INTEGRAL* and *Swift*. Technical development in the meantime opened up many new possibilities. *NuSTAR* (Harrison et al., 2013) with its extendable optical bench was launched on June 13, 2012 and is since investigating supermassive black holes (e.g., Risaliti et al., 2013) and exploring the radioactive matter in supernova remnants in the hard X-rays (e.g., Grefenstette et al., 2014). *Hitomi* (Takahashi et al., 2016), the Japanese mission launched on February 17, 2016, showed already during its short life time[1] that using a microcalorimeter like the Soft X-ray Spectrometer (SXS, Kelley et al., 2016) provides insights into conditions in an astrophysical plasma (Hitomi Collaboration et al., 2016, 2018).

A microcalorimeter is an X-ray detector consisting of an absorber, a thermistor and a heat sink. The energy of an X-ray photon hitting the absorber is converted to heat. This heat is then transferred to the thermistor, mostly a semiconductor operated at a temperature where it shows a large response in resistance for a small change in material temperature. This change in resistivity is measured, allowing to retrieve the energy of the incoming photon, and the detector is cooled down to its original temperature using the heat sink. Thus, a microcalorimeter is a singe photon detector. The cooling obviously is a challenge in space: Microcalorimeters typically work at temperatures of $T < 0.1\,\mathrm{K}$, well below the temperature of the cosmic microwave background of 2.7 K. Liquid helium is used by a three-stage adiabatic demagnetization refrigerator (ADR) to reach this low operating temperature. While the use of liquid helium limits the lifetime of the instrument in space, an operation time of the cooling system of at least three years can be guaranteed, and the high resolution and high throughput of a cryogenic X-ray microcalorimeter, which cannot be achieved by the classical

[1] Due to technical issues, *Hitomi* broke apart on March 26, 2016.

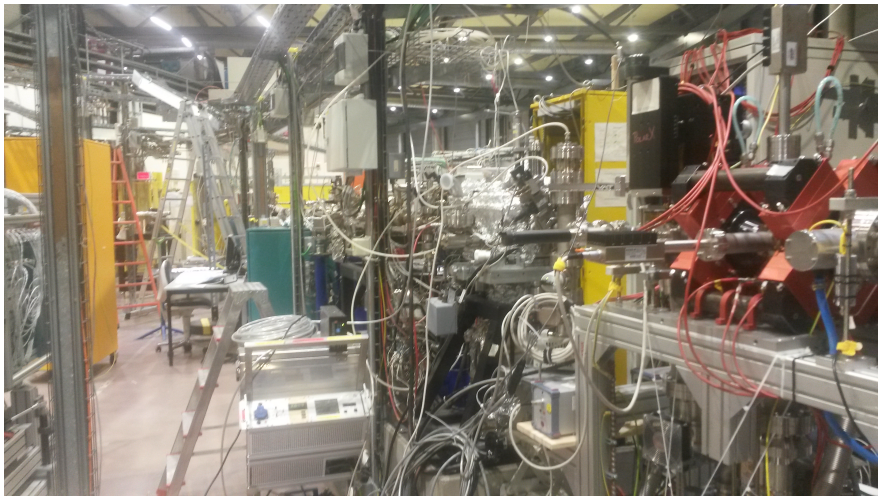

Figure 6.1: Part of the setup used at a laboratory astronomy measurement at the BESSY synchrotron in Berlin, taken in October 2017.

X-ray observing techniques, still make it worthwhile to put such an instrument on a satellite.

The replacement mission of *Hitomi*, *XRISM*[2], will carry another microcalorimeter like the SXS which will partly be built from flight spare parts of the original. *Athena* with its X-ray Integral Field Unit (X-IFU, Barret et al., 2016) will also have an X-ray microcalorimeter aboard, and will increase the angular resolution to about 5″ compared to *XRISM*'s 1′ pixels, and will be able to observe even bright sources. The *LYNX* observatory[3] proposed for the NASA 2020 decadal survey also counts on the cryogenic microcalorimeter technique.

While new satellites are developed, built and launched, research on ground, too, pushes to improve our knowledge of atomic physics and spectral lines. An example for this are the measurements of silicon and sulfur line positions by Hell et al. (2016) with an Electron Beam Ion Trap (EBIT), on which the Doppler measurement in this work is based. Without a detailed knowledge of the behavior of atoms, ions and plasmas under normal circumstances, it is impossible to investigate the influence of the extreme physical conditions space is providing us with. In a combined effort (an example can be seen in Fig. 6.1), laboratory physicists and astronomers are striving to solve the current problems – and uncover new ones!

[2] https://heasarc.gsfc.nasa.gov/docs/xrism/
[3] https://www.lynxobservatory.com/

Manuscript sent, my spirits were soaring
till it came back stamped "This book is boring,
Your prose so verbose,
left us near comatose,
and your readers can still be heard snoring."

(Lee Durben)

References

Abbe E., 1881, Journal of the Royal Microscopical Society 1, 388

Abbey T., Carpenter J., Read A., et al., 2006, In: Wilson A. (ed.) The X-ray Universe 2005, Vol. 604. ESA Special Publication, p. 943

Abbott B.P., Abbott R., Abbott T.D., et al., 2016, Physical Review Letters 116, 061102

Abbott D.C., 1978, ApJ 225, 893

Amelio G.F., Tompsett M.F., Smith G.E., 1970, The Bell System Technical Journal 49, 593

Aschenbach B., 2009, Experimental Astronomy 26, 95

Aveni A.F., 1993, Ancient Astronomers, St. Remy Press and Smithsonian Institution, 1 edition

Balbus S.A., Henri P., 2008, ApJ 674, 408

Balmer J.J., 1885, Wiedemann's Annalen 25

Bałucińska-Church M., Church M.J., Charles P.A., et al., 2000, MNRAS 311, 861

Barcons X., Barret D., Decourchelle A., et al., 2012, arXiv e-prints arXiv:1207.2745

Barret D., Lam Trong T., den Herder J.W., et al., 2016, In: Space Telescopes and Instrumentation 2016: Ultraviolet to Gamma Ray. Proc. SPIE Vol. 9905, 99052F, Bellingham, WA: SPIE

Barthelmy S.D., Barbier L.M., Cummings J.R., et al., 2005, Space Sci. Rev. 120, 143

Beardmore A.P., Balman S., Osborne J.P., et al., 2010, ATEL 2423

Beardmore A.P., Osborne J.P., Page K.L., 2013, ATEL 5573

Begelman M.C., Armitage P.J., 2014, ApJ 782, L18

Blondin J.M., 1994, ApJ 435, 756

Blondin J.M., Kallman T.R., Fryxell B.A., Taam R.E., 1990, ApJ 356, 591

Blondin J.M., Stevens I.R., Kallman T.R., 1991, ApJ 371, 684

Blondin J.M., Woo J.W., 1995, ApJ 445, 889

Bode M.F., O'Brien T.J., Osborne J.P., et al., 2006, ApJ 652, 629

Bode M.F., Priedhorsky W.C., Norwell G.A., Evans A., 1985, ApJ 299, 845

Boella G., Butler R.C., Perola G.C., et al., 1997, A&AS 122, 299

Bohr N., 1913a, Phil. Mag. 26, 1

Bohr N., 1913b, Phil. Mag. 26, 476

Bohr N., 1913c, Phil. Mag. 26, 857

Bonferroni C.E., 1936, Pubblicazioni del R Istituto Superiore di Scienze Economiche e Commerciali di Firenze 8, 3

Bouret J., Lanz T., Hillier D.J., 2005, A&A 438, 301

Bowyer S., Byram E.T., Chubb T.A., Friedman H., 1965, Ann. Astrophys. 28, 791

Boyle W.S., Smith G.E., 1970, Bell System Technical Journal 49, 587

Bradt H., 2004, Astronomy Methods: A Physical Approach to Astronomical Observations, Cambridge: Cambridge Univ. Press

Bradt H.V., Rothschild R.E., Swank J.H., 1993, A&AS 97, 355

Bragg W.H., Bragg W.L., 1913, Proceedings of the Royal Society of London A: Mathematical, Physical and Engineering Sciences 88, 428

Brandt S., Lund N., Rao A.R., 1990, Adv. Space Res. 10, 239

Brinkman B.C., Gunsing T., Kaastra J.S., et al., 2000, In: Truemper J.E., Aschenbach B. (eds.) X-Ray Optics, Instruments, and Missions III. Proc. SPIE Vol. 4012, 81-90, Bellingham, WA: SPIE

Brocksopp C., Fender R.P., Larionov V., et al., 1999, MNRAS 309, 1063

Burrows D.N., Hill J.E., Nousek J.A., et al., 2005, Space Sci. Rev. 120, 165

Caballero-Nieves S.M., Gies D.R., Bolton C.T., et al., 2009, ApJ 701, 1895

Canizares C.R., Davis J.E., Dewey D., et al., 2005, PASP 117, 1144

Canizares C.R., Huenemoerder D.P., Davis D.S., et al., 2000, ApJ 539, L41

Capalbi M., Perri M., Saija B., et al., 2005 http://www.swift.ac.uk/analysis/files/xrt_swguide_v1_2.pdf

Carroll B.W., Ostlie D.A., 1996, An Introduction to Modern Astrophysics, Pearson Education Limited

Castor J.I., Abbott D.C., Klein R.I., 1975, ApJ 195, 157

Chakrabarti S., Titarchuk L.G., 1995, ApJ 455, 623

Chandrasekhar S., 1931a, MNRAS 91, 456

Chandrasekhar S., 1931b, ApJ 74, 81

Chandrasekhar S., 1935, MNRAS 95, 207

Chang K.M., Kylafis N.D., 1983, ApJ 265, 1005

Clark G.W., 1965, Phys. Rev. Lett. 14, 91

Clarke R., 1990, Nuclear Instruments and Methods in Physics Research Section A: Accelerators, Spectrometers, Detectors and Associated Equipment 291, 117

Clarke R., 1994, Nuclear Instruments and Methods in Physics Research Section A: Accelerators, Spectrometers, Detectors and Associated Equipment 347, 529

Collon M.J., Kraft S., Günther R., et al., 2006, In: Society of Photo-Optical Instrumentation Engineers (SPIE) Conference Series. Proc. SPIE Vol. 6266, 62661T, Bellingham, WA: SPIE

Compton A.H., 1923, Phys. Rev. 21

Coulomb C.A.d., 1785a, Histoire de l'Académie Royale des Sciences 569–577

Coulomb C.A.d., 1785b, Histoire de l'Académie Royale des Sciences 578–611

Davis S.W., Blaes O.M., Hubeny I., Turner N.J., 2005, ApJ 621, 372

Debnath D., Mondal S., Chakrabarti S.K., 2015, MNRAS 447, 1984

den Herder J.W., Brinkman A.C., Kahn S.M., et al., 2001, A&A 365, L7

Dessart L., Owocki S.P., 2003, A&A 406, L1

Dotani T., Inoue H., Mitsuda K., et al., 1997, ApJ 485, L87

Dove J.B., Wilms J., Maisack M., Begelman M.C., 1997, ApJ 487, 759

Drake G.W., 1988, Can. J. Phys. 66, 586

Esin A.A., McClintock J.E., Narayan R., 1997, ApJ 489, 865

Euler L., 1757, Mémoires de l'académie des sciences de Berlin 11, 217

Eversberg T., Lepine S., Moffat A.F.J., 1998, ApJ 494, 799

Feldmeier A., Puls J., Pauldrach A.W.A., 1997, A&A 322, 878

Feng Y.X., Cui W., 2002, ApJ 564, 953

Feng Y.X., Tennant A.F., Zhang S.N., 2003, ApJ 597, 1017

Ferreira J., Petrucci P.O., Henri G., et al., 2006, A&A 447, 813

Fewell M.P., 1995, American Journal of Physics 63, 653

Fock V., 1935, Z. Phys. 98, 145

Forman W., Jones C., Cominsky L., et al., 1978, ApJS 38, 357

Frank J., King A., Raine D.J., 2002, Accretion Power in Astrophysics: Third Edition, Cambridge: Cambridge Univ. Press

Fraunhofer J.v., 1814, Denkschriften der Königlichen Akademie der Wissenschaften zu München 5, 193

Friedrich H., 1990, Theoretical Atomic Physics, 1st edition, Berlin, Heidelberg, New York: Springer

Friend D.B., Abbott D.C., 1986, ApJ 311, 701

Friend D.B., Castor J.I., 1982, ApJ 261, 293

Friend D.B., Castor J.I., 1983, ApJ 272, 259

Fryer C.L., Kalogera V., 2001, ApJ 554, 548

Fullerton A.W., Massa D.L., Prinja R.K., 2006, ApJ 637, 1025

Gabriel A.H., 1972, MNRAS 160, 99

Gandhi P., Rao A., Johnson M.A.C., et al., 2018, ArXiv e-prints

Garcia J.D., Mack J.E., 1965, Journal of the Optical Society of America 55, 654

Garmire G.P., Bautz M.W., Ford P.G., et al., 2003, In: Truemper J.E., Tananbaum H.D. (eds.) X-Ray and Gamma-Ray Telescopes and Instru-

ments for Astronomy. Proc. SPIE Vol. 4851, 28-44, Bellingham, WA: SPIE

Garstang R.H., 1962, In: D. R. Bates (ed.) Atomic and Molecular Processes., Academic Press, New York, p. 1

Gehrels N., Chincarini G., Giommi P., et al., 2004, ApJ 611, 1005

Ghosh A., Chakrabarti S.K., 2018, MNRAS 479, 1210

Giacconi R., Branduardi G., Briel U., et al., 1979, ApJ 230, 540

Giacconi R., Kellogg E., Gorenstein P., et al., 1971, ApJ 165, L27

Giacconi R., Rossi B., 1960, J. Geophys. Res. 65, 773

Gierliński M., Newton J., 2006, MNRAS 370, 837

Gies D.R., Bolton C.T., 1986a, ApJ 304, 371

Gies D.R., Bolton C.T., 1986b, ApJ 304, 389

Gies D.R., Bolton C.T., Blake R.M., et al., 2008, ApJ 678, 1237

Gies D.R., Bolton C.T., Thomson J.R., et al., 2003, ApJ 583, 424

Grefenstette B.W., Harrison F.A., Boggs S.E., et al., 2014, Nature 506, 339

Greiner J., Hasinger G., Kahabka P., 1991, A&A 246, L17

Grevesse N., Noels A., Sauval A.J., 1996, In: Holt S.S., Sonneborn G. (eds.) Cosmic Abundances., Astron. Soc. Pacific Conf. Ser. 99, 117, Orem, UT: ASPCS

Grinberg V., Hell N., El Mellah I., et al., 2017, A&A 608, A143

Grinberg V., Hell N., Pottschmidt K., et al., 2013, A&A 554, A88

Grinberg V., Leutenegger M.A., Hell N., et al., 2015, A&A 576, A117

Grotrian W., 1928, Graphische Darstellung der Spektren von Atomen und Ionen mit ein, zwei und drei Valenzelektronen, 2 Teile, Springer-Verlag, Berlin

Gursky H., Bradt H., Doxsey R., et al., 1978, ApJ 223, 973

Haardt F., Maraschi L., 1991, ApJ 380, L51

Hachisu I., Kato M., 2006a, ApJS 167, 59

Hachisu I., Kato M., 2006b, ApJ 642, L53

Hachisu I., Kato M., Nomoto K., 1996, ApJ 470, L97

Hanke M., 2011, Ph.D. thesis, Friedrich Alexander Universität Erlangen-Nürnberg

Hanke M., Wilms J., Nowak M.A., et al., 2009, ApJ 690, 330

Hanke M., Wilms J., Nowak M.A., et al., 2008, In: VII Microquasar Workshop: Microquasars and Beyond., PoS (MQW7) 029

Harrison F.A., Christensen F.E., Craig W., et al., 2005, Experimental Astronomy 20, 131

Harrison F.A., Craig W.W., Christensen F.E., et al., 2013, ApJ 770, 103

Heindl W.A., Smith D.M., 2002, ApJ 578, L125

Heisenberg W., 1927, ZPh 43, 172

Hell N., 2017, Ph.D. thesis, Universität Erlangen-Nürnberg, Lawrence Livermore National Laboratory

Hell N., Brown G.V., Wilms J., et al., 2016, ApJ 830, 26

Hell N., Miskovicova I., Brown G., et al., 2013, In: HCI conf. proc.

Hemphill P.B., Rothschild R.E., Markowitz A., et al., 2014, ApJ 792, 14

Herrero A., Kudritzki R.P., Gabler R., et al., 1995, A&A 297, 556

Hirsch M., Hell N., Grinberg V., et al., 2019, A&A submitted

Hirsch M., Pottschmidt K., Krauss F., et al., 2016, ATEL 9890

Hirsch M., Pottschmidt K., Smith D.M., et al., 2018, X-ray spectral and flux variability of the microquasar GRS 1758-258 on timescales from weeks to years, submitted

Hitomi Collaboration, Aharonian F., Akamatsu H., et al., 2016, Nature 535, 117

Hitomi Collaboration, Aharonian F., Akamatsu H., et al., 2018, PASJ 70, 9

Horne J.H., Baliunas S.L., 1986, ApJ 302, 757

Houck J.C., 2002, In: G. Branduardi-Raymont (ed.) High Resolution X-ray Spectroscopy with XMM-Newton and Chandra, London: MSSL.

Houck J.C., Denicola L.A., 2000, In: Manset N., Veillet C., Crabtree D. (eds.) Astronomical Data Analysis Software and Systems IX. Astron. Soc. Pacific Conf. Ser. 216, 591, Orem, UT: ASPCS

Hund F., 1925, ZPh

Jahoda K., Swank J.H., Giles A.B., et al., 1996, In: Siegmund O.H., Gummin M.A. (eds.) EUV, X-Ray, and Gamma-Ray Instrumentation for Astronomy VII. Proc. SPIE Vol. 2808, 59-70,

Bellingham, WA: SPIE

Jansen F., Lumb D., Altieri B., et al., 2001, A&A 365, L1

Kahabka P., Pietsch W., Hasinger G., 1994, A&A 288, 538

Kahabka P., van den Heuvel E.P.J., 1997, ARA&A 35, 69

Kallman T., Bautista M., 2001, ApJS 133, 221

Kalogera V., 1998, ApJ 493, 368

Kalogera V., Webbink R.F., 1998, ApJ 493, 351

Karttunen H., Krüger P., Oja H., et al., 2007, Fundamental Astronomy, Springer-Verlag, Berlin Heidelberg New York

Kawaler S.D., 1988, ApJ 334, 220

Keller C.U., 1995, Experientia 51, 710

Kelley R.L., Akamatsu H., Azzarello P., et al., 2016, In: Space Telescopes and Instrumentation 2016: Ultraviolet to Gamma Ray. Proc. SPIE Vol. 9005, 99050V, Bellingham, WA: SPIE

Kippenhahn R., Weigert A., Weiss A., 2012, Stellar Structure and Evolution

Kitamoto S., Miyamoto S., Tanaka Y., et al., 1984, PASJ 36, 731

Klencki J., Wiktorowicz G., Gładysz W., Belczynski K., 2017, MNRAS 469, 3088

Kniffen D.A., 1989, Annals of the New York Academy of Sciences 571, 482

Kraft R.P., Chappell J.H., Kenter A.T., et al., 2000, In: Truemper J.E., Aschenbach B. (eds.) X-Ray Optics, Instruments, and Missions III. Proc. SPIE Vol. 4012, 493-517, Bellingham, WA: SPIE

Krimm H.A., Holland S.T., Corbet R.H.D., et al., 2013, ApJS 209, 14

Krolik J.H., McKee C.F., Tarter C.B., 1981, ApJ 249, 422

Kuulkers E., Shaw S.E., Paizis A., et al., 2007, A&A 466, 595

Labanti C., Di Cocco G., Ferro G., et al., 2003, A&A 411, L149

Lanz T., Telis G.A., Audard M., et al., 2005, ApJ 619, 517

Larsson S., 1996, A&AS 117, 197

Lebrun F., Leray J.P., Lavocat P., et al., 2003, A&A 411, L141

Lense J., Thirring H., 1918, Physikalische Zeitschrift 19

Lesser M., 2015, PASP 127, 1097

Lewin W.H.G., van Paradijs J., van den Heuvel E.P.J., 1997, X-ray Binaries, Cambridge: Cambridge Univ. Press

Li K.F., Clark G.W., 1974, ApJ 191, L27

Livio M., 1992, ApJ 393, 516

Long K.S., Helfand D.J., Grabelsky D.A., 1981, ApJ 248, 925

Lubow S.H., Papaloizou J.C.B., Pringle J.E., 1994, MNRAS 267, 235

Lund N., Budtz-Jørgensen C., Westergaard N.J., et al., 2003, A&A 411, L231

Luque-Escamilla P.L., Martí J., Muñoz-Arjonilla Á.J., 2014, ApJ 797, L1

Lyman T., 1906, ApJ 23, 181

Mahoney W.A., Ling J.C., Jacobson A.S., Taphorn R.M., 1980, Nuclear Instruments and Methods 178, 363

Main D.S., Smith D.M., Heindl W.A., et al., 1999, ApJ 525, 901

Mandrou P., 1990, IAU Circ. 5032, 1

Manousakis A., Walter R., 2011, A&A 526, A62

Manousakis A., Walter R., 2015, A&A 575, A58

Marcel G., Ferreira J., Petrucci P.O., et al., 2018a, A&A 617, A46

Marcel G., Ferreira J., Petrucci P.O., et al., 2018b, A&A 615, A57

Markoff S., Nowak M.A., 2004, ApJ 609, 972

Markova N., Puls J., Scuderi S., Markov H., 2005, A&A 440, 1133

Martí J., Luque-Escamilla P.L., Bosch-Ramon V., Paredes J.M., 2017, Nature Communications 8, 1757

Martí J., Luque-Escamilla P.L., Muñoz-Arjonilla Á.J., 2016, A&A 596, 46

Martínez-Núñez S., Kretschmar P., Bozzo E., et al., 2017, Space Sci. Rev. 212, 59

Martocchia A., Matt G., 1996, MNRAS 282, L53

Mas-Hesse J.M., Giménez A., Culhane J.L., et al., 2003, A&A 411, L261

Mason K.O., Breeveld A., Much R., et al., 2001, A&A 365, L36

Mason K.O., Hawkins F.J., Sanford P.W., et al., 1974, ApJ 192, L65

Matt G., Perola G.C., Piro L., Stella L., 1992, A&A 257, 63

Matteson J.L., (ed.) 1978, The UCSD/MIT hard X-ray and low energy gamma-ray experiment for

HEAO-1 - Design and early results, Huntsville: AIAA

Mereghetti S., Cremonesi D.I., Haardt F., et al., 1997, ApJ 476, 829

Meyer F., Liu B.F., Meyer-Hofmeister E., 2000, A&A 361, 175

Meyer-Hofmeister E., Liu B.F., Meyer F., 2009, A&A 508, 329

Michaely E., Perets H.B., 2016, MNRAS 458, 4188

Miller J.M., Fabian A.C., Wijnands R., et al., 2002, ApJ 578, 348

Miškovičová I., Hanke M., Wilms J., et al., 2011, Acta Polytechnica 51, 4

Miškovičová I., Hell N., Hanke M., et al., 2016, A&A 590, A114

Morton D.C., 1967, ApJ 150, 535

Muñoz-Arjonilla A.J., Martí J., Luque-Escamilla P.L., et al., 2010, A&A 519, A15

Muijres L.E., Vink J.S., de Koter A., et al., 2012, A&A 537, A37

Murakami T., Fujii M., Hayashida K., et al., 1989, PASJ 41, 405

Murdin P., Webster B.L., 1971, Nature 233, 110

Murray S.S., Austin G.K., Chappell J.H., et al., 2000, In: Truemper J.E., Aschenbach B. (eds.) X-Ray Optics, Instruments, and Missions III. Proc. SPIE Vol. 4012, 68-80, Bellingham, WA: SPIE

Mushtukov A.A., Suleimanov V.F., Tsygankov S.S., Poutanen J., 2015, MNRAS 454, 2539

Nagarkoti S., Chakrabarti S.K., 2016, MNRAS 462, 850

Nelson T., Orio M., Cassinelli J.P., et al., 2008, ApJ 673, 1067

Ness J.U., Beardmore A.P., Osborne J.P., et al., 2015, A&A 578, A39

Ness J.U., Schaefer B.E., Dobrotka A., et al., 2012, ApJ 745, 43

Ness J.U., Schwarz G.J., Page K.L., et al., 2013, ATEL 5626

Ness J.U., Starrfield S., Beardmore A.P., et al., 2007, ApJ 665, 1334

Newsham G., Starrfield S., Timmes F.X., 2014, In: Woudt P.A., Ribeiro V.A.R.M. (eds.) Stellar Novae: Past and Future Decades, Vol. 490. Astronomical Society of the Pacific Conference Series, p. 287

Nixon C., Salvesen G., 2014, MNRAS 437, 3994

Noble M.S., Nowak M.A., 2008, PASP 120, 821

Nowak M.A., Hanke M., Trowbridge S.N., et al., 2011, ApJ 728, 13

Nowak M.A., Juett A., Homan J., et al., 2008, ApJ 689, 1199

Odendaal A., Meintjes P.J., 2017, MNRAS 467, 2797

Odendaal A., Meintjes P.J., Charles P.A., Rajoelimanana A.F., 2014, MNRAS 437, 2948

Orosz J.A., McClintock J.E., Aufdenberg J.P., et al., 2011, ApJ 742, 84

Osborne J., Page K., Beardmore A., et al., 2006a, ATEL 764

Osborne J., Page K., Beardmore A., et al., 2006b, ATEL 770

Osborne J., Page K., Beardmore A., et al., 2006c, ATEL 838

Osborne J.P., Page K.L., Beardmore A.P., et al., 2011, ApJ 727, 124

Oskinova L.M., Feldmeier A., Hamann W., 2006, MNRAS 372, 313

Oskinova L.M., Feldmeier A., Kretschmar P., 2012, MNRAS 421, 2820

Owocki S., van Marle A.J., 2008, In: Bresolin F., Crowther P.A., Puls J. (eds.) Massive Stars as Cosmic Engines. IAU Symposium 250, 71-82, Cambridge: Cambridge Univ. Press

Owocki S.P., Castor J.I., Rybicki G.B., 1988, ApJ 335, 914

Owocki S.P., Rybicki G.B., 1984, ApJ 284, 337

Pakull M.W., Beuermann K., van der Klis M., van Paradijs J., 1988, A&A 203, L27

Palmeri P., Quinet P., Mendoza C., et al., 2008, ApJS 177, 408

Parker M.L., Tomsick J.A., Miller J.M., et al., 2015, ApJ 808, 9

Parsignault D.R., Epstein A., Grindlay J., et al., 1976, Ap&SS 42, 175

Pauldrach A., Puls J., Kudritzki R.P., 1986, A&A 164, 86

Pauli W., 1925, ZPh 31, 765

Pepe C., Vila G.S., Romero G.E., 2015, A&A 584, A95

Petrucci P.O., Ferreira J., Henri G., Pelletier G., 2008, MNRAS 385, L88

Piro A.L., Bildsten L., 2004, ApJ 603, 252

Planck M., 1900, Verhandlungen der Deutschen Physikalischen Gesellschaft 2, 237

Porquet D., Dubau J., 2000, A&AS 143, 495

Porquet D., Dubau J., Grosso N., 2010, Space Sci. Rev. 157, 103

Porquet D., Mewe R., Dubau J., et al., 2001, Astronomy and Astrophysics 376, 1113

Pottschmidt K., Chernyakova M., Lubiński P., et al., 2008, In: Proceedings of "An INTEGRAL view of compact objects" – 7th INTEGRAL Workshop., PoS, id.67

Pottschmidt K., Eikmann W., Kreykenbohm I., et al., 2016, ATEL 9625

Poutanen J., Zdziarski A.A., Ibragimov A., 2008, MNRAS 389, 1427

Pradhan A., Nahar S., 2015, Atomic Astrophysics and Spectroscopy, Cambridge University Press, New York

Pravdo S.H., White N.E., Becker R.H., et al., 1980, ApJ 237, L71

Pringle J.E., 1981, Annual Review of Astronomy and Astrophysics 19, 137

Puls J., Markova N., Scuderi S., et al., 2006, A&A 454, 625

Puls J., Vink J.S., Najarro F., 2008, A&A Rev. 16, 209

Rahoui F., Lee J.C., Heinz S., et al., 2011, ApJ 736, 63

Reid M.J., McClintock J.E., Narayan R., et al., 2011, ApJ 742, 83

Remillard R.A., Canizares C.R., 1984, ApJ 278, 761

Reppin C., Pietsch W., Trümper J., et al., 1985, in: Non-thermal and Very High Temperature Phenomena in X-ray Astronomy, p.279, Roma: Univers. "La Sapienzia", Istittuto Astronomico

Reynolds C.S., 1999, In: Poutanen J., Svensson R. (eds.) High Energy Processes in Accreting Black Holes. Astron. Soc. Pacific Conf. Ser. 161, 178, Orem, UT: ASPCS

Risaliti G., Harrison F.A., Madsen K.K., et al., 2013, Nature 494, 449

Ritter H., Kolb U., 2003, A&A 404, 301

Rodriguez L.F., Mirabel I.F., Marti J., 1992, ApJ 401, L15

Roming P.W.A., Kennedy T.E., Mason K.O., et al., 2005, Space Sci. Rev. 120, 95

Roques J.P., Paul J., Mandrou P., Lebrun F., 1990, Adv. Space Res. 10, 223

Rosenberg M., Russo P., Bladon G., Lindberg Christensen L., 2013, ArXiv e-prints 1311.0508

Rothschild R., Boldt E., Holt S., et al., 1979, Space Science Instrumentation 4, 269

Rothstein D.M., Eikenberry S.S., Chatterjee S., et al., 2002, ApJ 580, L61

Rowland H.A., 1882, Phil. Mag. 13, 469

Rowland H.A., 1883, Phil. Mag. Series 5 16, 197

Russell H.N., Saunders F.A., 1925, ApJ 61, 38

Rutherford E., 1911, Phil. Mag. Ser.6 21, 669

Sako M., Liedahl D.A., Kahn S.M., Paerels F., 1999, ApJ 525, 921

Scargle J.D., 1982, ApJ 263, 835

Schmidtke P.C., McGrath T.K., Cowley A.P., Frattare L.M., 1993, PASP 105, 863

Schrödinger E., 1926a, Phys. Rev. 28, 1049

Schrödinger E., 1926b, Ann. d. Phys. 79, 361

Schulz N.S., Canizares C.R., Lee J.C., Sako M., 2002a, ApJ 564, L21

Schulz N.S., Cui W., Canizares C.R., et al., 2002b, ApJ 565, 1141

Schwartz R.A., Ling J.C., Mahoney W.A., Jacobson A.S., 1987, ApJ 317, 846

Seward F.D., Mitchell M., 1981, ApJ 243, 736

Shakura N.I., Sunyaev R.A., 1973, A&A 24, 337

Siegbahn K.M., 1924, Spektroskopie der Röntgenstrahlen, Berlin: Springer

Siuniaev R.A., Babichenko S.I., Goganov D.A., et al., 1990, Adv. Space Res. 10, 233

Smale A.P., Corbet R.H.D., Charles P.A., et al., 1988, MNRAS 233, 51

Smith D.M., Dawson D.M., Swank J.H., 2007, ApJ 669, 1138

Smith D.M., Heindl W.A., Markwardt C.B., Swank J.H., 2001, ApJ 554, L41

Smith D.M., Heindl W.A., Swank J.H., 2002a, ApJ 578, L129

Smith D.M., Heindl W.A., Swank J.H., 2002b, ApJ 569, 362

Sommerfeld A., 1940, Naturwissenschaften 28, 417

Soria R., Broderick J.W., Hao J., et al., 2011, MNRAS 415, 410

Strüder L., Briel U., Dennerl K., et al., 2001, A&A 365, L18

Sundqvist J.O., Owocki S.P., 2013, MNRAS 428,

1837

Sundqvist J.O., Owocki S.P., Cohen D.H., et al., 2012, MNRAS 420, 1553

Sundqvist J.O., Owocki S.P., Puls J., 2018, A&A 611, A17

Syunyaev R., Gilfanov M., Churazov E., et al., 1991, Sov. Astron. Let. 17, 50

Takahashi T., Kokubun M., Mitsuda K., et al., 2016, In: Space Telescopes and Instrumentation 2016: Ultraviolet to Gamma Ray. Proc. SPIE Vol. 9905, 99050U, Bellingham, WA: SPIE

Tanaka Y., Inoue H., Holt S.S., 1994, PASJ 46, L37

Taylor B.G., Andresen R.D., Peacock A., Zobl R., 1981, Space Sci. Rev. 30, 479

Tetarenko B.E., Sivakoff G.R., Heinke C.O., Gladstone J.C., 2016, ApJS 222, 15

Timmes F.X., Woosley S.E., Weaver T.A., 1996, ApJ 457, 834

Torrejón J.M., Schulz N.S., Nowak M.A., et al., 2015, ApJ 810, 102

Treis J., Fischer P., Hälker O., et al., 2004, In: Holland A.D. (ed.) High-Energy Detectors in Astronomy. Proc. SPIE Vol. 5501, 89-100, Bellingham, WA: SPIE

Truman H.S., 1949, Inaugural Address, https://www.trumanlibrary.org/whistlestop/50yr_archive/inagural20jan1949.htm

Trümper J., 1982, Adv. Space Res. 2, 241

Trümper J.E., Hasinger G., 2008, The Universe in X-Rays, Berlin, Heidelberg: Springer

Tsunemi H., Kitamoto S., Manabe M., et al., 1989, PASJ 41, 391

Tucker W.H., 1984, NASA Special Publication 466, Washington: US Government Printing Office

Turner M.J.L., Abbey A., Arnaud M., et al., 2001, A&A 365, L27

Turner M.J.L., Thomas H.D., Patchett B.E., et al., 1989, PASJ 41, 345

Ubertini P., Lebrun F., Di Cocco G., et al., 2003, A&A 411, L131

Vaytet N.M.H., O'Brien T.J., Bode M.F., 2007, ApJ 665, 654

Vaytet N.M.H., O'Brien T.J., Page K.L., et al., 2011, ApJ 740, 5

Vedrenne G., Roques J.P., Schönfelder V., et al., 2003, A&A 411, L63

Verner D.A., Ferland G.J., Korista K.T., Yakovlev D.G., 1996a, ApJ 465, 487

Verner D.A., Verner E.M., Ferland G.J., 1996b, Atomic Data and Nuclear Data Tables 64, 1

Vrtilek S.D., Boroson B.S., Hunacek A., et al., 2008, ApJ 678, 1248

Walborn N.R., 1973, ApJ 179, p.L123

Warner B., Woudt P.A., 2002, MNRAS 335, 84

Watanabe S., Sako M., Ishida M., et al., 2006, ApJ 651, 421

Webster B.L., Murdin P., 1972, Nature 235, 37

Wen L., Cui W., Levine A.M., Bradt H.V., 1999, ApJ 525, 968

Wheaton W.A., Jacobson A.S., Ling J.C., et al., 1989, AIP Conference Proceedings 186, 304-322, Melville:A IP Publishing Center

Wheeler J.C., Pooley D., 2013, ApJ 762, 75

Whelan J., Iben, Jr. I., 1973, ApJ 186, 1007

Wilms J., Allen A., McCray R., 2000, ApJ 542, 914

Wilms J., Nowak M.A., Pottschmidt K., et al., 2001, MNRAS 320, 327

Wilms J., Nowak M.A., Pottschmidt K., et al., 2006, A&A 447, 245

Winkler C., Courvoisier T.J.L., Di Cocco G., et al., 2003, A&A 411, L1

Wojdowski P.S., Liedahl D.A., Sako M., et al., 2003, ApJ 582, 959

Wolf W.M., Townsend R.H.D., Bildsten L., 2018, ApJ 855, 127

Wolter H., 1952, Annalen der Physik 445, 94

Woosley S.E., Heger A., Weaver T.A., 2002, Reviews of Modern Physics 74, 1015

Xiang J., Lee J.C., Nowak M.A., Wilms J., 2011, ApJ 738, 78

Zeeman P., 1896a, Versl. K. Akad. Wet. Amsterdam 5, 181

Zeeman P., 1896b, Versl. K. Akad. Wet. Amsterdam 5, 242

Zeeman P., 1897, Phil. Mag. 43, 226

An acknowledgment lets you give thanks,
Thus acknowledging all of the ranks
  Of the folks who resisted
  When most had insisted
That all who believed you were cranks.

(Seth Brown)

Acknowledgments

The amount of work that goes into a Ph.D. thesis is so much more than what is finally written down and handed in, and the number of people who have, in some part or other, contributed to its completion, is large. I want to thank

Jörn, my supervisor – You definitely are the one person without whom none of this would have been possible. I want to thank you for ten years of enthusiastically letting me and everyone else around you partake in your passion for astronomy, physics and science in general. Thanks for sharing not only your knowledge and your books but also your contacts around the world for fruitful discussions on many topics!

Ingo – for always taking the time for a discussion and for miraculously solving every computer problem I ever had.

The Remeis Admins – for doing an amazing job in the background which is often unseen. It was an honor to help you out a bit in the last two years!

Edith, the best secretary in the world – for always keeping track of things! I wish you "einen wunderschönen guten Morgen!" ;-) and I am sorry for causing such an amount of paperwork during my time at Remeis.

The observatory would not be the same without all the "Remeisen" working there. The friendly environment, where helping each other just is a given, is priceless! Please keep up this spirit! My special thanks goes to

Matthias – for helping with countless `isis` questions and for great teamwork in the webpage project, and

Ralf – for keeping the office warm and the cookie jar filled, and always having an open ear for everything.

Leaving the observatory thankfully does not prevent people from collaborating. I want to thank the Remeis graduates who have already left for never stopping to share their expertise, especially

Fe – for remotely teaching me how to use *Swift*,

Vici, my Cyg X-1 specialist – for never letting go until a problem is solved, and for knowing exactly when a hug is needed, even if it is only a virtual one.

Natalie – for being my instant atomic physics dictionary despite the time shift between us, as well as for being the kind of friend who does not need complete sentences!

International collaborations are not confined to former office mates. I want to thank all my co-authors for so many useful discussions, personal or via e-Mail. In particular I want to thank (in a random order)

Katja – for proofreading and patiently answering questions of all sorts,
David – for sharing the interest in GRS 1758−258 and for always helping out when I got stuck,
Jan-Uwe – for welcoming me into the paper collaboration and
Peter and Bärbel – for making me feel at home and sharing their cats for a week in Madrid, as well as
John E. Davis – for providing the `slxfig` module used for creating the presented plots, and
All other contributors to the isisscripts – for making my life so much easier.

The research leading to these results was funded by the Bundesministerium für Wirtschaft und Technologie under grant numbers DLR 50 OR 1113, DLR 50 OR 1410 and DLR 50 OR 1606.

Finally, I want to thank my family:

My parents – for their unfailing support throughout the years, and countless hours of babysitting their grandkids,
Heiko, the best husband I can imagine – for just being him ♡! Having you in my life brightens every day!
Jaan and Oskar – for being the best mischievous sons and for always keeping me distracted.

But family does not end there, and I also want to thank

The fellow firefighters of the Freiwillige Feuerwehr Uttenreuth – for being an additional family. The mutual support and trust mean a lot to me!